UNIONE EUROPEA
Fondo Sociale Europeo

Ministero dell'Università e della Ricerca

PON RICERCA E INNOVAZIONE

REACT EU

UNIVERSITÀ DEGLI STUDI DI TRIESTE

UNIVERSITÀ DEGLI STUDI DI TRIESTE

XXXVII CICLO DEL DOTTORATO DI RICERCA IN INGEGNERIA INDUSTRIALE E DELL'INFORMAZIONE

Risultati conseguiti con il finanziamento ottenuto a valere
sull'Asse IV del PON Ricerca e Innovazione 2014-2020 "Istruzione e ricerca per il recupero – REACT-EU"
Results achieved with funding obtained under
Axis IV of NOP Research and Innovation 2014-2020 "Education and research for recovery – REACT-EU"

Design of a surface permanent magnet synchronous machine with external rotor for variable speed screw turbines

Settore scientifico-disciplinare: **ING-IND/32**

DOTTORANDO / A
KIROLS EDWAR LOUIS MANSOUR

COORDINATORE
PROF. FULVIO BABICH

SUPERVISORE DI TESI
PROF. ALBERTO TESSAROLO

ANNO ACCADEMICO 2023/2024

Design of a surface permanent magnet synchronous machine with external rotor for variable speed screw turbines

Kirols Edwar Louis MANSOUR

ABSTRACT

In an attempt to mitigate CO_2 emissions and combat climate change, the role of green energy generation systems has become increasingly critical. Hydropower, one of the oldest and most environmentally friendly methods of generating electricity, remains a cornerstone of renewable energy solutions. This thesis delves into the realm of small hydropower plants, examining their diverse technologies with a particular emphasis on the innovative use of screw turbines. These systems are not only sustainable but also adaptable to a variety of environmental conditions and geographical settings. This thesis introduces an innovative approach to the design of small hydropower screw turbines, specifically focusing on the integration between screw turbines and electric generators to enhance plant efficiency and reduce maintenance requirement.

The core of this study focuses on the integration of screw turbines with electric generators, specifically Surface Permanent Magnet (SPM) synchronous machines. SPM machines are renowned for their high efficiency and robust performance, making them ideal for small-scale hydropower applications. We explore the design intricacies of these electric generators, detailing the processes and engineering principles that underpin their construction. By leveraging advanced magnetic materials and cutting-edge design techniques, we aim to enhance the performance and reliability of these generators.

Control systems play a crucial role in the efficient operation of SPM generators. This thesis investigates various power electronics control strategies, with a spotlight on the field-oriented control (FOC) method. FOC is celebrated for its precision and effectiveness in managing the torque and speed of electric machines. We provide a comprehensive analysis of its implementation, highlighting its advantages in optimizing the performance of SPM generators in hydropower systems.

A detailed cost estimation is conducted, reflecting the economic aspects of SPM generator deployment within the Italian market context of 2023. This analysis includes a breakdown of material costs, manufacturing expenses, and market trends, providing a holistic view of the financial viability of small hydropower projects.

Furthermore, we address one of the significant challenges in SPM machine operation: eddy current losses. These losses can significantly impact on the efficiency and longevity of electric generators. Our research proposes an innovative approach to reduce eddy current losses by altering the winding configurations without changing the machine geometry. This method promises to enhance efficiency and reduce operational costs, contributing to the overall sustainability and effectiveness of small hydropower plants.

In conclusion, this thesis not only advances the understanding of SPM generators in small hydropower applications but also introduces novel solutions to enhance their performance and economic feasibility. By bridging the gap between traditional hydropower techniques and modern engineering innovations, this work paves the way for more efficient, reliable, and eco-friendly energy generation systems.

Index

Figure Index

Tables Index

Acronyms list

Acronyms	Extended form
SPM	surface permanent magnet
D1	Inner stator diameter
D3	Outer stator diameter
D4	Inner rotor diameter
D5	Outer rotor diameter
P3	Outer stator perimeter
T_{max}	Maximum torque
B_{FeMax}	Maximum magnetic induction within the iron
NSB	Number of turns per coil
NCP	Number of parallel circuits
AFE	Active Front End Inverter
L_n	Machine net length
N_P	Poles number
N_C	Slots number
L_{phase}	Length of a single phase winding
S_w	Area of a single coil winding wire
PID	Proportional-Integral-Derivative controller
FOC	Field Oriented Control
EMF	Electromotive Force
MMF	Magneto Motive Force

1 Introduction

In an era dominated by the pursuit of sustainable and eco-friendly energy sources, hydropower plants have emerged as a beacon of hope in the global energy landscape. As societies grapple with the urgent need to address climate change and its devastating consequences, the exploration of renewable energy solutions becomes increasingly vital. Hydropower, the oldest clean power source, presents an environmentally friendly alternative to fossil fuels and remains a cornerstone of renewable energy solutions, accounting for the largest share of power generated from renewables [1].

While large-scale hydropower plants equipped with dams and reservoirs have historically dominated the industry, their remarkable negative environmental impacts, high initial investment costs, and long pay-back times present significant challenges for future expansion. Conversely, the potential for run-of-the-river plants, particularly micro-hydropower and small hydropower plants, holds promise for important growth in the coming years. These smaller-scale facilities, characterized by their reduced environmental impact, limited investment requirements, and safe operation, are particularly suitable for distributed generation [2].

This thesis aims to provide a comprehensive analysis of small screw turbine hydropower plants, with a particular focus on enhancing plant efficiency and reducing maintenance requirements through innovative integration between screw turbines and Surface Permanent Magnet (SPM) synchronous machines for electric generation [3]. By examining the design, operation, speed control systems, and performance characteristics of these compact power facilities, this research seeks to shed light on their pivotal role in the transition toward a sustainable energy system.

The second chapter of this thesis will delve into the intricacies of small hydropower plants, encompassing different turbine technologies and highlighting their significance in the broader renewable energy context. Additionally, the chapter will explore the traditional screw turbines and introduce a novel technological solution with innovative design principles for the integration between screw turbines and the electric generation.

Chapters three, four, and five will focus on the engineering aspects governing the design of SPM electric generators [4] for small hydropower plants, while chapters six and seven will examine the critical importance of the field-oriented control

(FOC) method for the speed and torque control systems [5], discussing various governing mechanisms and their impact on turbine efficiency and system reliability.

Amidst the numerous advantages of small hydropower systems, significant challenges must be addressed to facilitate their development, particularly in terms of the economic aspects associated with electric generators. The eighth chapter of this thesis will provide a detailed analysis of the total cost of designing an electric generator based on the Italian market conditions in 2023 [6].

Finally, the subsequent chapters will focus on optimizing the electric generator to reduce the eddy current power losses [7], enhance efficiency, and extend its lifespan, contributing to the development of more cost-effective and efficient small hydropower systems.

In conclusion, this thesis seeks to contribute essential insights into the realm of small hydropower plants, offering a holistic understanding of their design, operation, performance, and environmental significance. By assessing the challenges and opportunities in their development, this research endeavors to promote the integration of small hydropower plants as a key component in the journey toward a more sustainable and resilient global energy system.

2 Small Hydropower Plants

In the relentless pursuit of sustainable energy solutions, the world's attention has turned resolutely towards the potential harbored within small hydropower plants. These compact yet potent installations have assumed a central role in the discourse surrounding renewable energy, offering a localized means of generating clean electricity. Their intrinsic ability to harness the kinetic energy of flowing water renders them not only ecologically sound but also conducive to reducing carbon emissions and ensuring energy security. An intriguing facet of small hydropower plants is their inherent adaptability to a spectrum of geographic and hydrological circumstances, ranging from mountainous terrains with steep gradients to lowland areas characterized by more modest water flows. This adaptability endows them with the versatility required to establish themselves as a cornerstone of decentralized energy production, capable of tailoring their approach to diverse local conditions.

2.1 Main turbine technologies

Central to the operational efficacy of small hydropower plants are four quintessential turbine technologies, each meticulously designed to suit distinct hydrological contexts and power generation requisites. The Pelton turbine, renowned for its proficiency in converting high head and low flow water sources into electrical power, is characterized by its array of double-cupped buckets and high rotational speeds. This unique configuration optimizes its performance by enabling the efficient transfer of the water's kinetic energy to the turbine's rotating shaft, subsequently powering the attached generator.

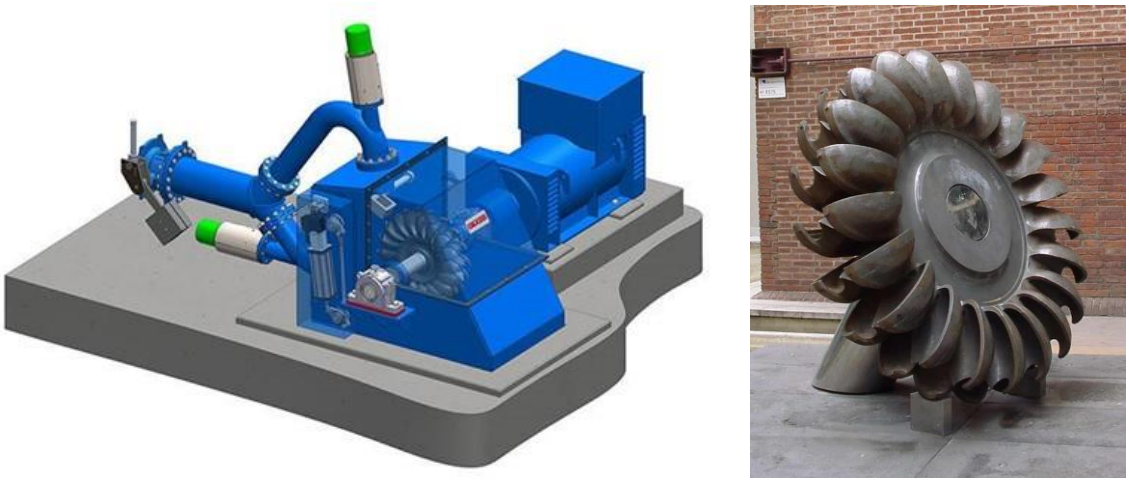

Figure 1: Pelton turbines [8].

Contrastingly, the Francis turbine, characterized by its applicability in medium head and flow scenarios, embodies adaptability and versatility. This turbine employs a combination of radial and axial flow principles, making it an invaluable asset in accommodating a diverse range of hydraulic conditions. Its ability to maximize energy extraction from the water flow, coupled with its comparatively lower rotational speeds, ensures optimal operational efficiency across a broad spectrum of settings.

Figure 2: Francis turbine [9] [10].

In environments defined by low head and high flow conditions, the Kaplan turbine emerges as the technology of choice. Its adjustable blades and propeller-like design facilitate efficient energy capture, even amidst variable water flows. This adaptability not only enhances its efficiency but also underlines its suitability for rivers, tidal currents, and other dynamic aquatic environments, where consistency in flow rates is often challenging to predict.

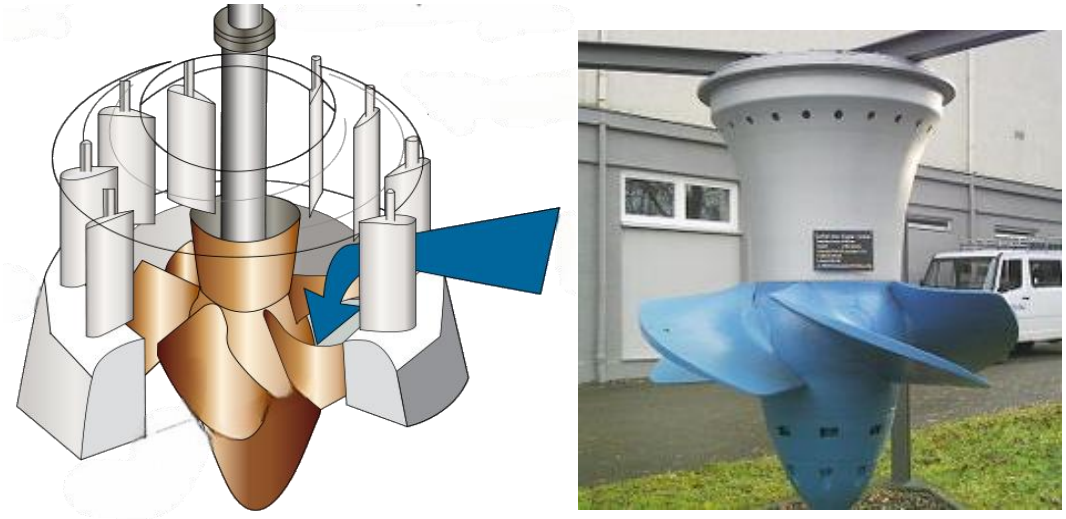

Figure 3: Kaplan turbine [11].

Furthermore, the realm of small hydropower plants encompasses the innovative screw turbine, a technology well-suited for installations characterized by low head and moderate flow rates. What sets the screw turbine apart is its low rotational speed

and ability to accommodate a diverse array of fish species during their passage through the turbine, thereby addressing ecological concerns associated with traditional turbine technologies.

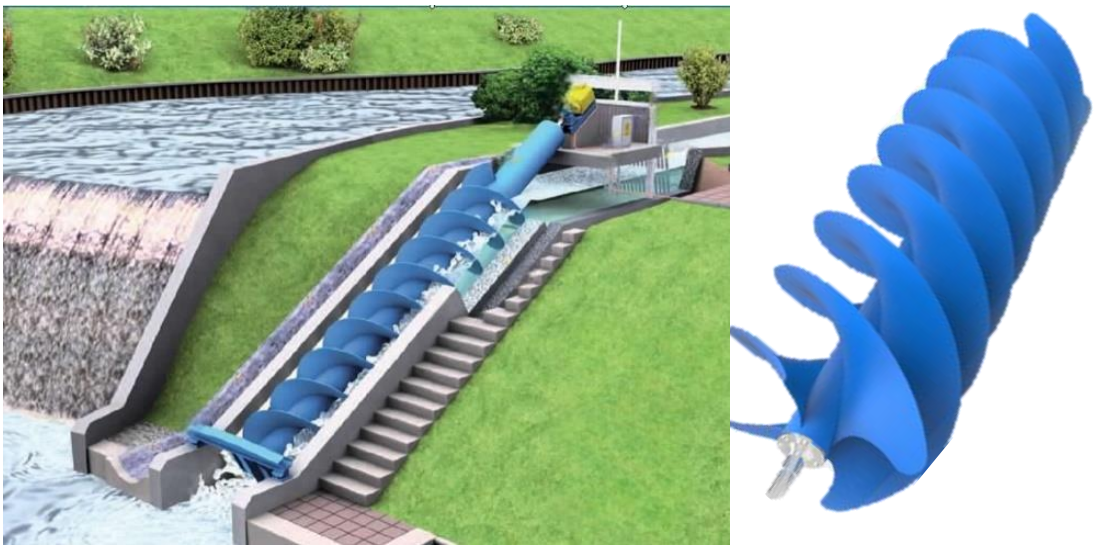

Figure 4: Screw turbines [12].

This comprehensive exploration of the Pelton, Francis, Kaplan, and screw turbines within the domain of small hydropower plants unravels their distinct operational principles, advantages, and limitations. The intricate interplay of these technologies, each tailored to particular hydraulic conditions, culminates in a holistic and adaptable approach to sustainable energy generation. By harnessing the forces of nature in a way that respects both environmental considerations and the imperatives of power production, these technologies collectively contribute to steering our global energy landscape toward a cleaner, more resilient future.

2.2 New Solution for Screw Turbines

Central to the efficacy of small hydropower plants are various turbine technologies, each tailored to specific hydrological contexts. In this thesis, the screw turbine has taken a stride towards innovation, exemplifying a novel approach to extracting energy from low head, moderate flow conditions and a large variable speed range. This technology represents a harmonious synergy between mechanical engineering, electrical engineering and automation system engineering. The proposed contribution addresses an innovative design concept for a screw turbine based small hydropower plant, resulting from the cooperation between academia and the HPG s.r.l. company specialized in micro and small hydropower technology solutions.

The traditional layout for screw-turbine based plants is provided in Figure 5. It consists of an electric generator G, a coupling C and a screw turbine T. The turbine is driven by a current stream falling through a conduit from an upstream level $H_{upstream}$ to a downstream level $H_{downstream}$. The so call head, equal to the difference $H_{upstream} - H_{downstream}$, is generally lower than 10 m. The generator is coupled to the turbine via a coupling C which can be implemented as a gearbox. In fact, rotational speeds are usually around 30 rpm, which would lead to significant generator size if a direct coupling were adopted. In order to keep the generator size within acceptable limits, its speed is increased, and its torque reduced compared to the turbine values by a gearbox coupling with suitable gear ratio. As it can be seen from Figure 5, the generator is usually coaxial with the turbine, so that the whole rotational axis is bent (neither vertical nor horizontal) and the generator is mounted at the top end of the turbine as a cantilever structure. A picture illustrating the overall group mechanical arrangement is provided in Figure 6.

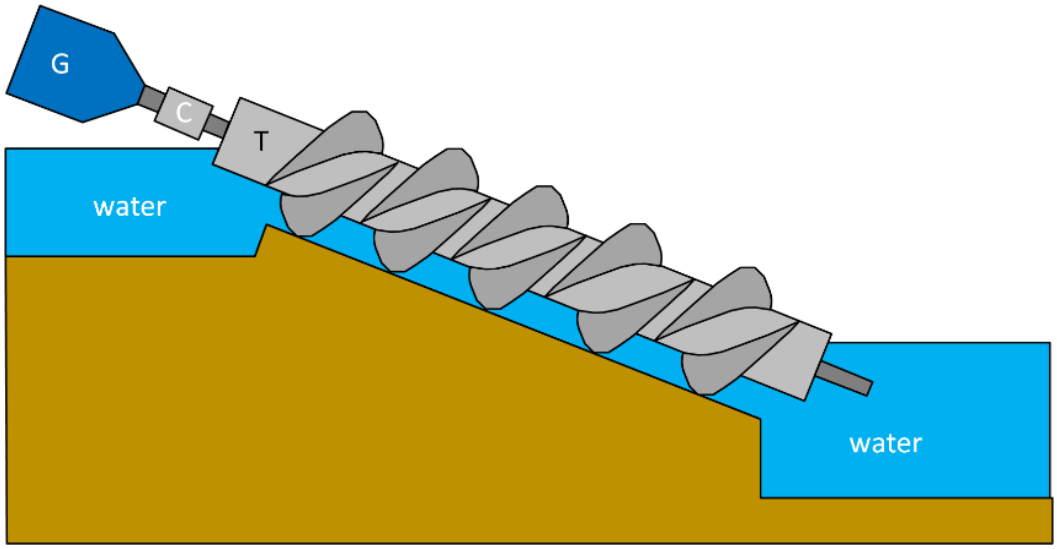

Figure 5: Traditional layout for screw turbine based hydropower plant.

Figure 6: Example of an electric generator coupled to a skew turbine for a hydropower group.

The design solution proposed in the thesis consists of a mechanical integration between the turbine and the electric generator, as sketched in Figure 7. The hollow inner structure of the turbine is exploited to locate the generator inside the turbine itself. This can be done through an outer-rotor generator (outer-rotor SPM synchronous generator). The back iron of the generator is directly provided by the turbine cylinder by fixing permanent magnets on its inner surface. The stator is located inside the inner hollow part of the turbine. Using the inner diameter of the turbine as a design constraint and the air gap as a mechanical construction constraint, the goal is minimizing the used material in order to reduce the generator cost.

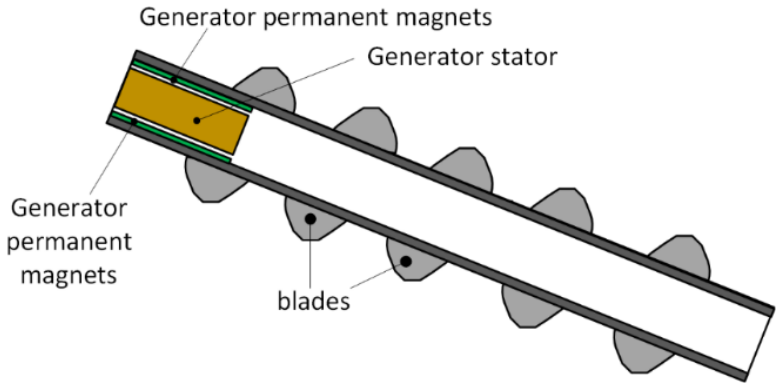

Figure 7: New proposed arrangement with the electrical generator integrated into the screw turbine.

This solution offers the elimination of the mechanical coupling, which leads to great benefits in terms of maintenance, reliability and efficiency [13]. Moreover, the overall axial length of the turbine-generator group is significantly shortened. On the other side, the direct-coupling solution implies the generator and turbine to have the same speed and torque. Hence the generator size (and so its cost) is expected to be

higher than in the case where a gearbox is employed. The higher cost of the generating system is also related to the higher quality of the machine (permanent magnet machine for the direct drive solution vs induction machine for the gearbox solution) and the related higher cost of materials. The design challenge is therefore to find an electromagnetic configuration which preserves the economic competitiveness of the generating group.

This thesis presents the electromagnetic dimensioning and design of the generator subject to the performance and dimensional constraints imposed by the final application. Different design solutions are explored, all characterized by a fractional-slot dual-layer concentrated tooth-coil winding for the stator section. This choice is dictated by the extremely low speed of the machine, which forces to choose the number of stator teeth relatively close to the number of rotor poles, in addition to the simpler construction and very short end windings compared to distributed winding solutions [4]. The surface mounted permanent magnet arrangement obviously descends from the idea of using the very turbine mechanical structure as the rotor core.

3 Electrical Generator Specification

In order to embark upon the initiation of the generator design phase, to be subsequently incorporated within the turbine, a pivotal collaborative discourse was necessitated alongside HPG s.r.l. The objective was to jointly ascertain a pertinent scenario involving a medium-sized turbine, which had hitherto been employed, thereby delineating a potential focal point for rigorous examination. This turbine, characterized by the following salient attributes, has emerged as a captivating subject for comprehensive invention:

- An internal diameter of 1321 mm.
- A nominal rotational velocity of 30.3 rpm.
- A peak turbine torque of 60 kNm.
- An utmost turbine length spanning 8354 mm.

This strategic selection was predicated upon a convergence of insights, designed to engender a robust foundation for the ensuing phases of inquiry, analysis, and design. Such meticulous scrutiny of this exemplar turbine, Figure 8, lays the groundwork for elucidating patterns, correlations, and design principles that shall undeniably enrich the fabric of our academic exploration.

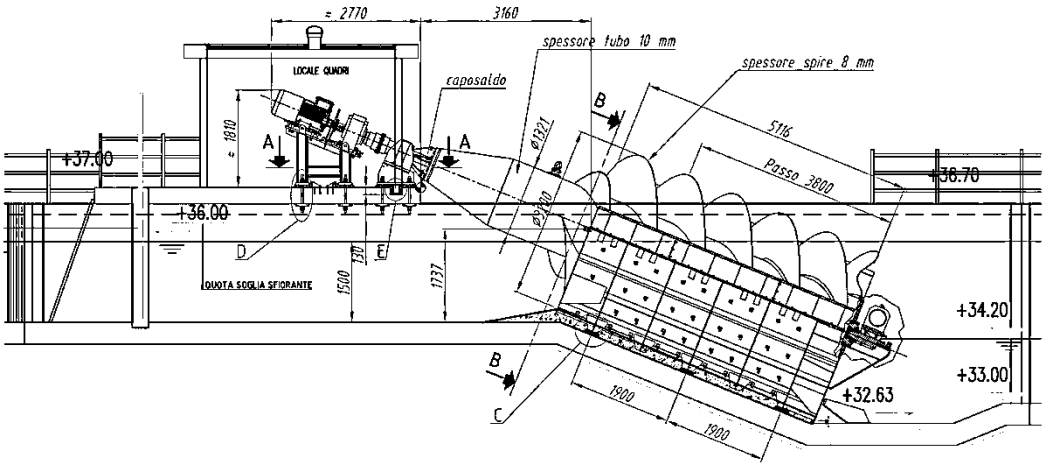

Figure 8: A two-dimensional view of the screw turbine.

Taking into consideration the provided data, a conclusive determination has been reached to orchestrate the design of the generator, stipulated by the ensuing set of specifications:

- The external diameter of the rotor (D5) is slated at 1300 mm.
- The rotor's nominal rotational speed is fixed at 30.3 rpm.
- The operational envelope encompasses a dynamic spectrum, ranging from 3.3 rpm to 33.3 rpm.
- The generator's nominal power output stands at 190 kW.
- The upper echelon of generator torque reaches a pinnacle of 60 kNm.
- The generator's dimensions are bound by a maximum length of 8354 mm.
- Integral to the design, the stator configuration is characterized by rectangular teeth, each possessing a minimum width of 20 mm.
- A material selection of the utmost thickness is incumbent for the stator laminations, and specifically, M800-100A [14] has been elected as the designated material of choice. This material was chosen by the company duo to it simplicity in production.

Such meticulous delineation of design parameters is poised to propel our endeavor toward a meticulous translation of conceptual ingenuity into tangible engineering fruition. By harmonizing the imperatives of performance, functionality, and materiality, this framework serves as a cogent testament to our commitment to the pursuit of excellence in generator design and its synchronous integration with the intricate ecosystem of the turbine.

3.1 Finite Elements Analysis Software

With the complete dataset at our disposal, it became feasible to meticulously determine the essential software tools to be employed throughout the design phase. After careful consideration, the initial preference was directed towards FEMM 4.2 [15], an open-source software solution renowned for its robust capabilities in finite element analysis of magnetic fields. This software not only aligns effectively with our project's requirements but also offers a cost-efficient approach to simulating intricate electromagnetic phenomena.

To harness the full potential of FEMM 4.2, a comprehensive script was meticulously developed. This script serves as a versatile tool, enabling the parametric design of surface permanent magnet (SPM) synchronous machines. It empowers engineers to meticulously define various design parameters, facilitating the creation of intricate geometries tailored to specific project needs. Subsequently, this script seamlessly interfaces with FEMM 4.2, orchestrating the simulation process with precision and consistency.

In adopting this software and script framework, our approach emphasizes not only technical efficacy but also a streamlined workflow. By integrating a systematic and

automated method for designing and simulating machines, we aspire to achieve a higher level of efficiency, accuracy, and repeatability in our design process. This software-script synergy not only enhances the quality of our designs but also contributes to a more robust foundation for research and analysis within the realm of electromagnetic machine design.

The meticulously crafted script serves as an intricate tapestry that weaves together a multitude of parameters, each a crucial brushstroke that collectively characterizes the essence of the synchronous machine model. This orchestration embraces not just technical details, but an encompassing understanding of the machine's behavior, dynamics, and potentialities. Let us embark on a comprehensive exploration of these parameters:

- *Internal and External Diameters*: The stator and rotor, the very core of the machine, are defined by their internal and external diameters. These dimensions lay the architectural groundwork, shaping the machine's physical form and electromagnetic interactions.
- *Stator Slot Geometry*: The labyrinthine slots within the stator play an instrumental role in flux distribution. Dimensions like length and width of these slots, as well as that of bridges and wedges, intricately influence magnetic paths and conduction properties.
- *Stator Slot Configuration*: The arrangement of slots shapes the machine's performance. The type and number of stator slots intricately influence its operational characteristics, encapsulating a blend of form and function.
- *Magnet Characteristics*: The magnets infuse the machine with magnetic energy. Their dimensions, coercive force, and surface distribution determine the very essence of the machine's magnetic field, a vital foundation for its operation.
- *Pole Number*: The machine's magnetic structure is further defined by the number of poles. This parameter lays the groundwork for its magnetic behavior and the dynamics of energy conversion.
- *Winding Attributes*: The heart of the machine's operation, the winding attributes, encompass vital specifications like the number of parallel circuits (NCP), number of turns per coil (NSB), and the configuration of coil circuit sets within the machine.
- *Cooling Pipes*: In the heat of operation, cooling is essential. The placement, quantity, and dimensions of cooling pipes on the stator facilitate heat dissipation, ensuring the machine's sustained performance and longevity.
- *Simulation Current*: The dynamic force of simulation current permeates the entire analysis, unraveling the machine's behavior and characteristics under varying conditions.

These parameters provide the groundwork for a diverse spectrum of simulations:

1. **Stator Flux Simulation**: Uncovering the intricacies of electromagnetic interactions, this simulation reveals the flux linked with stator windings when the stator circuit is open, a foundation for understanding its magnetic dynamics.
2. **Torque Curve Generation**: The torque curve, a cornerstone of the machine's operational behavior, takes shape as the rotor rotates with a constant imparting insight into its torque-generation capabilities.
3. **Torque Ripple Analysis**: During operation, torque ripple can emerge, offering insights into operational smoothness. This simulation delves into the nuances of torque variation during the machine's regular function.
4. **Cogging Torque Assessment**: Idle states hold secrets too. This simulation investigates the cogging torque produced in the stator teeth when the stator circuit is unpowered, unraveling magnetic interactions.
5. **Harmonic Field Analysis**: The harmonic components within the air gap magnetic field, dissected by this simulation, cast light on the intricate nature of the machine's magnetic flux.
6. **Inductance Determination**: Using the potential method, the script calculates direct-axis and quadrature-axis inductances, opening the door to understanding key electromagnetic properties.

Throughout these simulations, the model's depth remains a constant 1 mm. This practical choice allows the computation of the machine's actual depth by relating the nominal torque to the torque generated by the 1 mm model.

In Figure 9, the initial machine model generated by the aforementioned script is illustrated. The visualization captures the essence of the machine's foundational design parameters, as synthesized through the script's intricate orchestration. The model's form, defined by its dimensions, winding configurations, and material attributes, serves as a canvas on which the script's analytical prowess is transmuted into tangible engineering manifestation.

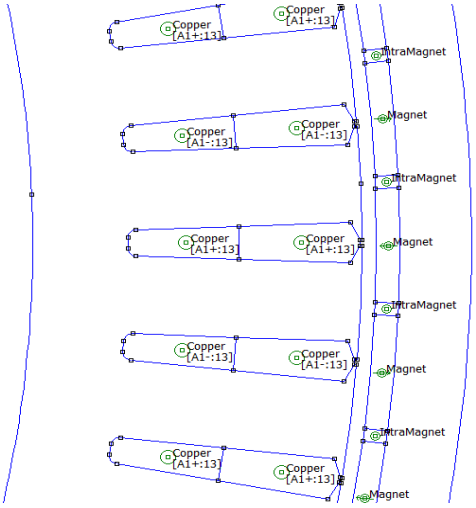

Figure 9: Cross section of the electromagnetic design solutions for the electric generator.

Through the tapestry of these simulations, two avenues open:

- **Linear Model with Efficiency**: A model employing a linear ferromagnetic material configuration, devoid of saturation, offers expedited results, bolstering efficiency.
- **Non-Linear Model for Precision**: A more comprehensive model incorporates ferromagnetic material characteristics with saturation, yielding finely-tuned and accurate outcomes at the expense of computational time.

This comprehensive and meticulous approach culminates in a script that not only encapsulates technical intricacies but nurtures a profound understanding of the synchronous machine's multi-faceted behavior. The script serves as a bridge between theoretical exploration and practical application, facilitating a harmonious synthesis of scientific inquiry and engineering realization.

3.2 Generator Designing Rules

Following the successful development and validation of the script, the project seamlessly transitioned to the intricate realm of synchronous generator design.

3.2.1 Poles and Slots

With the paramount objective of achieving optimal performance at remarkably low rotational velocities, a strategic decision was made to optimize the pole number. This meticulous strategy aimed to ensure that the resulting electrical frequency remains

at or above the desired threshold of 20 Hz. This endeavor, underpinned by both technical ingenuity and mathematical precision, steered the project towards a configuration that would yield not only practical efficiency but also a harmonious distribution of electromagnetic forces.

As a calculated maneuver, a dual-layer concentrated tooth-coil winding was chosen for the stator [4]. This design philosophy, in conjunction with a pole-to-slot ratio of $N_P/N_C = 20/21$, where N_P is the poles number and N_C is the slots number, emerged as the embodiment of this endeavor. This ratio was strategically selected to strike a balance between operational stability, harmonic content, and manufacturing feasibility. By configuring N_P to a preliminary value of 80, a calculated electrical frequency of 20.2 Hz was achieved, thereby illuminating the ideal value for N_C, which was determined to be 84.

3.2.2 Number of Parallel Circuits

The inherent symmetry of the machine, dictated by the number of poles and slots, has enabled the division of the machine into four sections, called parallel circuits (NCP = 4). This strategic configuration not only imparts a level of flexibility during the control phase but also serves as an assurance for the machine's seamless operation.

The division into four parallel circuits presents a versatile control framework. In fact, the four parallel circuits could be organized as independent three-phase windings which supply four inverters to inject the produced power into the grid. This means that the machine can be thought as 4 different machines connected in parallel. If one of these machines gets defected, the other three machines can work independently. This arrangement would equip the machine with an inherent redundancy, ensuring uninterrupted operation even in the event of a circuit interruption during machine operation. This strategic design consideration underscores a robust engineering approach, ensuring not only efficiency but also resilience within the machine's functioning.

3.2.3 Machine Diameters

However, the complexity of the synchronous generator's design journey extended beyond just these numerical determinants. A critical design consideration revolved around defining the minimum distance between the magnets and the rotor's outer diameter, often referred to as the rotor magnetic yoke. This intricate distance, embodying a fusion of magnetic flux dynamics and mechanical strength imperatives,

was meticulously analysed. Collaborative discussions with the company's technical experts culminated in a consensus to utilize magnets with dimensions of approximately 40 mm in width and 8 mm in height. This collaborative endeavor aimed to harmonize magnetic efficiency with structural robustness, culminating in a strategic decision to extend this distance to approximately 60 mm. This measure not only assured optimal magnetic performance but also bolstered the mechanical integrity of the generator's construction.

Armed with this multifaceted understanding, the project moved forward to precisely delineate the initial diameters of the synchronous generator:

- The outer rotor diameter (D5) was meticulously established at 1300 mm, an embodiment of both structural stability and efficient magnetic flux distribution.
- The inner rotor diameter (D4) was artfully configured as 1235 mm, encompassing a delicate balance between mechanical constraints and electromagnetic efficiency.
- Navigating the nuanced space between electromagnetic performance and thermal considerations, the outer stator diameter (D3) was meticulously chosen as 1225 mm, factoring in a 5 mm of air gap.
- Finally, the inner stator diameter (D1) was artfully set at 1000 mm, aligning with design specifications while embracing a holistic perspective on machine integration.

This deliberate orchestration of diameters and design considerations is emblematic of the symbiotic marriage between scientific prowess and engineering pragmatism. It lays the foundation for a synchronous generator that embodies not just technical excellence but also an intricate interplay of electromagnetic forces, mechanical robustness, and operational harmony. As the generator design unfolds, this preliminary groundwork serves as a compass, guiding the exploration into the complex and captivating realm of electromagnetic machinery.

3.2.4 **Finding the Simulation Current**

Given the critical requirement for the machine to feature rectangular teeth with a minimum width of 20 mm, a thoughtful analysis of the stator's external perimeter becomes essential. With D3 already determined as 1225 mm, the external stator perimeter (P3) can be expressed as $P3 = \pi \times D3 = 3877$ mm. To ensure that the machine design adheres to the stipulated width requirements for the teeth, a meticulous calculation follows. The aim is to divide the stator's external perimeter

(P3) by twice the number of slots (NC), accounting for both teeth and slots. Thus, the calculated value is P3 / (84 × 2) = 23 mm. This calculated width of 23 mm stands as a promising and viable choice. Notably exceeding the stipulated minimum width of 20 mm, this decision aligns harmoniously with the design parameters.

The height of the slot is intricately linked to the number of conductors (turns) accommodated within it. As an initial assumption, a trapezoidal slot with a height of 80 mm (equivalent to a slot area of 1300 mm²) is considered. In this preliminary scenario, let us propose a single turn per coil (NSB = 1). Consequently, the current to be set for simulation is calculated as:

$$\frac{Aslot * J * 0.5}{2} \approx 2000 \text{ A}_{\text{turns}}$$

Here, A_{slot} represents the slot area, J represents the current density, contingent upon the type of cooling employed (which is 6 A/mm^2 in this case, signifying water cooling). The fill factor, denoted as 0.5, accounts for the space between conductors (since they are circular) and insulation, and this result is divided by 2 to account for the dual-layer nature of the slots (with two active conductors).

This calculation testament to the fusion of theoretical precision with practical application. As the project navigates the tapestry of engineering intricacies, this calculated current emerges as a guiding force, propelling the synchronous generator's evolution towards optimal performance and operational harmony.

Finally, all the carefully chosen parameters come together in a visual representation of a machine cross-section.

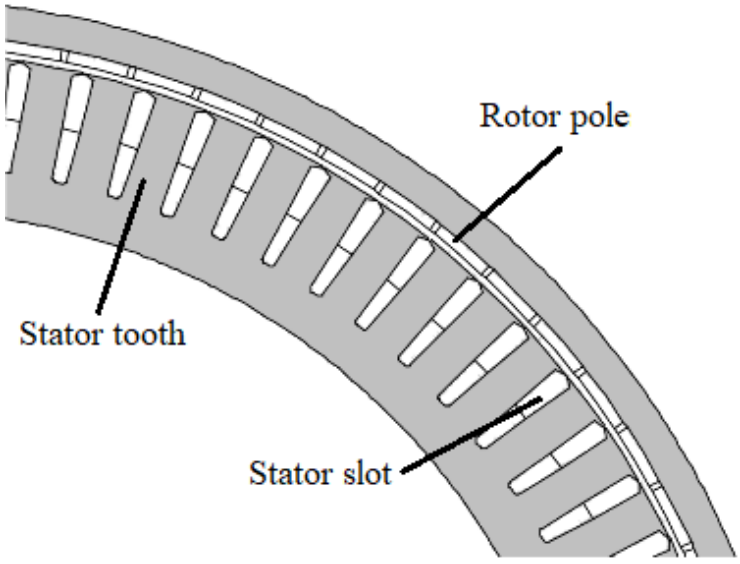

Figure 10: Cross section of the electric generator.

4 First Generator Designing

As emphasized earlier, all simulations will be conducted with a fixed machine depth of 1 mm. This approach facilitates the calculation of the effective machine depth by dividing the nominal torque by the torque produced at this standardized 1 mm depth.

This particular choice of uniform depth harmonizes with the characteristics of the screw turbines manufactured by HPG s.r.l.. In these turbines, the internal diameter remains consistent across designs. To achieve varying power and torque outputs, adjustments are made to the screw's length. By opting for a fixed 1 mm depth, a versatile parameterization of simulations is enabled, catering to a wide spectrum of generator power requirements. This standardized approach streamlines the analysis process and allows the company to seamlessly extrapolate performance insights across different power levels while maintaining a constant internal diameter.

4.1 Tuning of the Teeth Length

The initial simulation involves calculating the flux linkage (with the stator circuit opened) in the absence of saturation. For this purpose, a single point suffices to determine the magnetic induction within the teeth. Subsequently, based on this data, the dimensions of the teeth and slots are adjusted to achieve a maximum magnetic induction of approximately B = 1.5 T within the stator teeth. This iterative approach not only simplifies the simulation process but also ensures that the machine's magnetic performance aligns with the desired threshold. By iteratively fine-tuning the dimensions of the teeth and slots, the magnetic induction is optimized, fostering an efficient and balanced distribution of magnetic flux throughout the machine. This method underscores the intricate interplay between simulation results, design modifications, and the ultimate goal of achieving magnetic performance within the desired range.

4.2 Three Phases Flux Linkage

A second simulation is initiated to calculate the flux linkage and observe the behavior of flux linkages across the three phases. To achieve this, the polar pitch of the machine model is divided into 90 equidistant points, in the absence of saturation. The outcomes of each of these points are meticulously saved and recorded.

In Figure 11, we can observe a distinct sinusoidal pattern in the flux linkages along the polar pitch of the model. This sinusoidal behavior signifies a harmonious alignment with the machine's design, highlighting the synchronization between electromagnetic forces and phase currents. This symmetrical progression is a testament to the effectiveness of the design choices made and the precision of the simulation process.

This visual depiction encapsulates the synergy between mathematical modelling, simulation, and real-world implications. The sinusoidal flux distribution stands as a visual testament to the successful of electromagnetic forces in the machine.

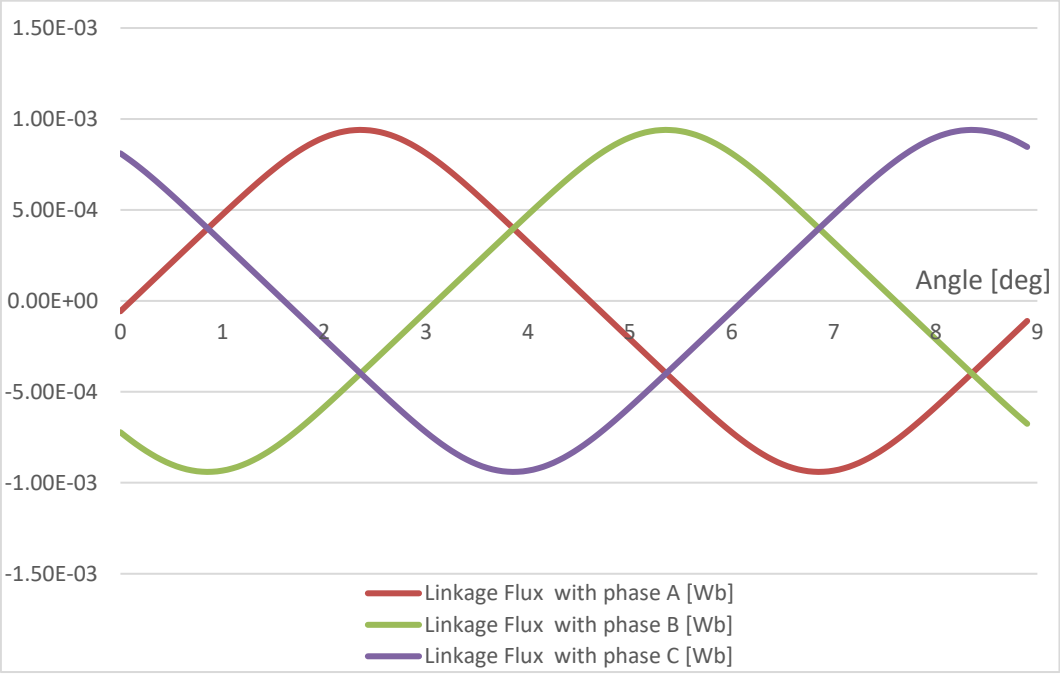

Figure 11: The flux linkages along a polar pitch with 2000A of model current.

4.3 Torque Curve

A third simulation is executed to study the torque profile by discretizing the polar pitch of the machine model into 90 segments. The outcomes of each of these segments are recorded systematically. For practicality, this simulation is conducted using linear ferromagnetic material properties, bypassing saturation effects for computational expediency.

Upon completing this simulation, the angle corresponding to the point of maximum torque, T_{max}, for the 1 mm deep machine model is identified. This angle stands as the operational angle of the machine, which holds pivotal significance. It will serve

as a cornerstone parameter in forthcoming simulations, particularly those concerned with torque ripple analysis.

Figure 12 aptly depicts the torque behavior over the polar pitch. Upon closer examination of the graph, we can discern a distinct peak at approximately 0.1 degrees. This angle marks the juncture at which the machine generates its maximum torque output. In the context of torque ripple simulations, this angle plays a central role, serving as the reference point for studying deviations from this optimal operating condition.

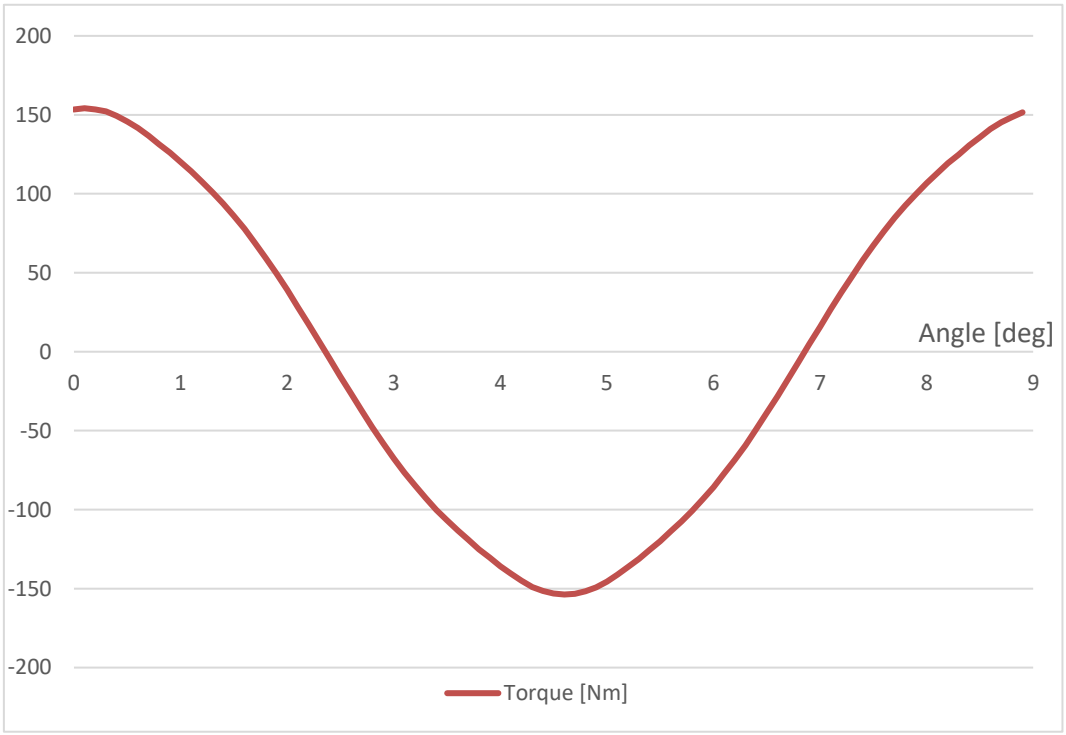

Figure 12: The torque curve along a polar pitch with 2000A of model current.

4.4 Fine-Tuning of the tooth width and Model Current

From the findings of the third simulation, the angle corresponding to the maximum torque is determined (in our case, this angle is 0.1 mechanical degrees). For the subsequent torque ripple simulation, a single simulation point is necessary. By initializing this simulation with an angle of 0.1 degrees, it becomes possible to ascertain the maximum magnetic induction within the iron, denoted as B_{FeMax}. Based on this value of B_{FeMax}, it is feasible to calculate a compromise between the maximum Ampere-turns and the width of the tooth/slot, in order to achieve a maximum induction of 1.5 T.

In the context of our case, this optimization led to the widening of the tooth to 30 mm and an Ampere-turns value of 1200 A. This delicate balance ensures that the machine performs at its optimum magnetic saturation level while accommodating design constraints and operational requirements. This iterative process, founded on simulation data, marries precision with practicality, culminating in a design that seamlessly integrates performance and robustness.

4.5 Finding the Generator Length

By utilizing the non-linear laminations M800-100A, a torque profile is calculated across 90 rotor positions to determine the maximum produced torque, T_{max}, for the 1 mm deep machine model, accounting for non-linear behavior and saturation effects. This process aims to establish a connection between the maximum attainable torque and the desired nominal machine torque specified in the design requirements.

Through this simulation, a T_{max} value of 69 Nm is attained. However, the specified maximum required torque for the machine is 60 kNm. This disparity underscores the need to adjust the machine's physical dimensions to align with the specified torque requirement. By dividing the specified nominal machine torque by T_{max}, the net length of the machine can be determined. Following this calculation, the machine's net length is estimated to be approximately 870 mm. This iterative process highlights the intricate interplay between simulation results, material properties, and design constraints. The discrepancy between simulated and desired torque emphasizes the need to optimize design parameters to achieve the desired performance characteristics while adhering to real-world practicalities. Results can be shown in Figure 13 and Figure 14.

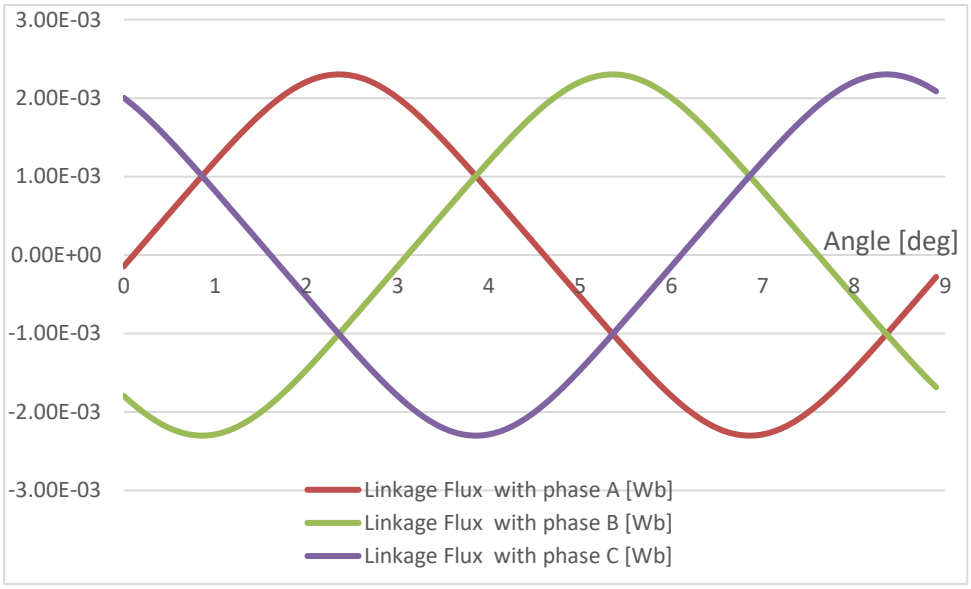

Figure 13: The flux linkages along a polar pitch with 1200A of model current.

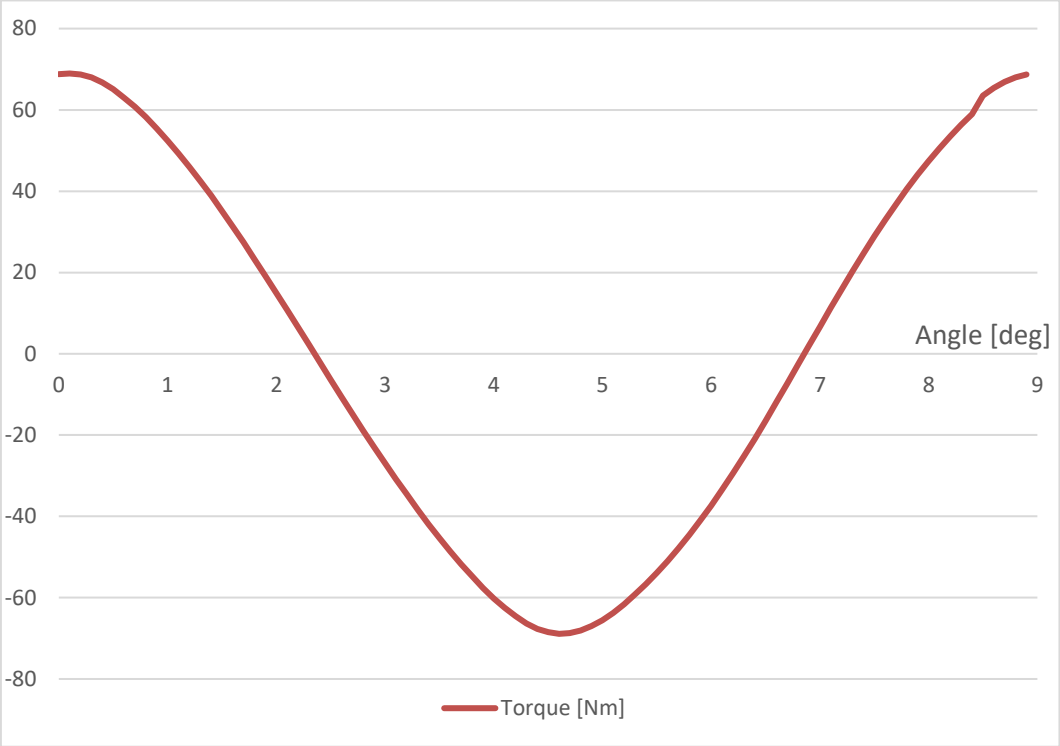

Figure 14: The torque curve along a polar pitch with 1200A of model current.

4.6 Calculation of NSB and NCP

The most recent series of simulations were undertaken using a single coil per winding (NSB = 1) configuration along with four parallel circuits (NCP = 4). Additionally, a nominal current was assigned, specifically tailored for a singular coil per winding. To achieve a comprehensive representation of the generator model, the intricacies of its winding parameters had to be meticulously calculated.

As a preliminary step, the determination of the generator's produced voltage was deemed imperative. Given the generator's intended connection to the low-voltage electrical grid via an Active Front End (AFE) inverter, a rms line-to-line nominal voltage (V_n) of approximately 500V was deemed appropriate. Consequently, this leads to an effective phase voltage (E_n) measuring approximately 290V. This voltage selection, deliberately set at 25% above the grid voltage, aims to ensure a reliable and stable operation throughout the entire stipulated speed range.

Subsequent to finalizing the generator's voltage, a rigorous torque curve simulation was executed, accounting for saturation effects, precisely at the angle corresponding

to the maximum torque occurrence (0.1°). The principal objective of this simulation was to acquire a comprehensive comprehension of the flux linkages across the three distinct phases, specifically at the point of peak torque. Upon the successful determination of these flux linkages, the overall magnitude of the machine's flux was evaluated using Equation 1. Here, the variables λ_A, λ_B and λ_C symbolize the respective flux linkages pertaining to phases A, B, and C.

$$\lambda = \left|\frac{2}{3} * \left(\lambda_A e^{-0i} + \lambda_B e^{\frac{-2}{3}\pi i} + \lambda_C e^{\frac{-4}{3}\pi i}\right)\right| = 1.12 * 10^{-3}\ Wb$$

Equation 1

With the machine's flux magnitude accurately ascertained, the next step involved the utilization of Equation 2 to ascertain the winding ratio N. This equation involves the nominal electrical frequency of the machine (f_n), set at 20.2 Hz, and the net length of the machine (L), which is measured at 870 mm.

$$\mathrm{N} = \frac{\sqrt{2} * E_n}{2\pi * \lambda * f_n * L} = 3.35$$

Equation 2

It is noteworthy to mention that the winding ratio N corresponds to the ratio of the number of coil turns to the number of parallel circuits. Given the stipulated presence of four parallel circuits, Equation 3 was employed to deduce the appropriate number of turns per coil.

$$\mathrm{NSB} = N * NCP = 13.402$$

Equation 3

Upon rigorous application of Equation 3, the value of NSB was derived as 13.402. However, due to the inherent requirement for whole-number values, NSB could only practically assume values of either 13 or 14. Prior to finalizing the choice of the number of turns per coil, a critical assessment of the nominal current of the machine was undertaken, employing Equation 4. Notably, in this context, A_{turns} was stipulated to be 1200A.

$$\mathrm{I_n} = \mathrm{A}_{turns} * \frac{NCP}{NSB}$$

Equation 4

Given the two viable alternatives concerning the number of coil turns, a strategic decision was made to conduct dual torque simulations, strategically focusing on the

critical juncture of maximum torque incidence at 0.1°. Following the meticulous analysis of the results obtained from these simulations, a judicious selection of the appropriate number of coil turns was achieved. The tabulated data presented in Table 1 effectively encapsulates the outcomes of the two distinct simulations.

NSB	I_n	E_n
13	370 A	281 V
14	343 A	302 V

Table 1: Comparison between NSB = 13 and NSB = 14.

Upon a comprehensive review of the results presented in Table 1, it becomes conspicuously evident that the solution corresponding to NSB = 14 would invariably yield a machine voltage that significantly surpasses the desired threshold. In view of this, a prudent course of action was determined, leading to the adoption of the alternative solution characterized by NSB = 13 and I_n = 370A.

In summary, the culmination of rigorous simulations and thoughtful parameter calculations has led to a comprehensive understanding of the generator's winding configuration and characteristics. Through a systematic approach, we determined the generator's generated voltage to align with low-voltage grid connectivity throw an inverter. Torque curve simulations, accounting for saturation effects, provided insights into the maximum torque point for a high efficiency generator. This informed the choice of turns per coil, optimizing between performance and voltage constraints. The fusion of calculations, simulations, and decision-making produced a synchronous generator that meets design specifications while harmonizing performance and practicality. This showcases the synergy of engineering expertise and computational tools in shaping a promising future for advanced generators.

4.7 Torque Ripple and Cogging Torque

The culmination of this phase in the electric generator design process involved a series of meticulous simulations, each shedding light on critical aspects of the machine's behavior. A simulation was conducted to analyse the torque variation by dividing the polar step of the 1 mm machine model into 90 points, and the results were recorded for each point. For enhanced accuracy, this simulation was executed using a non-linear ferromagnetic material, accounting for saturation effects. The resulting torque curve perfectly matched the one depicted in Figure 14. This

exceptional outcome underscores the precision of the previously explained winding design.

Subsequently, a ripple torque simulation was orchestrated, further exploring the machine's response to varying conditions. This meticulous analysis illuminated a ripple of approximately 3.6%, offering valuable insights into the machine's resilience and performance under dynamic conditions. The ripple torque phenomenon, visible in Figure 15, served as a testament to the robustness of the design and its ability to handle real-world operational scenarios.

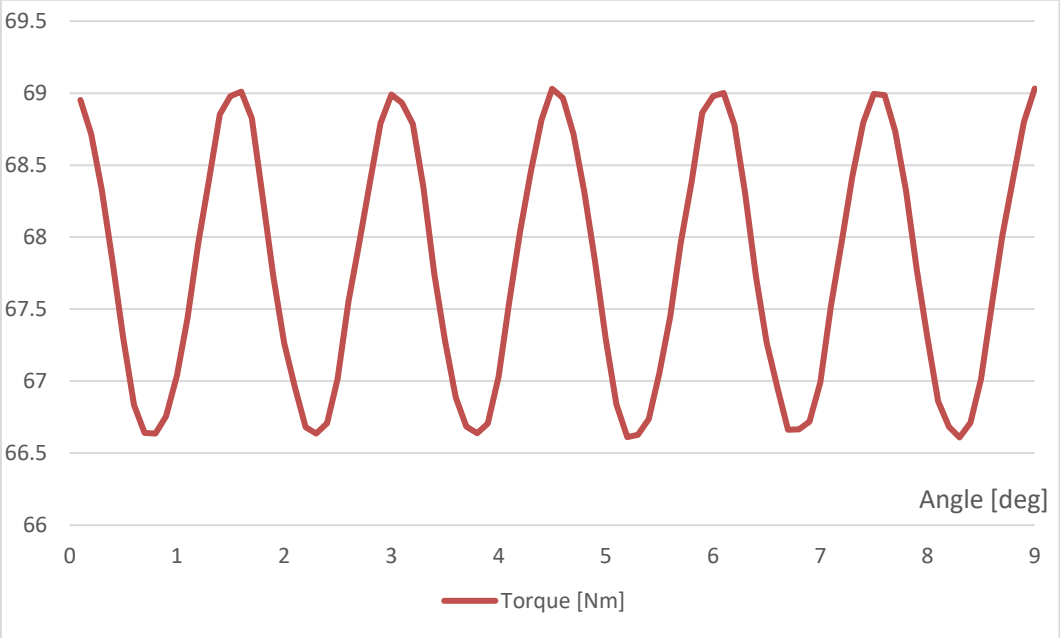

Figure 15: The torque ripple curve along a polar pitch with 370A of a machine current.

Closing this chapter of the design journey, a cogging torque simulation provided a final perspective on the generator's behavior. By dissecting the cogging step into 90 increments, the simulation uncovered a cogging torque pattern characterized by a modest peak below 0.1 Nm as shown in Figure 16. This subtle but vital element ensured a smoother operational experience while underscoring the precision and depth of the design process.

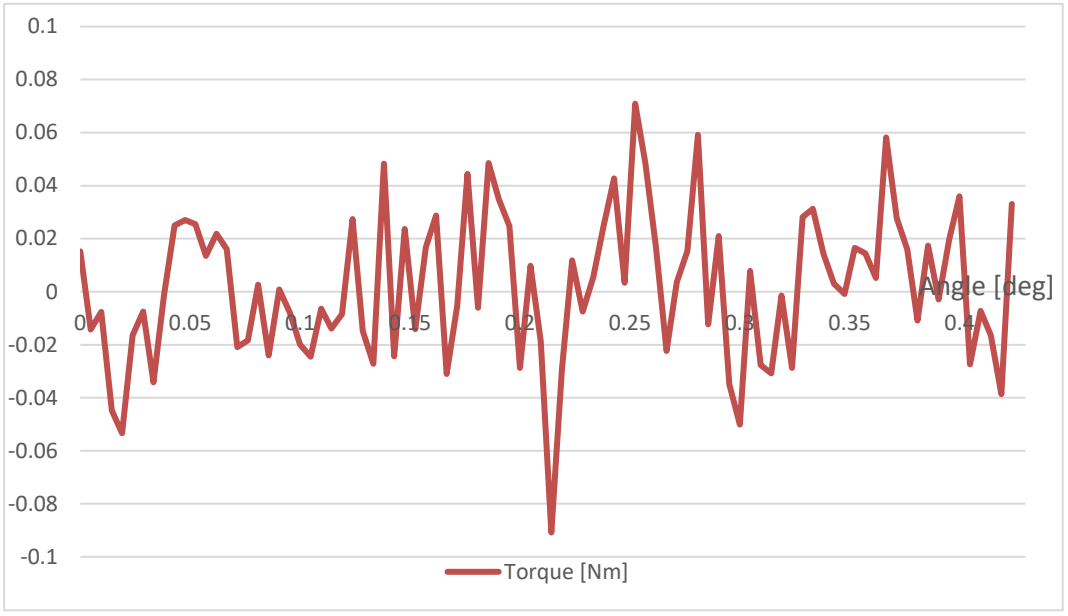

Figure 16: The torque cogging curve along a cogging step.

In sum, this meticulous simulation-driven exploration of torque, ripple, and cogging phenomena has fortified the foundation of the electric generator's design. The alignment between theoretical expectations and empirical results serves as a testament to the dedication, expertise, and thoughtful consideration invested in every aspect of the design process. Armed with this comprehensive understanding, the design team now embarks on the next phase, poised to transform these insights into a tangible and effective electric generator solution.

5 Second Generator Design

Following a comprehensive review of the outcomes from the initial synchronous generator design attempt with HPG s.r.l., several modifications have been requested to refine the project:

1. Modify the script to accommodate rectangular magnets instead of curved ones. The desired magnets are now specified as 43×30×8 mm in dimensions.
2. Widen the slot opening to 3.5 mm and extend the slot, creating a bottom slot radius of 6 mm. These adjustments are aimed at enhancing the mechanical feasibility of the machine. Then decrease the machine length (core length 870 mm) and optimize the inner stator diameter to minimize the utilization of ferromagnetic material, thus reducing costs.
3. Integrate water-cooling pipes (located under the teeth) with a diameter larger than 8 mm. These pipes need to be at least 5 mm away from the inner stator diameter and designed with a thermal transfer coefficient of 500 [W/(m^{2}K)].
4. Considering the stator's laminated structure, the rotor will be solid. As a result, it is necessary to segment the stator into symmetric sections and collaborate with the mechanical designer for further alignment with production considerations.

These refinements underscore a commitment to the interplay between mechanical and electromagnetic aspects, ensuring not only optimal performance but also practical manufacturability. Through this iterative process, the design aims to align closely with the specific requirements of HPG s.r.l., translating into a generator solution that strikes a harmonious balance between performance, feasibility, and economic considerations. This collaborative effort showcases the dedication to refining and advancing the generator design, paving the way for a more sophisticated and impactful solution that resonates with both technical excellence and practical implementation.

5.1 Changing the Generator Magnets

In the simulation script utilized in section 3.3, the decision was made to depict curved magnets that followed the contour of the inner rotor diameter for the sake of script simplicity. This representation is visible in Figure 17. However, in actual production, rectangular magnets are employed instead of curved ones. The company's preference is rectangular magnets with dimensions of approximately 43×30×8 mm. To achieve a simulation that closely mirrors reality, the script was adapted to incorporate the rectangular magnets as per the production specifications, as depicted in Figure 18.

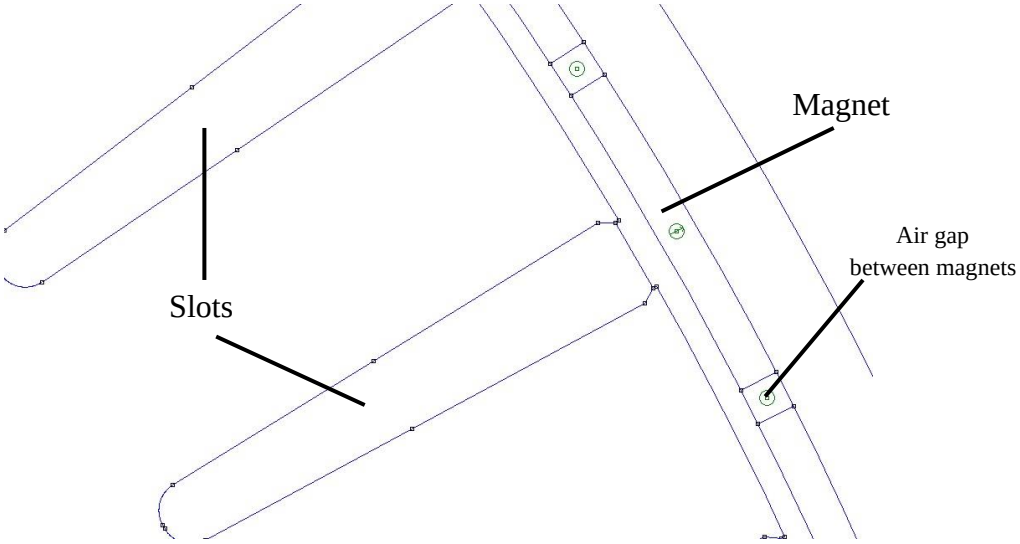

Figure 17: Cross section of the electric generator with curved magnets.

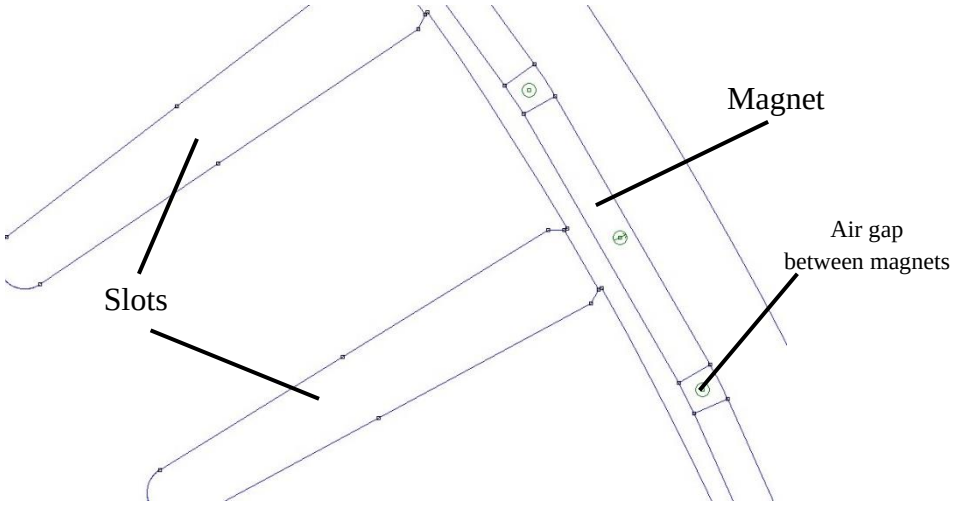

Figure 18: Cross section of the electric generator with rectangular magnets.

By making this adjustment, the simulation results are more closely with the practical manufacturing process, ensuring that the generated data reflects the expected performance of the generator in a real-world context. This modification not only enhances the accuracy of the simulation but also facilitates a more precise design process for the production stages.

5.2 Sizing of Slots and Machine Length

In pursuit of reducing the machine's overall length and optimizing the internal diameter of the stator, a pivotal decision was made to enhance the magnetic field strength within the stator teeth. The augmentation aimed at elevating the magnetic field intensity from 1.5 T to 1.75 T, constituting a 17% increase. Alongside this modification, an additional adjustment involved modifying the geometry of the stator slots. Specifically, the slot opening was expanded to achieve a width of 3.5 mm, coupled with a slot bottom radius of 6 mm.

With these design modifications in place, a subsequent ripple simulation was executed, incorporating the revised slot dimensions and assuming a magnetomotive force (MMF) of 2400 ampere-turns per coil; the determination of this MMF followed the procedural guidelines elucidated in section 3.2.4. Likewise, the angle of maximum torque was set to 0.1°, mirroring the conditions employed in previous simulations. The parameters NSB=1, NCP=1, and I_n=MMF were maintained to ensure alignment with these simulation parameters. These modifications were devised to ensure that the maximum magnetic field intensity (B) within the teeth corresponded to the targeted 1.75 T threshold.

Acknowledging the nonlinear behavior of the magnetic material, an iterative adjustment of the MMF was undertaken to ascertain the optimal value that would achieve the desired magnetic field strength within the teeth. Ultimately, a suitable MMF of 1600 ampere-turns was identified. At this magnetomotive force, the machine exhibited a torque production of 84.6 Nm, thereby determining a refined machine length of 710 mm.

In accordance with the methodology outlined in section 3.2.4, the subsequent step involved the calculation of NSB, NCP, and machine current (In). As a result of these calculations, the values of NSB = 15, NCP = 4, and I_n = 425 A emerged as the defining parameters that would govern the generator's operation under the revised design criteria. This iterative process of design refinement and simulation ensured the attainment of an optimized generator design that aligned effectively with the specified performance requirements.

5.3 Design of the Cooling System

Absolutely, the designed synchronous generator inevitably generates heat during its operation, necessitating effective cooling mechanisms to dissipate this heat and ensure optimal performance and longevity. Given the continuous contact between the rotor and water, the cooling of the rotor can be achieved without the need for additional cooling systems. However, the stator, operating in a distinct environment, requires a more tailored cooling approach.

To embark on the design of appropriate cooling systems, a fundamental step is the accurate assessment of the power losses within the generator. For the sake of simplification, an initial approach involves categorizing the power losses into two primary branches: copper losses and iron losses. Copper losses stem from the resistance of the winding conductors, leading to the conversion of electrical energy into heat. These losses are a direct result of the current flowing through the conductors and are proportional to the square of the current value. On the other hand, iron losses, also known as core losses, originate from the cyclic magnetization and demagnetization of the core materials due to the alternating magnetic fields. These losses manifest as hysteresis losses and eddy current losses within the magnetic core. By accurately quantifying these power losses, a clear understanding of the heat generated within the generator can be gained. This data then serves as the foundation for the design of efficient and effective cooling systems, tailored to address the specific cooling requirements of each component.

For the stator, operating within an idyllic hydropower environment, a forced water cooling system presents itself as a viable and efficient solution. The abundance of water resources provides an ample opportunity to harness this natural cooling medium, effectively carrying away the heat generated in the stator windings and the core.

In essence, the division of power losses into copper and iron losses provides a strategic starting point for the design of cooling systems that align with the generator's operational demands. This approach not only ensures that the generator operates within safe temperature limits but also optimizes its overall efficiency and reliability, culminating in a meticulously designed synchronous generator that efficiently harnesses hydropower while maintaining its performance standards.

5.3.1 **Copper Power Losses**

Through simulations, the crucial parameters for constructing the machine's winding configuration were derived. These parameters include the number of turns per coil (NSB) and the number of parallel circuits (NCP). Leveraging this information alongside the count of slots (N_C) and the overall machine length (L_n), the length of a single phase winding (L_{phase}) and the area of a single coil winding wire (S_w) can be calculated.

The L_{phase} calculation is made possible by referencing Equation 5, wherein L_{arc} represents the average arc length between two consecutive slots.

$$\mathrm{L_{phase}} = \frac{NSB * N_C * (2 * L_n + 2 * L_{arc})}{3 * NCP} = 162.8\, m$$

Equation 5

With the determination of L_{phase}, the area of S_w can be deduced as depicted in Equation 6. The slot fill factor (C_r), set at 0.5 in our scenario due to the usage of circular wire, and the number of active turns per slot (N_S) is set to 2, for a dual-layer slot configuration, are the key factors in this calculation.

$$\mathrm{S_w} = \frac{S_C * \frac{C_r}{N_S}}{NSB} = 28.68\, mm^2$$

Equation 6

Armed with the values of L_{phase} and S_w, the resistivity of copper at 20° C (ρ_{cu}) comes into play, enabling the calculation of the phase resistance (R_f) at 20° C according to Equation 7. This vital parameter forms the foundation for the subsequent calculation of copper losses within the winding.

$$\mathrm{R_f} = \rho_{cu} * \frac{L_{phase}}{S_w} = 0.131\ \Omega$$

Equation 7

Upon quantifying the phase resistance, the copper loss (P_{cu}) can be calculated using Equation 8, offering insight into the magnitude of power lost due to electrical resistance within the winding. This comprehensive analysis of copper losses serves as a pivotal step in the overall assessment of the machine's performance and efficiency, providing essential information for the design of effective cooling strategies and the optimization of the generator's operational characteristics.

$$P_{cu} = 3 * \left(R_f * \left(\frac{I_n}{NCP} \right)^2 \right) * NCP = 17.69 \text{ kW}$$

Equation 8

5.3.2 Iron Power Losses

Having meticulously calculated the copper losses, the task of estimating iron losses emerged as a pivotal endeavor. This entailed the determination of the iron's cross-sectional area (A_{Fe_s}) within a given machine section, a task accomplished through the adept use of finite element software (FEMM). Furthermore, the datasheet of the M800-100A laminated material proved indispensable, offering insights into the iron loss values for an induction of 1.5 T and a frequency of 50 Hz, succinctly denoted as P_{Fe_50Hz} = 8 W/kg.

The deliberation on induction and frequency warrants elaboration. The selection of an average induction of 1.5 T reflects a balanced approximation, while the frequency choice of 50 Hz was strategic. Although higher than the envisaged operational frequency, this selection ensures a prudent overestimation of iron losses, consequently enhancing the anticipated machine efficiency. Such judicious choices underscore the commitment to a design that transcends theoretical ideals and translates into real-world excellence.

Incorporating key machine specifications, such as the machine length (L_n = 710 mm) and the specific weight of iron (p_{s_Fe} = 7874 kg/m³), the iron loss can be elegantly quantified using the formidable Equation 9. By delving into the intricacies of iron losses, which encapsulate both magnetic hysteresis and eddy current phenomena, the comprehension of energy dissipation within the generator gains depth. This nuanced understanding not only enriches the generator's design but also augments its operational efficiency, symbolizing an endeavor characterized by meticulous engineering and visionary foresight.

$$P_{Fe} = A_{Fe\_s} * L_n * p_{s\_Fe} * P_{Fe\_50Hz} = 13.11 \text{ kW}$$

Equation 9

5.3.3 Calculation of the Cooling Pipes

As the copper and iron losses have been diligently determined, the next pivotal step involves aggregating these losses to ascertain the total dissipated power (P_t), a critical parameter necessitating management through the cooling system, as elegantly described in Equation 10.

$$P_t = P_{Cu} + P_{Fe} = 30.8\ \text{kW}$$

Equation 10

During the last collaborative meeting with the company, a consensus emerged regarding the design of the hydraulic circuit. It was decided to adopt a convective thermal dissipation coefficient (C_{st}) of 500 W/(m²·K) and a temperature differential (ΔT) of 30°C between the inlet and outlet of the cooling pipes. Armed with these parameters, the heat exchange surface area, defined by the periphery of the pipes per unit length of the machine, was calculated using Equation 11.

$$S_{pipe} = \frac{P_t}{C_{st} * \Delta T} = 2.05\ m^2$$

Equation 11

Further discussions led to the choice of cooling pipes with a diameter exceeding 8 mm, necessitating the allocation of one cooling pipe for each stator tooth. As a preliminary design effort, cooling pipes with a diameter (D_{pipe}) of 12 mm were considered. Utilizing the known machine length, Equation 12 was applied to determine the required number of cooling pipes.

$$N_{pipe} = \frac{S_{pipe}}{\pi * D_{pipe} * L_n} = 76.7$$

Equation 12

Given the necessity for whole-number pipe counts and the presence of 84 stator teeth, it was proposed to implement 84 cooling pipes, each with a diameter of 12 mm, effectively assigning one pipes per stator tooth. This comprehensive approach to cooling system design reflects a meticulous attention to detail and a commitment to ensuring that the generator operates within optimal temperature ranges, upholding its performance and longevity.

5.3.4 **Pump Characteristics Calculation**

In the meticulous process of selecting an appropriate cooling solution for the synchronous generator, several critical considerations were made. Beyond merely determining the number of cooling ducts required, the design delved into the intricacies of tubing layout and fluid dynamics to ensure optimal cooling efficiency and the pump selection characteristics. One essential aspect was the configuration of the cooling pipes as they traverse the generator's stator. To facilitate efficient heat

dissipation, it was decided that the cooling pipes would execute a 180-degree bend when transitioning from one channel to the next. This alternating bending pattern, illustrated in Figure 19, helps evenly distribute the cooling fluid throughout the stator, mitigating the risk of hotspots and ensuring consistent cooling.

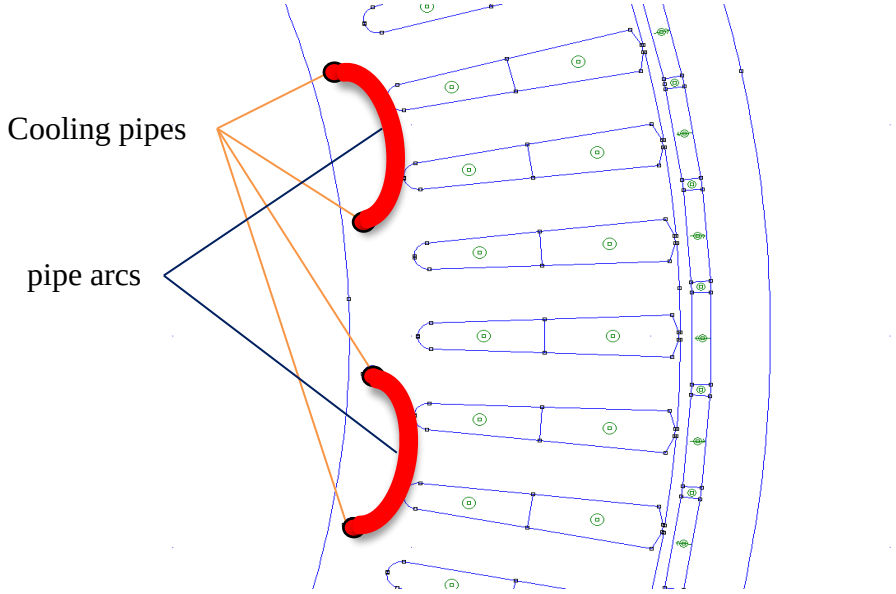

Figure 19: Cross section of the synchronous generator with the cooling system pipes.

The spacing between successive cooling channels, crucial for the accurate design of the cooling system, was determined through thorough analysis in FEMM. This analysis revealed that the length of the arc formed by the cooling pipes was consistent and measured L_{arc_pipe} = 58 mm. By multiplying this arc length and the machine net length by the number of cooling channels, the total length of cooling pipes required was established, as detailed in Equation 12.

$$L_{t\_pipe} = N_{pipe} * (L_n * L_{arc\_pipe}) = 64.5\ m$$

Equation 13

Additionally, to ensure that the cooling system could effectively dissipate the generated heat, it was imperative to estimate the minimum required flow rate for the cooling fluid. This calculation considered fundamental properties of water, including its specific heat capacity (C_{H2O} = 1.163 (W·hr)/(kg·K)) and water density (ρ_{H2O} = 997 kg/m³), ensuring that the cooling fluid could absorb and carry away heat efficiently. Equation 14 provided a straightforward means of calculating this essential flow rate.

$$Q_{pump} = \frac{P_t}{C_{H2O} * \Delta T * \rho_{H2O}} = 885\ \frac{liter}{hr}$$

Equation 14

In the comprehensive assessment of pump selection, an equally crucial factor alongside flow rate is pump pressure. To determine the required pump pressure, it was essential to first ascertain the viscosity of water at 25°C ($\eta_{H2O} = 8.9 * 10^{-4}$ Pa·s). Armed with this information, it became possible to calculate the hydraulic resistance of the cooling channels, as outlined in Equation 15.

$$R_{idr} = \frac{128 * \eta_{H2O} * L_{t\_pipe}}{\pi * D_{pipe}} = 1.128 * 10^8\ \frac{\text{kg}}{\text{m}^4 \cdot \text{s}}$$

Equation 15

Once the hydraulic resistance was determined, the next step was to find the pressure drop concentrated within the straight sections of the cooling channels, absent any bends. This calculation was achieved by multiplying the hydraulic resistance by the cooling fluid's flow rate, as presented in Equation 16.

$$\Delta P_{con} = R_{idr} * Q_{pump} = 0.277\ bar$$

Equation 16

Additionally, it was vital to account for pressure losses incurred within the bends of the tubing, constituting another significant source of hydraulic resistance. To compute these distributed pressure losses, the fluid velocity within the tubing was first determined using Equation 17.

$$\text{v}_{H2O} = \frac{Q_{pump}}{\pi * \left({}^{D_{pipe}}/_{2}\right)^2} = 2.174\ \frac{m}{s}$$

Equation 17

Subsequently, armed with knowledge of the fluid velocity, the number of cooling channels, and the fluid density, the distributed pressure losses were calculated as per Equation 18.

$$\Delta P_{dis} = 0.9 * N_{pipe} * \rho_{H2O} * \frac{{v_{H2O}}^2}{2} = 1.782\ bar$$

Equation 18

The sum of concentrated and distributed pressure losses yielded the total pressure losses, as illustrated in Equation 19.

$$\Delta P_t = \Delta P_{con} + \Delta P_{dis} = 2.059\ bar$$

Equation 19

These total pressure losses were instrumental in establishing the minimum pump pressure requirement. Typically, it is prudent to ensure that the pump's pressure output exceeds the total pressure losses by at least 1 bar, providing a safety margin. In this context, this translates to a minimum pump pressure of 3 bar.

In conclusion, the meticulous analysis of pump parameters, including flow rate and pressure, represents a pivotal step in the design of the cooling system for the synchronous generator. Accurately calculating the minimum required flow rate to ensure proper heat dissipation and the necessary pressure to maintain the cooling fluid's flow is crucial for the machine's correct operation. The selection of a pump with the correct specifications in terms of flow rate and pressure is essential to ensure that the cooling system operates efficiently, preventing overheating and performance losses. The approach of considering both concentrated and distributed pressure losses in the cooling channel pipes ensures a robust and reliable system.

Furthermore, sizing the pump with slightly higher pressure than the total pressure losses provides a safety margin, contributing to the stable and continuous operation of the cooling system. This meticulous evaluation of pump parameters underscores the importance of detailed design at every stage of the process, ultimately enhancing the success and reliability of the designed synchronous generator.

5.4 Splitting the Generator into Symmetric Divisions

In light of the impending realization of the generator, a comprehensive manufacturing strategy has been meticulously devised to achieve optimal material utilization and minimize wastage. The underlying principle of this strategy hinges upon balancing material efficiency with precision during the construction of critical components. Specifically, the design necessitates a substantial stator, ingeniously integrated into the internal structure of the helical assembly. Conversely, the stator is intended to be constructed using specialized laminations crafted from M800-100A material. These laminations are commercially available in the form of metal coils. However, they possess a width considerably narrower than the stator's overarching outer diameter, which measures 1225 mm. Consequently, a strategic decision was

made to partition the stator into symmetric segments, carefully matched to the width of the available laminations. The objective here is to ensure that, during the production phase, the stator can be optimally shaped onto these laminations through advanced manufacturing techniques such as laser cutting and precision pressing.

By implementing this production methodology, the aim is to significantly reduce material wastage, thereby enhancing the overall efficiency and precision of the generator manufacturing process. An exhaustive analysis of the machine's inherent symmetry led to two compelling options: dividing the stator into either four or six

symmetric segments. Following a comprehensive evaluation, the company opted for a six-part symmetric division, as illustrated in the figure below. This decision was primarily influenced by considerations related to the dimensions of the laminations, aligning with the overarching goal of achieving maximal material efficiency and precise construction.

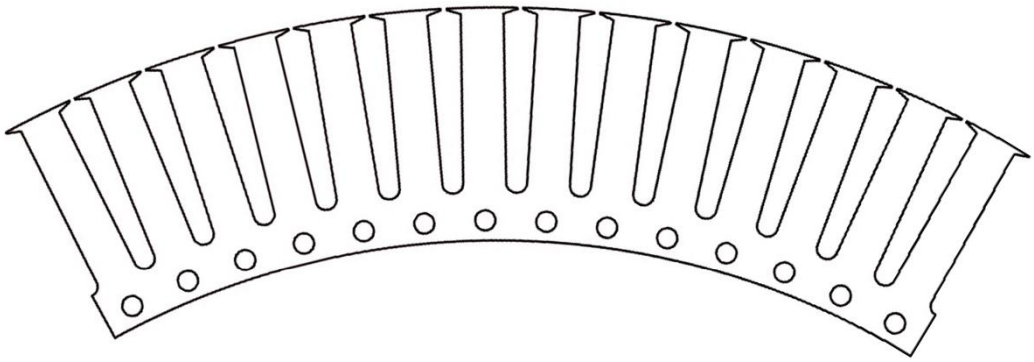

Figure 20: Six-part symmetric division of the generator stator.

6 Generator Control System

Following the results obtained from the second design phase, the decision was made to employ Matlab/Simulink[1] for simulating the control of the electrical machine. The primary objective at the outset was to utilize 4 parallel three-phases diode bridges (one bridge per each circuit, assuming the phase parallel paths used as independent windings) to convert the alternating voltage generated by the electric generator into direct current. Subsequently, a DC/DC boost converter should be used to control the output voltage, and finally a three-phase inverter [5] would convert this direct current back into synchronized alternating current suitable for connection to the low-voltage distribution grid at 400V, as illustrated in the figure below.

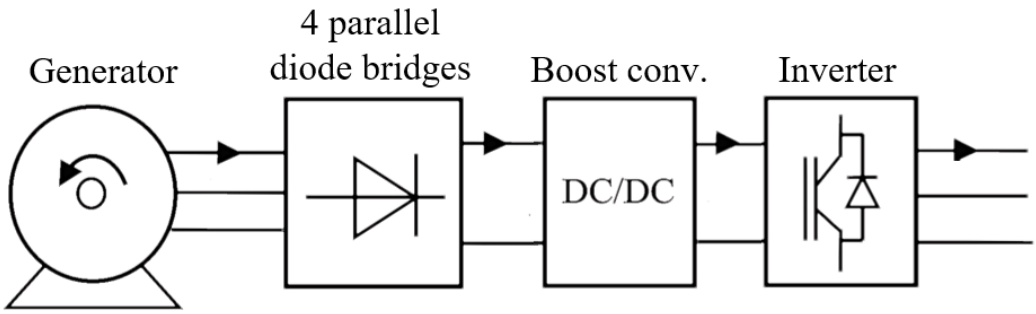

Figure 21: Generator control system [16].

However, during the preliminary modelling phase of the generator, an issue emerged concerning the utilization of the maximum flux of the permanent magnets as a modelling parameter for the electrical machine within the Simulink model. This resulted in an unexpectedly low voltage output, approximately two-thirds of the desired voltage.

Upon further investigation, it was discovered that the calculation of NSB (Number of turns per coil) and NCP (Number of parallel circuits) was based on the flux under maximum load conditions, which corresponds to the maximum torque point. This flux value was 3/2 times higher than the flux under no-load conditions, leading to an erroneous reduction in the calculated voltage. To fix this point, it was decided to recalculate NSB and NCP based on the no-load flux, and consequently, the no-load voltage E_0. The objective was to ensure that the three-phase line-to-line voltage under load conditions would indeed reach the desired 400V, addressing the voltage discrepancy that had been encountered.

[1] Simulink is a MATLAB-based graphical programming environment for modelling, simulating and analysing multidomain dynamical systems.

This correction in the design approach was undertaken to align the simulated model with the intended operational voltage requirements, ensuring accurate representation and reliable control simulations within the Matlab/Simulink environment.

Following the rectification of the previously mentioned issues, the engineering process transitioned to the design and development phase of the control system. However, prior to delving into detailed discussions regarding the various available solutions in the realm of power electronics for control systems, it was deemed crucial to establish a comprehensive understanding of the fundamental physical principles underpinning the control process.

The screw turbine, as an exemplar of volumetric turbines, operates in a manner where its rotational velocity is directly proportional to the flow rate it processes. Achieving precise control over a screw turbine necessitates an alignment with its torque curve, vividly illustrated in the accompanying diagram. As recognized, the electrical power output from the turbine constitutes the product of the mechanical torque it generates and the rotational speed it exhibits. Thus, to maximize the absorption of power at differing river flow rates, it becomes paramount to operate the turbine at specific speeds that correspond to the distinct flow rates encountered.

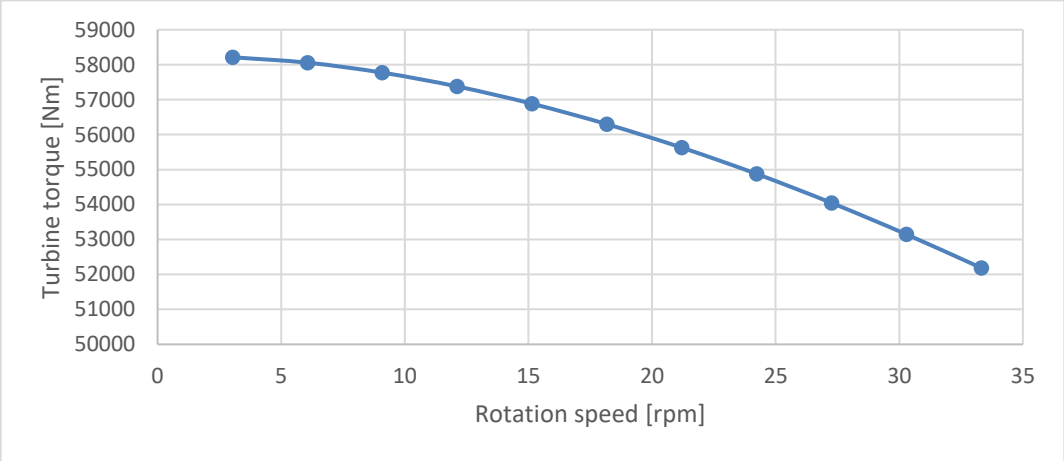

Figure 22: Screw turbine torque for varies rotation speeds.

To establish and uphold this precise control, measurements of water levels upstream and downstream of the turbine are consistently conducted. This measurement difference, referred to as the "water head" (ΔH), is contingent upon the instantaneous river flow rate. As such, when the river flow rate experiences fluctuations, there arises a necessity to calibrate the speed of the screw turbine. By adjusting the turbine's speed, the system endeavours to ensure that the head remains in alignment with the desired reference level (ΔH_{des}). Hence, as the flow rate within the river undergoes fluctuations, prompt and precise alterations in the screw turbine's

rotational speed are employed. This, in turn, enables the maintenance of a head difference that corresponds to the predefined reference head level (ΔH_{des}).

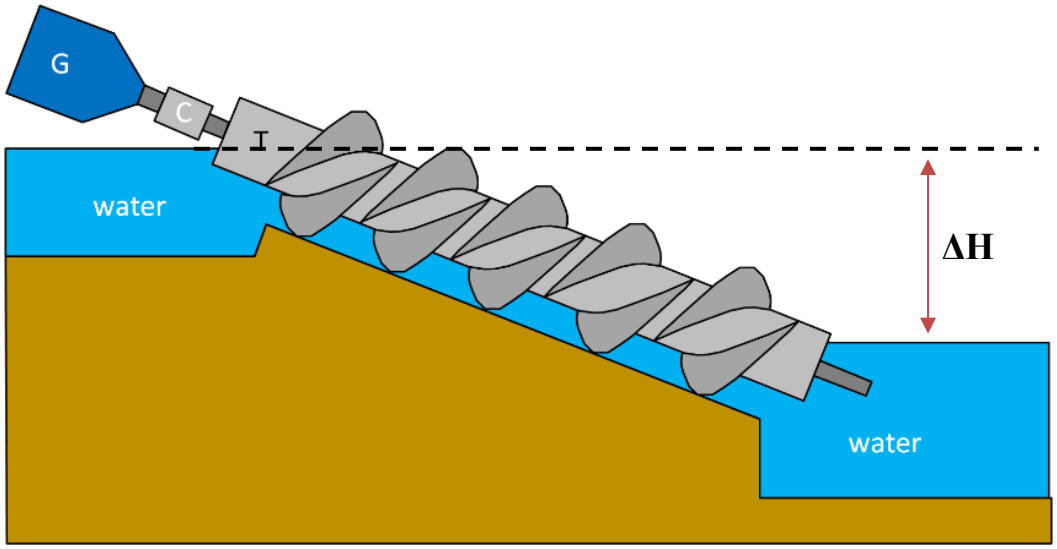

Figure 23: Screw turbine speed control.

With this comprehensive understanding of the control dynamics in place, the automatic control system is structured as illustrated in the schematic below. Central to this control system is the calculation of an "error" – a metric that emerges from the disparity between the aspired head level and the contemporaneous head measurement. The precise quantification of this error becomes the pivotal parameter for minimization, and this is facilitated through the employment of a PID (Proportional-Integral-Derivative) controller. The PID controller operates systematically, iteratively, and autonomously in response to variations in this error magnitude. It adjusts the speed of the generator with the overarching objective of curtailing this error to the greatest extent possible.

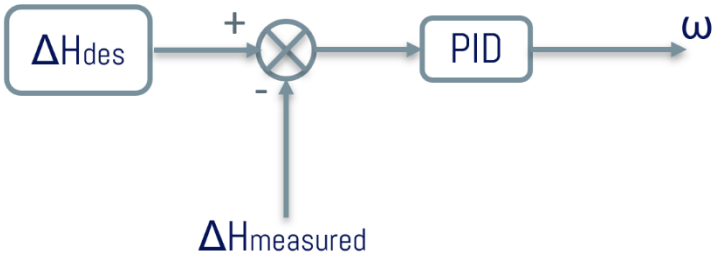

Figure 24: Control system for traditional screw turbines.

To effectively implement this intricate speed control system, it is imperative to harness the capabilities of power electronic systems [17]. In the chapter, we will

embark on a comprehensive exploration of four distinct solutions, each tailored to facilitate the realization of this form of speed control.

6.1 Diode bridges and Boost Converter

The necessity for precise control over the generator is underscored by its operational requirement to function within a variable speed range, specifically between 3 and 30.3 RPM. This range of rotational speeds corresponds to an electrical frequency output that spans from 2 to 20 Hz. As evident from Equation 20, the generator's phase voltage (E) is directly contingent upon various parameters, including magnetic flux per pole (Φ), the number of turns in the stator winding (N_s), electrical frequency (f), and the winding coefficient (k_w). With this foundational knowledge, the control system was devised to absorb the maximum power generated at any rotational speed.

$$E = \frac{2\pi * \emptyset * N_s * f * K_w}{\sqrt{2}}$$

Equation 20

The control system itself is orchestrated with four diode bridges, one diode bridge per each single generator circuit. The bridges outputs are connected in parallel. Following the diode bridges, a DC/DC Boost converter takes center stage, increasing the output voltage. Ultimately, an inverter links the system to the low-voltage grid for power distribution.

The inverter's operation is meticulously controlled, utilizing feedback from the DC link voltage at its input. The inverter works diligently to maintain a constant DC link voltage, absorbing all the generatable power. However, it is essential to maintain machine current within the generator's nominal current, necessitating precise control. To achieve this, the Boost converter is integrated with current feedback control, ensuring that the three-phase current of the generator remains at its maximum value. This methodology enables the generator to deliver the maximum absorbable power output regardless of its rotational speed.

6.1.1 Boost Converter Design

As highlighted, the Boost converter, a vital component in this system, comprises an inductance (L), a capacitance (C), a rectifying diode, and a MOSFET electronic switch. The MOSFET switch alternates between open and closed states, inducing energy storage in the inductance when closed and releasing stored energy to boost the output voltage when opened. This process serves to increase the output voltage

concerning the input voltage, effectively adjusting it to the desired level. The figure below illustrates a Boost converter that takes in a direct current (DC) input and provides a higher DC output voltage to power a load [18] [19].

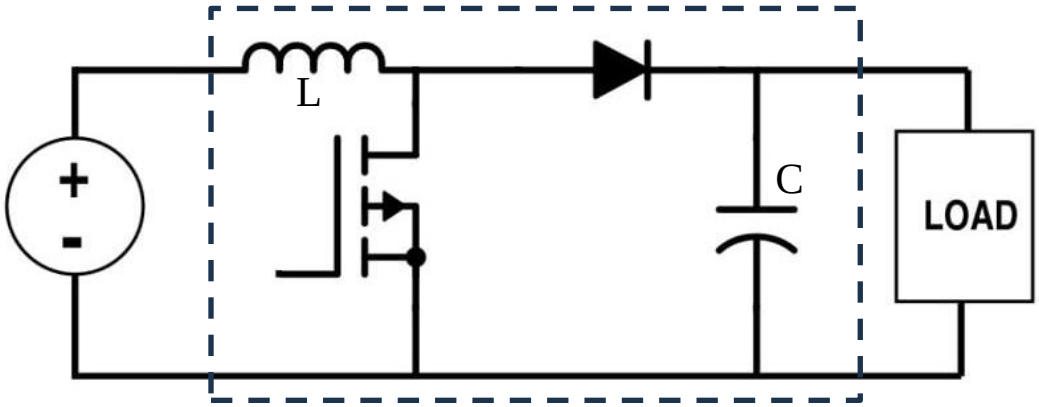

Figure 25: Boost converter diagram [20].

However, the practical application of the Boost converter poses significant challenges, primarily in calculating the required inductance and capacitance. To address these challenges, a methodological approach has been adopted, inspired by Texas Instruments' "Basic Calculation of a Boost Converter's Power Stage" [21]. This approach streamlines the design process by considering factors such as the switching frequency (f) of the MOSFET, the maximum input current (I_{Max}), the maximum input voltage to the converter (V_{Max}), the minimum input voltage (V_{min}), and the desired output voltage (V_{out}).

In an initial design attempt, a switching frequency of 10 kHz was selected. In adherence to the generator's nominal current requirement, I_{Max} was fixed to this maximum current value. The generator is designed to function within the variable speed range of 3 to 30.3 RPM, corresponding to minimum input voltage and a maximum input voltage of approximately 70V and 700V, respectively. For simplification purposes, calculations are based on the average voltage, resulting in a mean voltage, V_{mean}, of approximately 390V. The desired output voltage was determined to be variable from 560V to 600V.

In consideration of practical components and their inherent losses, an overall converter efficiency (η) of 85% was factored into the design. From these parameters, the maximum duty cycle and maximum current ripple were calculated using Equation 21 and Equation 22, respectively.

$$D_{Max} = 1 - \frac{V_{min} * \eta}{V_{out}}$$

Equation 21

$$\Delta I_L = 0.3 * \mathrm{I}_{Max} * \frac{\mathrm{V}_{out}}{\mathrm{V}_{mean}}$$

Equation 22

This information facilitated the calculation of the inductance (L) for the Boost converter, as shown below.

$$L = \frac{\mathrm{V}_{mean} * (\mathrm{V}_{out} - \mathrm{V}_{mean})}{\Delta I_L * \mathrm{V}_{out} * f} = 92\ \mu H$$

Equation 23

Subsequently, a desired output voltage ripple (ΔV_{out}) of approximately 10V was implemented. This criterion also allowed for the determination of the required capacitance value.

$$C = \frac{\mathrm{I}_{Max} * \mathrm{D}_{Max}}{\Delta V_{out} * f} = 2700\ \mu F$$

Equation 24

In summary, the design of the control system and the intricate interplay between the generator and the Boost converter exemplify the system integration required to meet the dynamic and challenging operational demands of the generator. The comprehensive approach adopted is poised to ensure the efficient utilization of energy resources, optimizing power generation across the entire spectrum of rotational speeds.

6.1.2 **Control System Modelling**

Having determined the construction elements' values for the Boost converter, the next step involved configuring the control system for potential simulations. The simulation environment employed here includes the Matlab Simulink software for numerical analysis, coupled with the SimScape Electric systems simulation package.

The schematic representation of the system to be simulated was carefully divided into three main blocks, as illustrated in the figure below. The first block serves to depict the generator with the four diode bridges – one for each circuit. The second block elaborates on the Boost converter, while the third block embodies the inverter, acting as the interface between the entire system and the distribution network. This inverter absorbs the maximum active power produced by the generator and transfers it to the grid [22].

It is worth noting that, at the output of the diode bridges, a capacitor with a capacitance of 2200 microfarads were strategically connected. This addition plays a crucial role in smoothing out the ripple effect in the system's output.

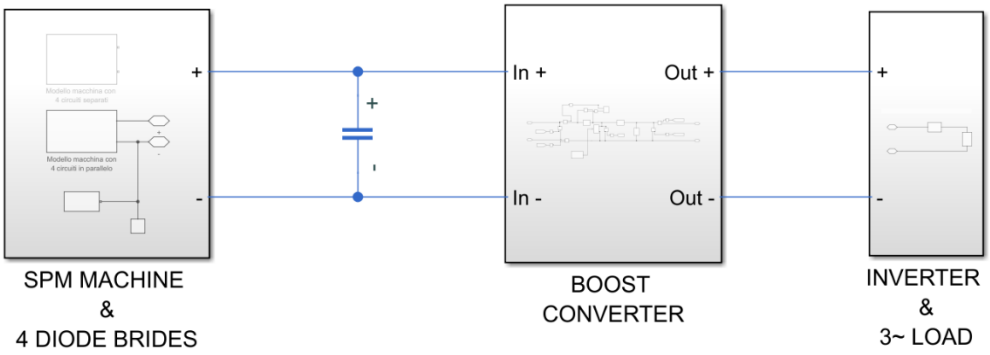

Figure 26: Diode bridges and boost converter control system

In the subsequent sections of this chapter, our focus will be on a more in-depth examination of each block depicted in the figure. This detailed analysis aims to provide a comprehensive understanding of how each component functions within the larger system architecture.

6.1.2.1 Generator and Diode Bridges Modelling

As explained earlier, the first block represents the generator along with four diode bridges, one for each electrical circuit. Given that the Simulink libraries lack a model for a unique surface magnet synchronous generator with four separate electrical circuits, the approach taken was to utilize a single-circuit electric machine model and modify its parameters to simulate it as if it were four circuits in parallel. This decision was made to ensure reduced computation time. Therefore, the "*PMSM*" (Permanent Magnet Synchronous Machine) model was chosen for the generator's representation.

Given that this machine is intended to function as a generator, it was connected to a mechanical system setting the generator's rotor at a constant speed. This approach allows for the evaluation of power generation at different speeds. Finally, a diode bridge was employed at the generator's output to convert the three-phase alternating voltage to a direct voltage with a certain amount of ripple.

This modelling strategy enables an effective assessment of the generator's performance under varying conditions, providing valuable insights into power generation across different rotational speeds. The diode bridge, by converting the

output voltage to direct current, sets the stage for subsequent stages of the system, facilitating the study of the generator's behavior under practical operating conditions.

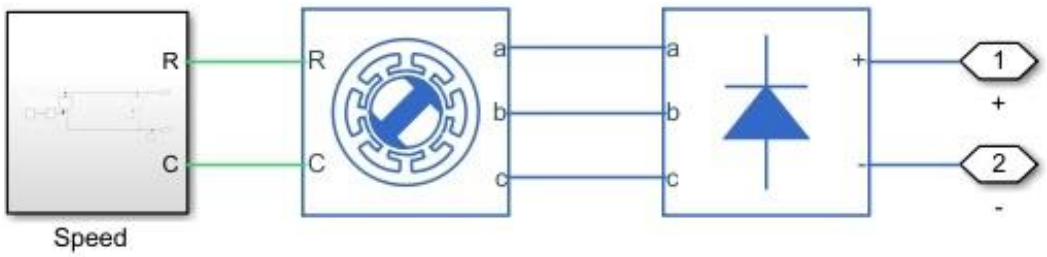

Figure 27: Generator and diode bride model

As elaborated earlier, the initial block in the simulation represents the speed of the generator. This is implemented through a SimScape mechanical block, specifically the "*Ideal Angular Velocity Source*," denoted in green in the accompanying figure. The purpose of this block is to translate a numerical input, signifying the desired speed, into the SimScape system, consequently establishing the actual speed of the generator.

The intricacy in Simulink simulations arises from the challenge of determining the initial time state of the simulation. To navigate this, the decision was made to commence the simulation with a velocity of zero and efficiently ramp up to the target speed within a brief interval, approximately 0.01 seconds. This transition is orchestrated through the integration of "*PS Ramp*" and "*PS Saturation*" blocks, visible in brown in the illustration below.

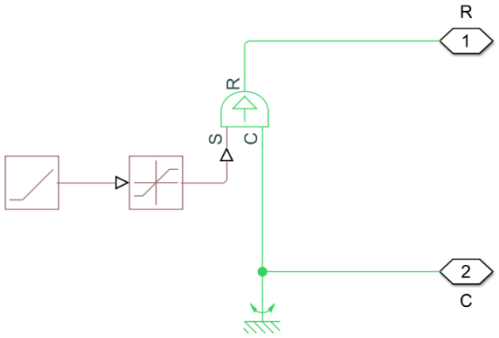

Figure 28: Speed control model

Moreover, this choice was prompted by the absence of a pre-existing Simulink library model for a synchronous generator with surface magnets configured with

four distinct electrical circuits. To circumvent this limitation, a model of a single-circuit Permanent Magnet Synchronous Machine (PMSM) was employed and subsequently modified to mimic a four-circuit parallel configuration. This pragmatic approach was adopted to ensure expedited computation times during the simulation.

The most challenging aspect of this modelling process was encountered in the representation of the generator. As previously mentioned, the generator would feature a single electrical circuit, yet it was necessary to manipulate its parameters to model it as if it had four parallel circuits.

Upon inspecting the "PMSM" generator model, it becomes apparent that certain defining parameters of the machine must be known to successfully model a synchronous generator:

- The number of pole pairs
- Permanent magnet flux linkage
- Stator d-axis inductance (L_d)
- Stator q-axis inductance (L_q)
- Stator resistance per phase

As elucidated in Chapter 3, the number of pole pairs was chosen to be 40 (equivalent to 80 poles) to ensure a maximally achievable electrical frequency for the machine. The same chapter also demonstrated how to determine the direct and quadrature axis inductances using the FEMM model. In Chapter 5, the calculation of the phase resistance was explained to estimate the power losses.

With this information, the permanent magnet flux linkage remained unknown. This flux represents the magnetic flux generated by the magnets and linked with the generator windings when the generator is not connected to any load. The flux was simply calculated using the Stator Flux Simulation method explained in Chapter 3. Once the three flux linkages (λ_A, λ_B and λ_C) associated with the three machine windings are known, the permanent magnet flux linkage can be determined using the equation below.

$$\lambda = \frac{2}{3} * \left(\lambda_A e^{-0i} + \lambda_B e^{\frac{-2}{3}\pi i} + \lambda_C e^{\frac{-4}{3}\pi i} \right)$$

Equation 25

Having determined the required flux linkage for the machine model, the next step was to understand how to employ this machine model to simulate four parallel circuits. During the design phase, the generator was conceived to have four circuits that are subsequently connected in parallel. This implies that in one machine circuit,

only 1/4th of the machine current flows. Consequently, from an external perspective, the machine has a resistance equal to 1/4th of the phase resistance. The same principle applies to the inductances. Therefore, the final machine model could be easily represented with 1/4th of the phase resistance and 1/4th of the direct and quadrature axis inductances. This concept is readily comprehensible by referring to the figure below, which illustrates the PMSM model.

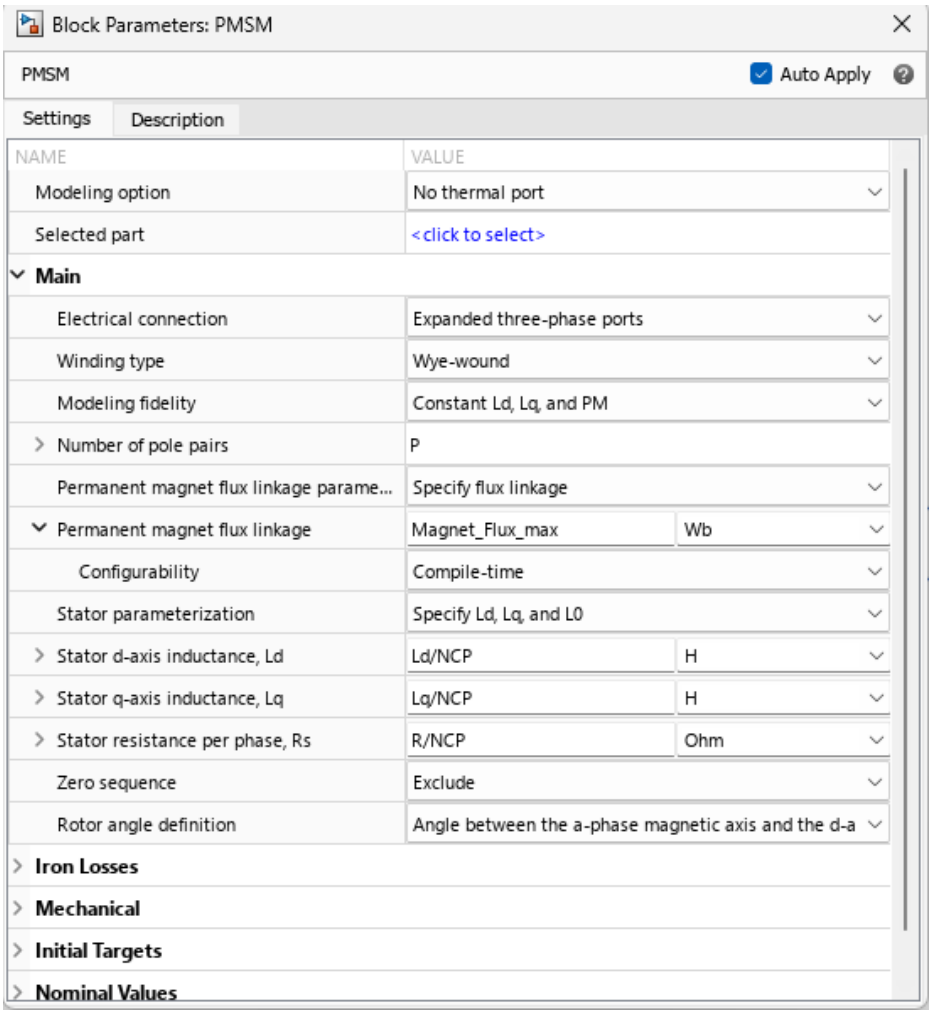

Figure 29: PMSM block parameters

Lastly, the generator is connected to a single diode bridge, which from a physical standpoint represents the parallel configuration of four diode bridges.

In conclusion, the design and simulation of the variable-speed generator system involve intricate considerations, spanning from the mechanical aspects of controlling the screw turbine speed to the electrical components of the generator and diode bridges. The simulation incorporates a permanent magnet synchronous machine (PMSM) model, modified to represent four circuits in parallel. The generator, operating within a speed range of 3 to 30.3 rpm, necessitates a careful

balance between mechanical and electrical parameters. Furthermore, the diode bridge configuration ensures efficient conversion of the generator's alternating current to direct current. The complex interplay of these components forms a comprehensive system that will be further explored and optimized in subsequent phases of the design process.

6.1.2.2 Boost Converter Modelling

In the second phase of the design, focus shifted to the modelling of the boost converter. While SimScape Electric provides pre-built models for static DC-DC converters, such as the Boost converter in our case, a decision was made to model the boost converter from scratch for experimental and measurement purposes. As known, a boost converter primarily consists of an inductance L, a capacitor C, a rectifying diode, and an electronic switch, which can be either a MOSFET or an IGBT. This configuration is illustrated in the figure below, where the input comprises the inductance and IGBT, followed by the rectifying diode, with the capacitor C positioned at the output.

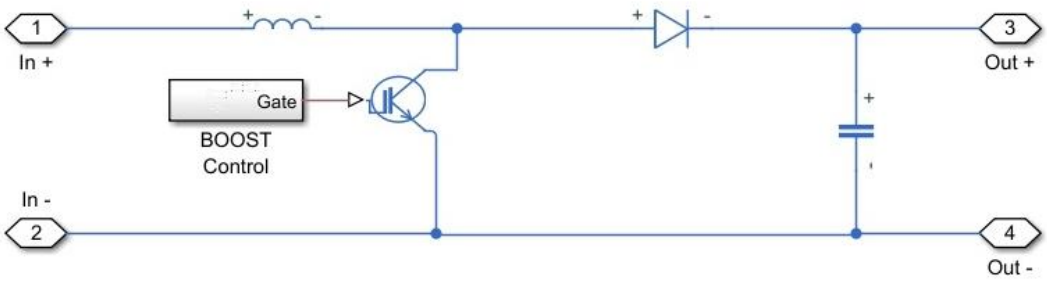

Figure 30: Boost converter model

As evident from the figure, the duty cycle of the IGBT must be controlled to ensure the maximum absorption of input current. Consequently, the "BOOST Control" block contains a proportional-integral (PI) control system, receiving as input the error derived from the difference between the reference current to be absorbed by the generator and the measured output current from the diode bridge. This control scheme is visualized in the figure below, where the "PWM Generator" block transforms the signal from the PI controller into the gate signal for turning the IGBT on and off.

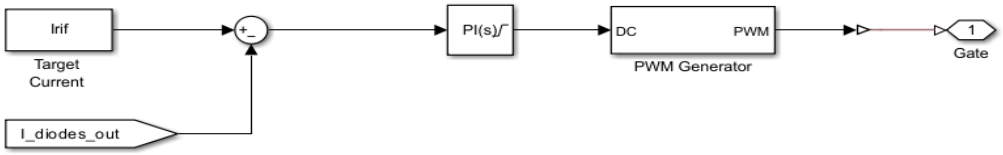

Figure 31: Boost control feedback system

As previously mentioned, the switching frequency for the IGBT in this simulation was set at 10 kHz, as calculated for the Boost converter. This detailed model provides insights into the dynamic behavior of the boost converter under varying conditions, allowing for a comprehensive understanding of its performance within the larger system.

In conclusion, the modelling of the boost converter from first principles has been a crucial aspect of the design process. While pre-built models are available, developing a bespoke representation enabled a deeper understanding of the converter's behavior under different conditions. The inclusion of a proportional-integral (PI) control system ensures precise regulation of the IGBT duty cycle, optimizing the converter's performance in absorbing the varying input current from the generator.

This detailed model not only facilitates experimental exploration but also serves as a valuable tool for comprehending the dynamic interactions within the broader system. The boost converter, a pivotal component in the power generation process, plays a vital role in transforming the variable voltage generated by the synchronous generator into a stable, high-voltage DC output. As the design progresses, the insights gained from this modelling phase will contribute to the overall efficiency and reliability of the system.

6.1.2.3 Inverter and Grid Modelling

Concluding the modelling phase, the remaining components to be represented are the inverter and the electrical grid. The inverter, a static converter comprising six power electronic switches, transforms direct current to alternating current. It also includes filters and synchronization systems for connection to the distribution grid, ensuring alignment with its frequency and phase. Modelling a real inverter with synchronization systems and an entire distribution grid demands extensive computational time for short-term simulations. For this reason, alternative approaches were considered for a more efficient representation.

As outlined earlier in this chapter, the inverter's control system is configured to absorb all the DC current at its input, maintaining the input voltage within the range of 560 V to 600 V. Consequently, the inverter can be modelled with this control concept in mind. As illustrated in the figure below, the inverter is simplified to an ideal DC voltage source set at 560 V and a rectifier diode. When the voltage at the inverter's input exceeds 560 V, positive current flows through the diode, entirely absorbed by the ideal DC voltage source. This simplified representation provides a practical yet computationally efficient means to simulate the intricate behavior of

the entire system. The engineering and computational simplicity of this approach makes it a valuable tool for understanding and optimizing the performance of the overall system.

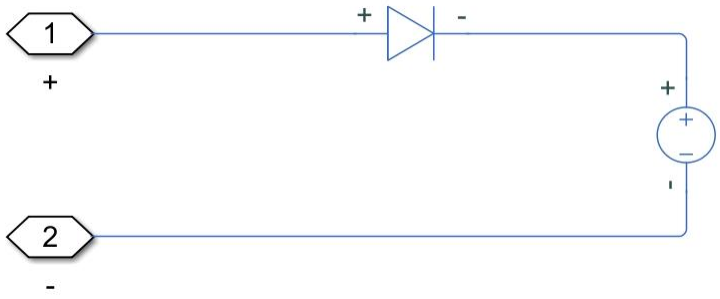

Figure 32: Simplified inverter and grid model

In conclusion, the modelling phase has successfully captured the dynamic behavior of the speed control, generator, and diode bridges, followed by the boost converter. The intricacies of the boost converter were explored, with a particular focus on the control system, ensuring maximum current absorption for optimal generator performance. The modelling approach considered practical elements, facilitating experimental observations and accurate representation.

Moving forward, attention turned to the inverter and its integration into the electrical grid. Recognizing the computational challenges of modelling a real inverter and distribution grid, a simplified yet effective representation was devised. The inverter's control system, designed to absorb DC current and maintain specified voltage levels, was incorporated into the model.

This holistic representation, while simplifying complex components, enables comprehensive system-level simulations. As the simulation framework takes shape, the subsequent phases will delve into detailed analyses, leveraging the modelled components to evaluate system performance and optimize its behavior under various conditions.

6.1.3 **Simulation Results**

Once the model was prepared with all its construction elements, the entire system was simulated to analyse its behaviour at various operating speeds. For these simulations, a reference current value of 160 A was set for the boost control system. For each rotation speed, the following parameters were observed:

1. Three-phase voltage across the generator terminals.

2. Three-phase current absorbed by the generator.
3. Active and reactive powers absorbed by the generator.
4. DC-link voltage at the input of the boost converter.
5. Output voltage from the boost converter.
6. Current to be compared with the reference one. This current is the one exiting the diodes and entering the boost converter.
7. Current output from the boost converter.

Therefore, for each speed, these seven parameters were analysed. Simulations were set for various speeds, and three operating points of the machine are presented:

- Operating point at 15 rpm.
- Operating point at 20 rpm.
- Operating point at 30 rpm.

For these operating points, the seven listed parameters were studied during the steady-state operation, excluding the initial transient where the machine accelerates from zero speed to reach the steady state. This choice was made for mathematical calculation convenience within the Simulink simulation system and does not reflect the actual transient behavior of the machine.

6.1.3.1 System Simulation with a Target Speed of 15 rpm

In the initial test, the generator was set to a speed of 15 rpm. The subsequent figures reveal interesting insights into the system's behavior. Firstly, the generator's three-phase voltage exhibits a square waveform due to the utilization of diode bridges, deviating from the expected sinusoidal pattern. However, the three-phase current maintains a sinusoidal shape, showcasing the system's ability to convert the unconventional voltage waveform.

Moving on to power characteristics, the third figure illustrates the active power absorbed by the generator, depicted in yellow, amounting to approximately 25 kW. Simultaneously, reactive power, represented in blue, is exchanged between the generator and the diode bridge, resulting in a net zero average over time.

The more intriguing aspects are captured in Figure 36, Figure 37, Figure 38 and Figure 39. The input voltage to the boost converter starts at around 280 V, and through the converter's action, it is elevated to 560 V at the output. This voltage transformation is accompanied by a reduction in input current from approximately 150 A to 45 A at the output of the boost converter.

These observations underscore the effectiveness of the boost converter in enhancing voltage levels while efficiently managing current, ultimately contributing to the optimization of power absorption within the system. Further analysis at different speeds will provide a comprehensive understanding of the system's performance across various operating conditions.

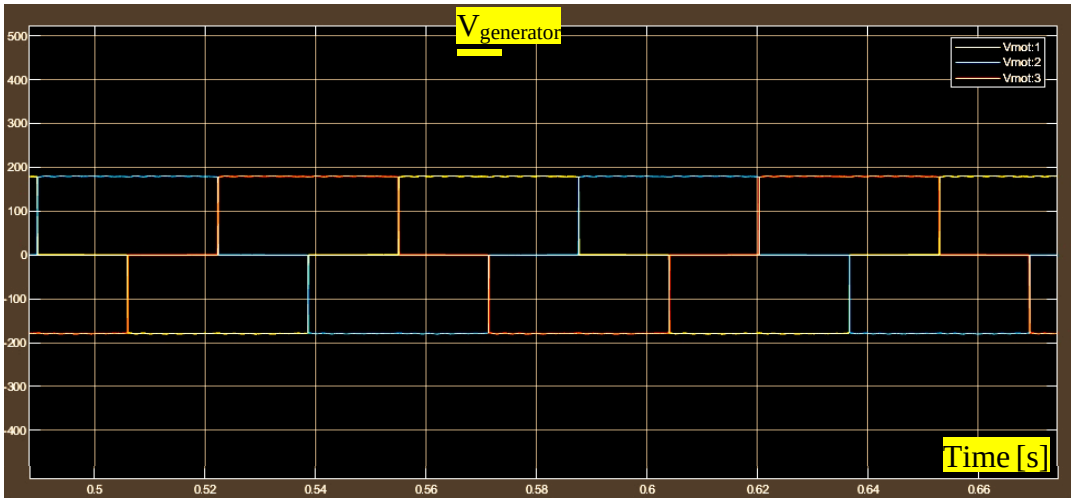

Figure 33: Generator's output voltage at 15 rpm

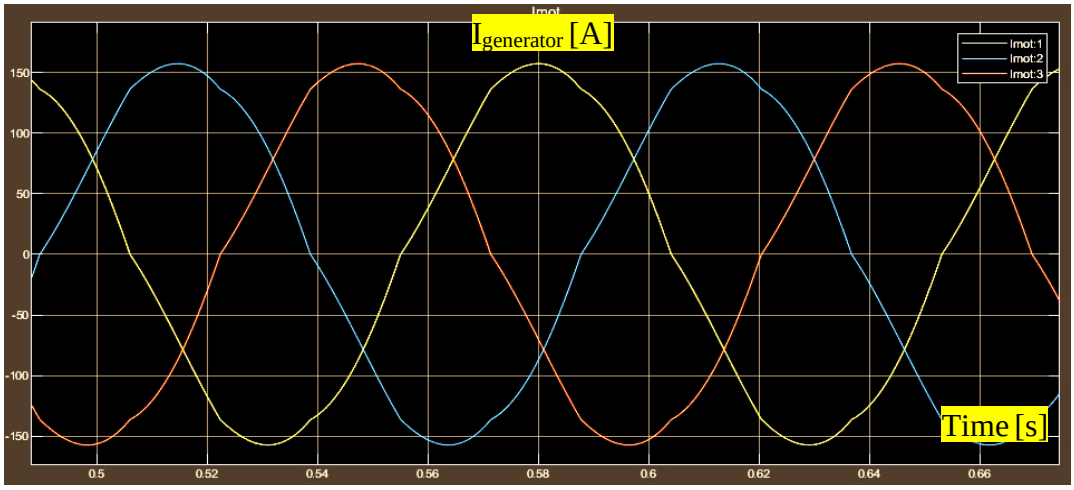

Figure 34: Generator's output current at 15 rpm

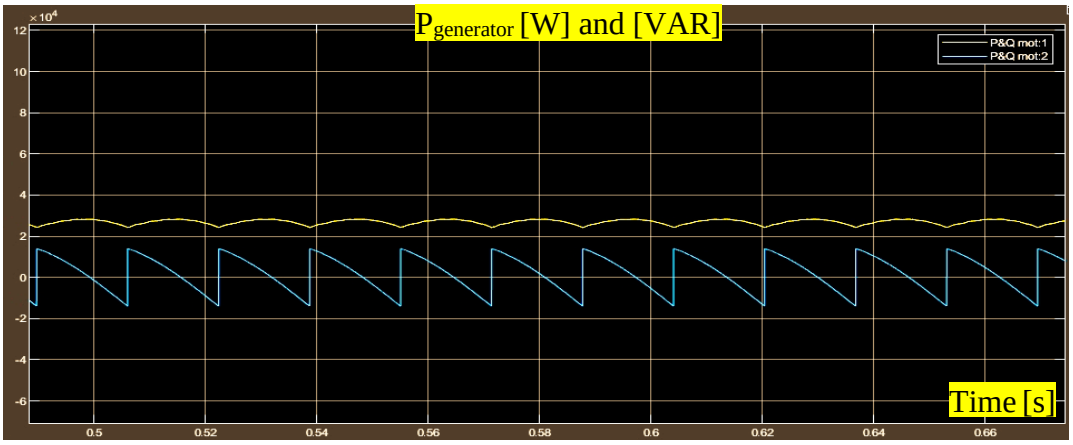

Figure 35: Generator's output power at 15 rpm

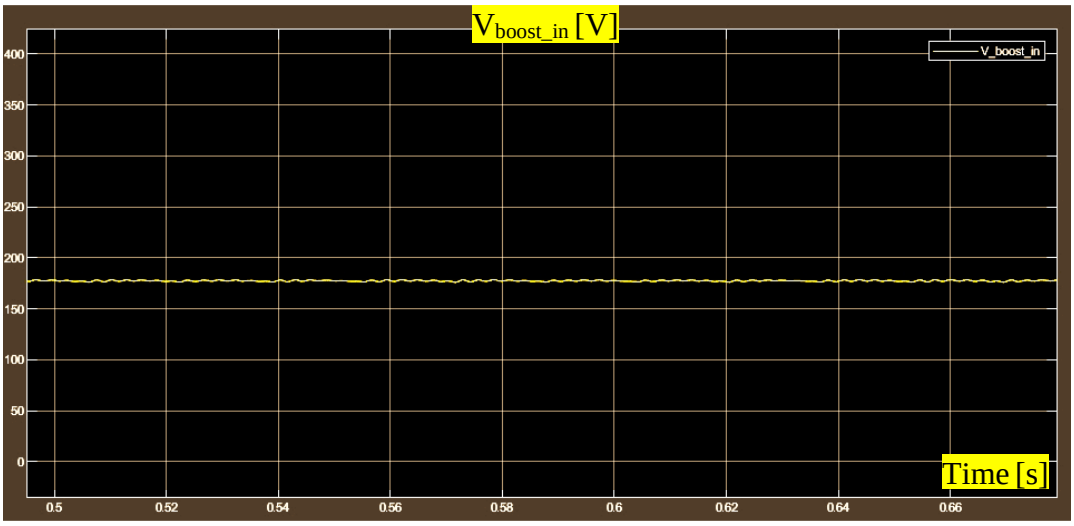

Figure 36: Boost converter's input voltage at 15 rpm

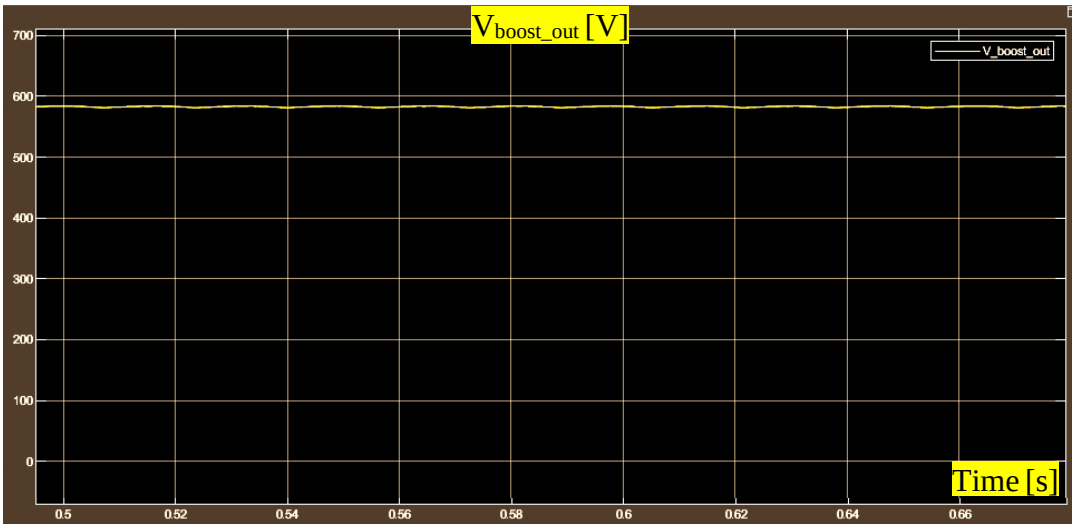

Figure 37: Boost converter's output voltage at 15 rpm

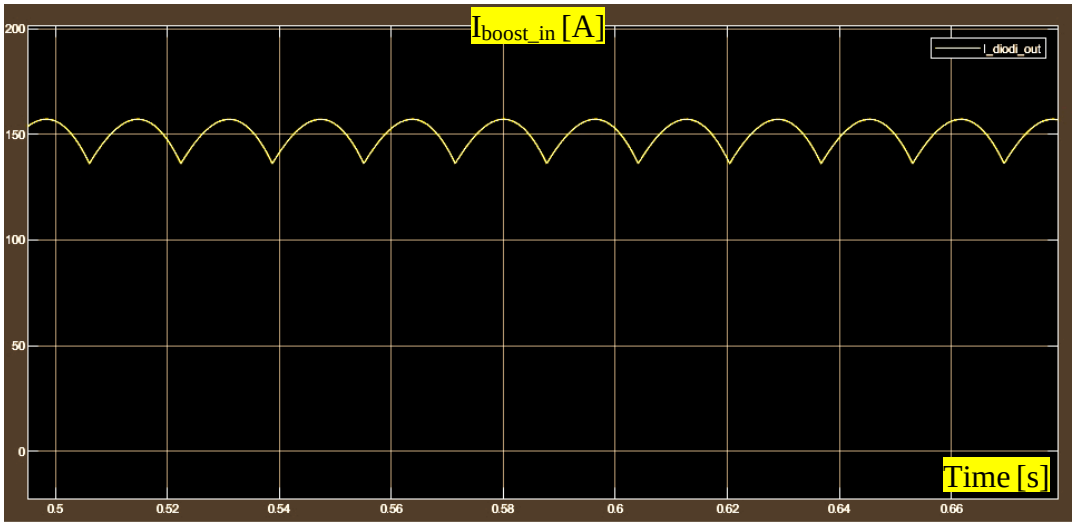

Figure 38: Boost converter's input current at 15 rpm

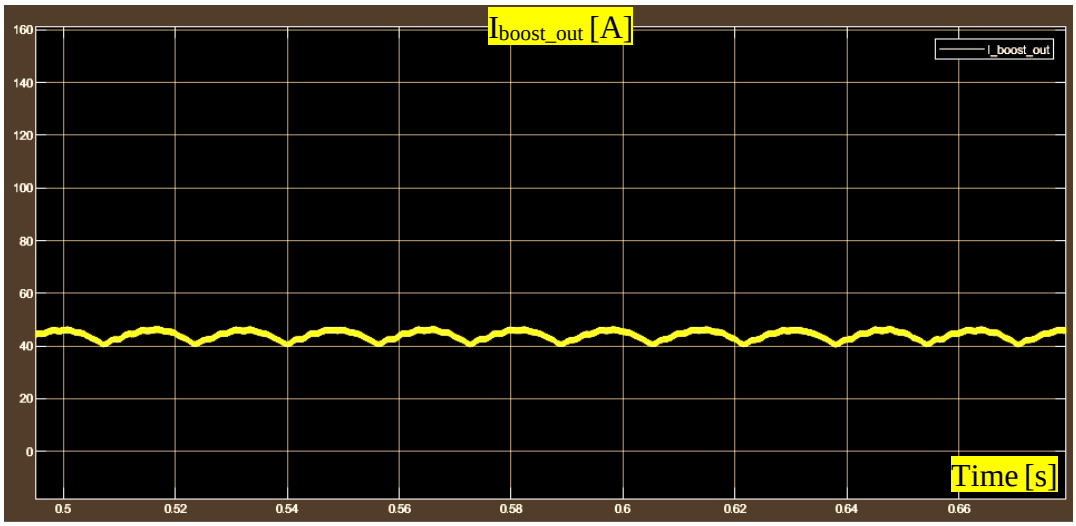

Figure 39: Boost converter's output current at 15 rpm

6.1.3.2 System Simulation with a Target Speed of 20 rpm

In this second scenario, the simulation is conducted at a generator rotation speed of 20 rpm, allowing for a comparison with the previous case at 15 rpm. The following seven figures present the same parameters for comparison, offering insights into the system's behavior as the generator speed increases.

As evident in the results, the three-phase voltage of the generator and, consequently, the output voltage from the diode bridge and the input to the boost converter exhibit an increase in amplitude with the higher generator rotation speed. The boost converter responds by attempting to elevate the voltage at its output, similar to the previous case.

Examining the currents, the three-phase current from the generator maintains a peak value similar to the previous case, resulting in the outgoing current from the diode bridge and entering the boost converter being consistent with the earlier scenario. However, the output current from the boost converter is greater than in the previous case, reaching approximately 60 A.

This alteration in the system's behavior has led to a shift in the profile of powers absorbed by the generator, resulting in an increase in active power to around 40 kW. The varying responses at different speeds highlight the dynamic nature of the system, showcasing its adaptability to changes in generator speed. Further exploration of additional speeds will provide a comprehensive understanding of the system's performance across a range of operating conditions.

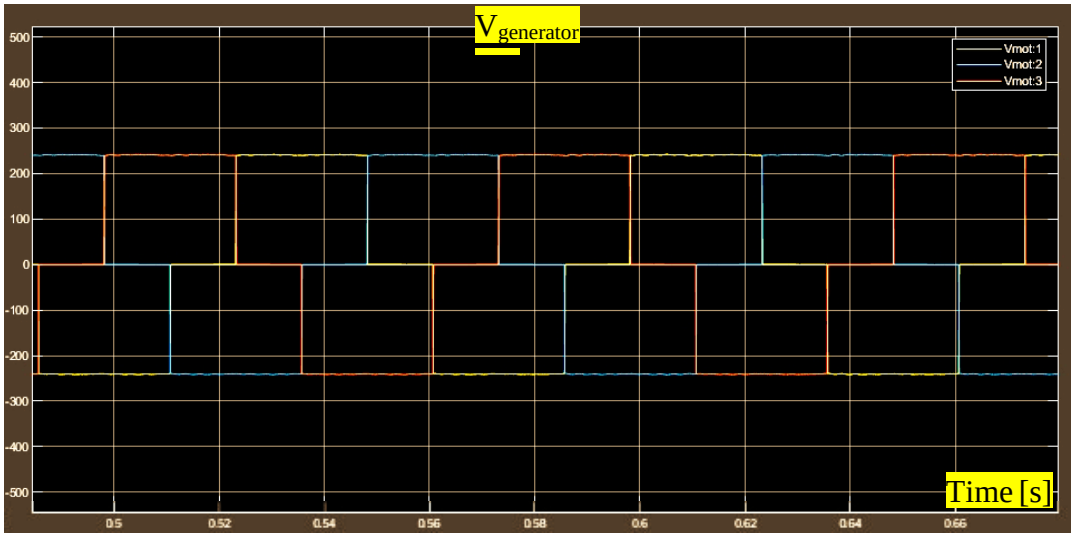

Figure 40: Generator's output voltage at 20 rpm

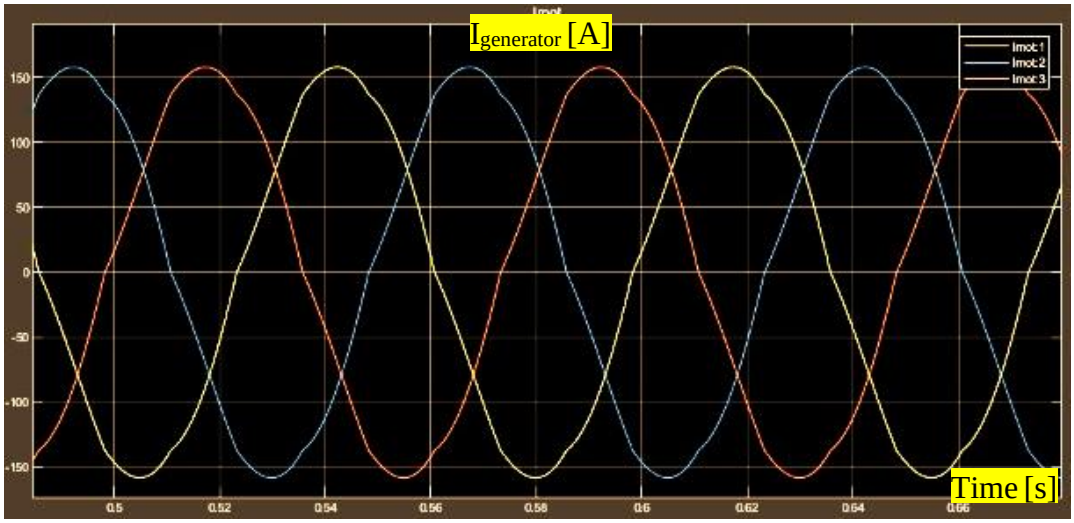

Figure 41: Generator's output current at 20 rpm

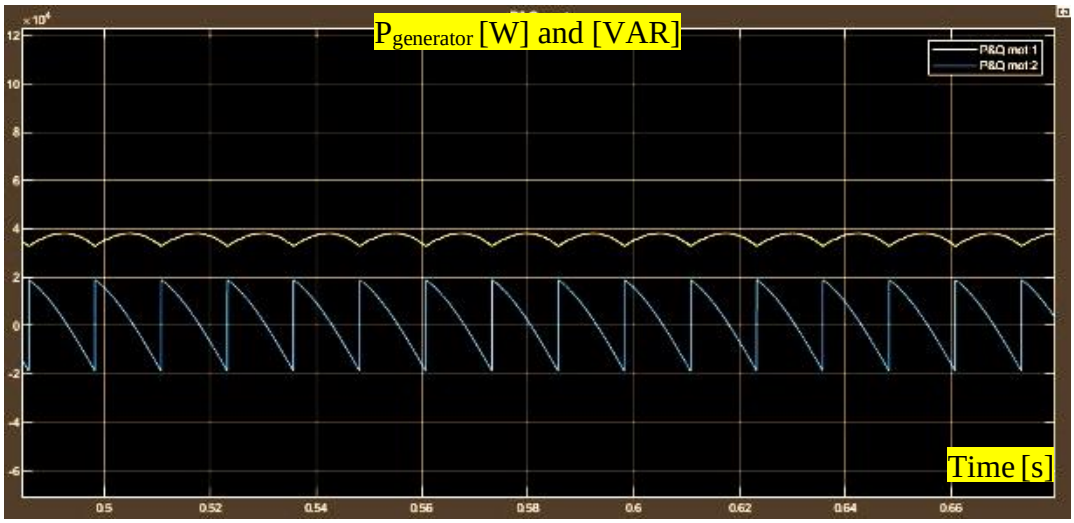

Figure 42: Generator's output power at 20 rpm

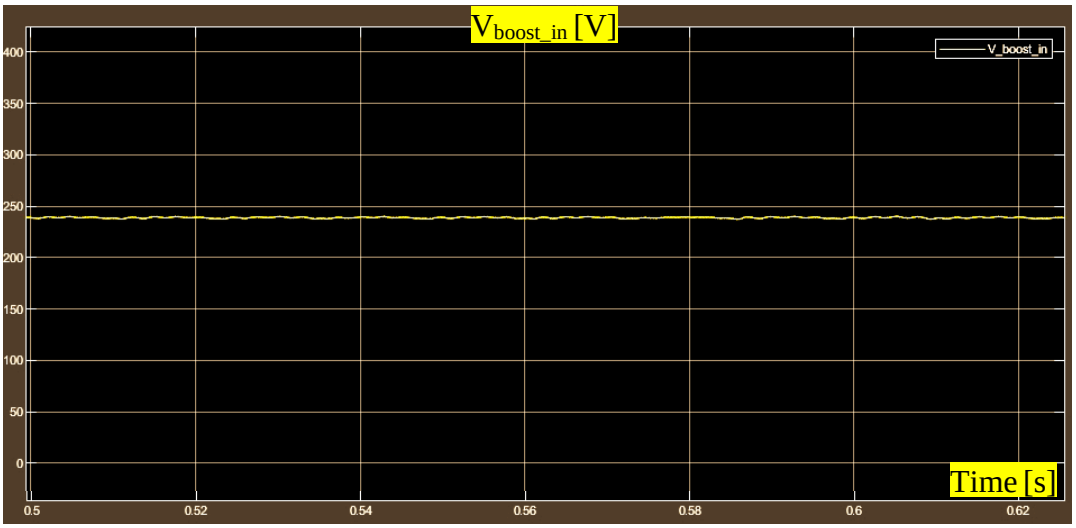

Figure 43: Boost converter's input voltage at 20 rpm

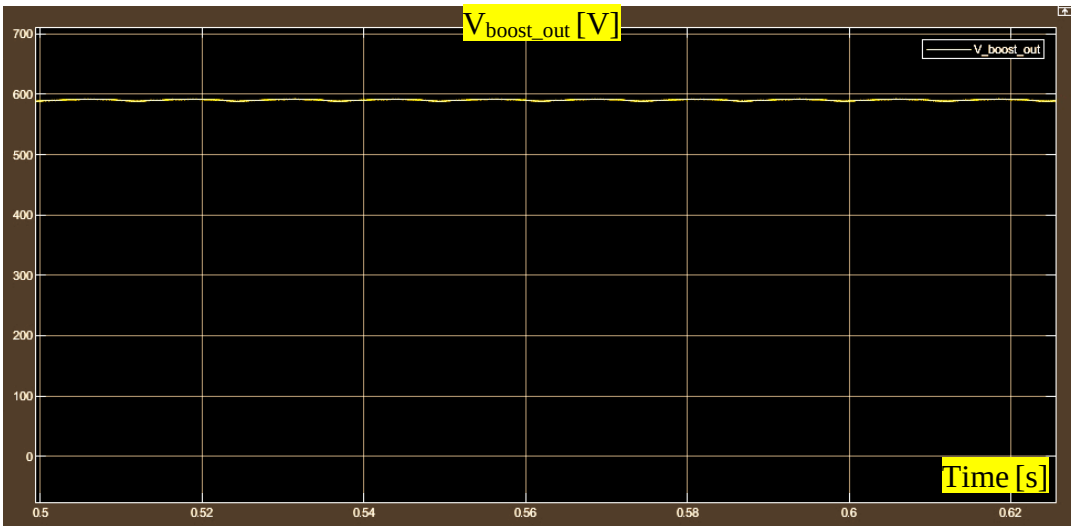

Figure 44: Boost converter's output voltage at 20 rpm

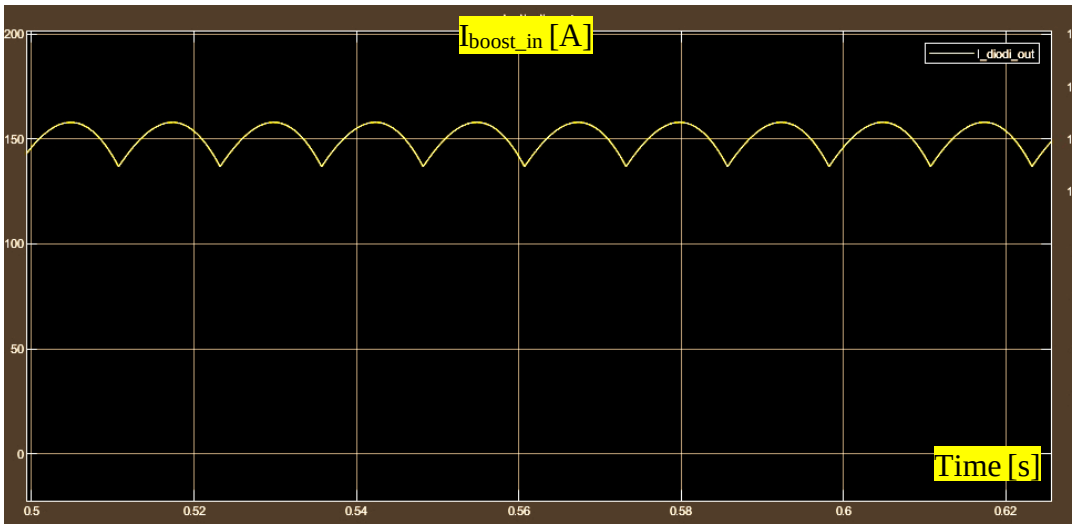

Figure 45: Boost converter's input current at 20 rpm

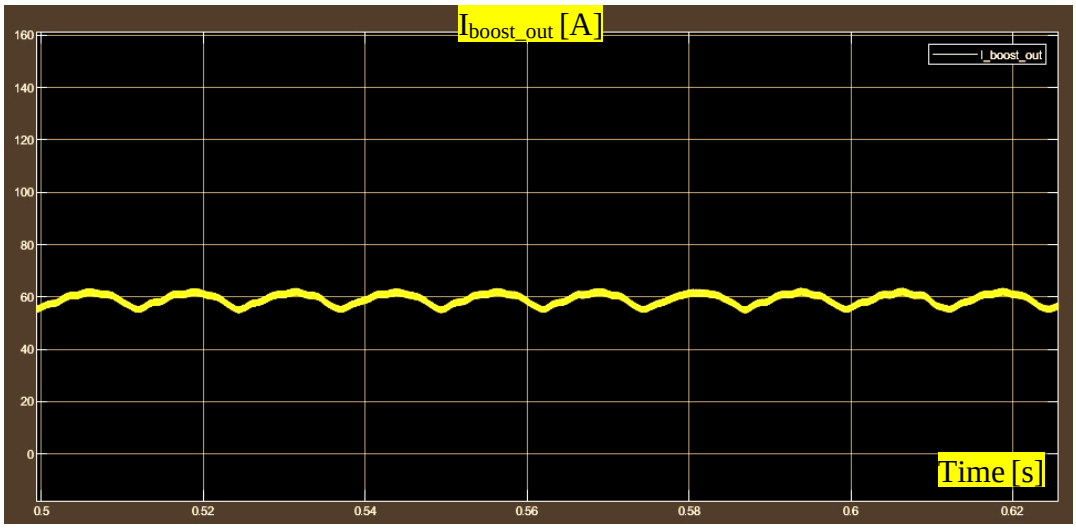

Figure 46: Boost converter's output current at 20 rpm

6.1.3.3 System Simulation with a Target Speed of 30 rpm

In this final scenario, the system's behavior at 30 rpm is examined. The notable increase in machine speed prompts an exploration of how this higher speed contributes to a rise in generated active power. The following figures illustrate how the acceleration in rotational speed leads to an upsurge in the three-phase voltage output from the generator and the active power generated by the generator.

As evident in the results, the enhanced speed of rotation has a direct impact on the three-phase voltage, causing a substantial increase. Consequently, this higher speed translates into a remarkable boost in the active power generated by the generator. This relationship emphasizes the influence of rotational speed on power generation, illustrating the system's dynamic response to changes in operating conditions.

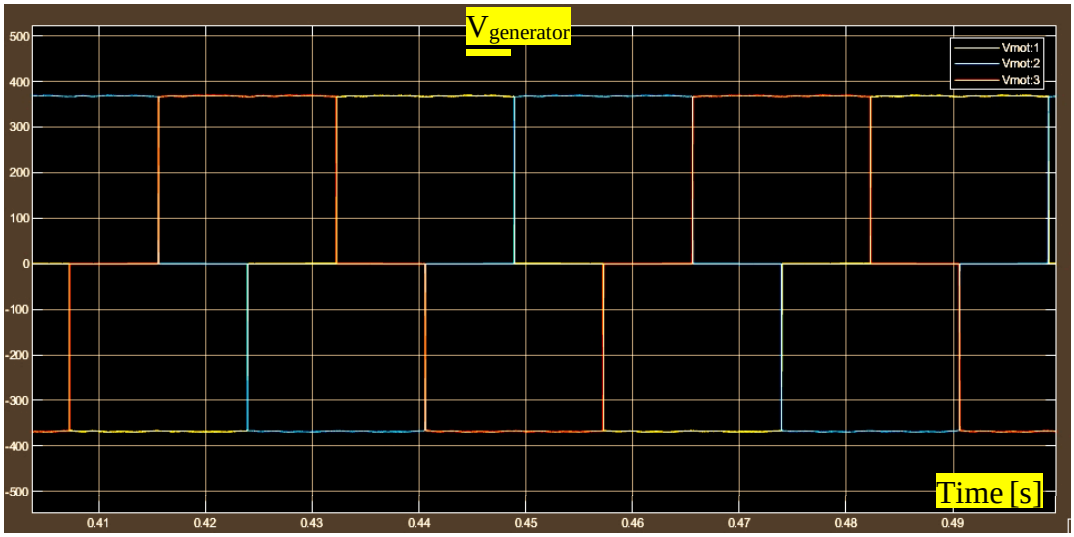

Figure 47: Generator's output voltage at 30 rpm

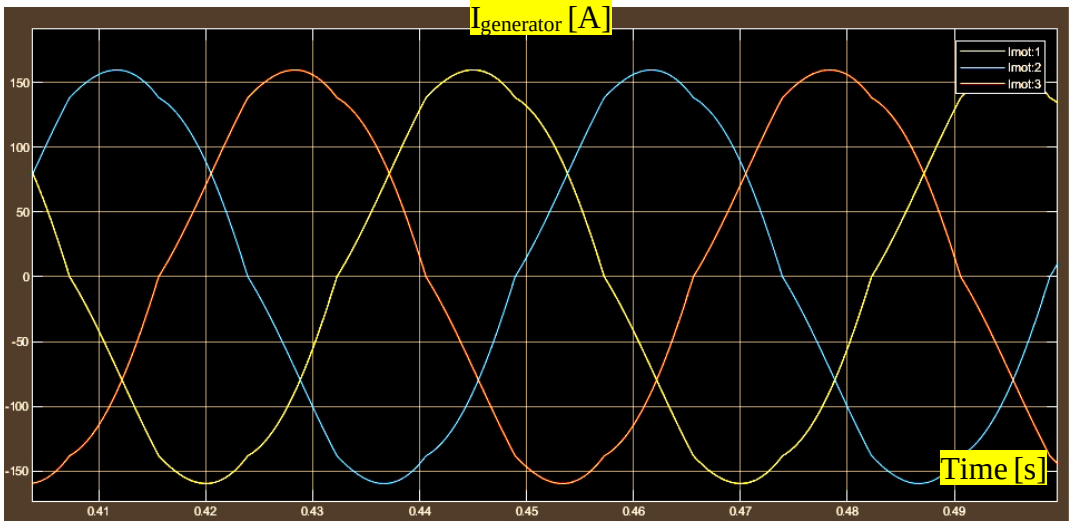

Figure 48: Generator's output current at 30 rpm

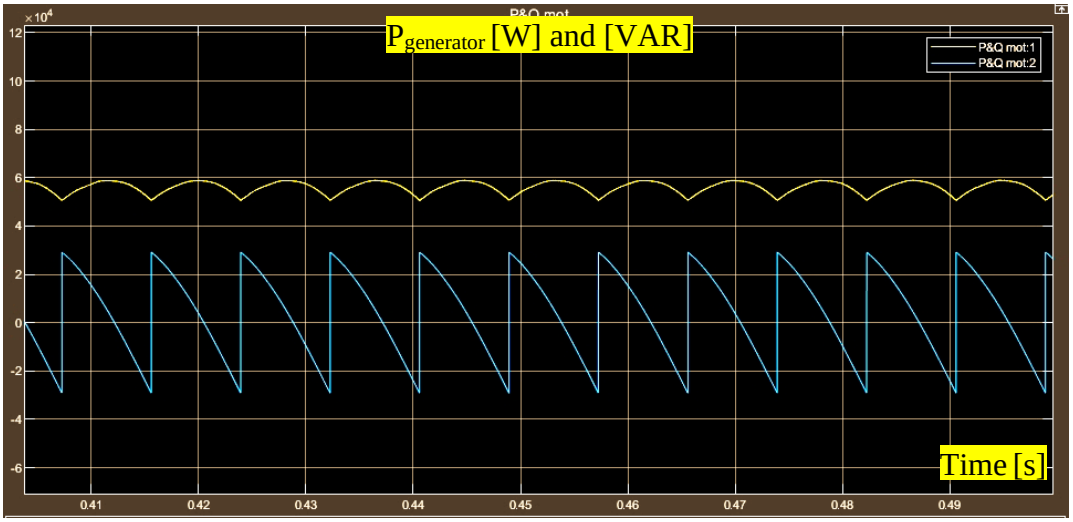

Figure 49: Generator's output power at 30 rpm

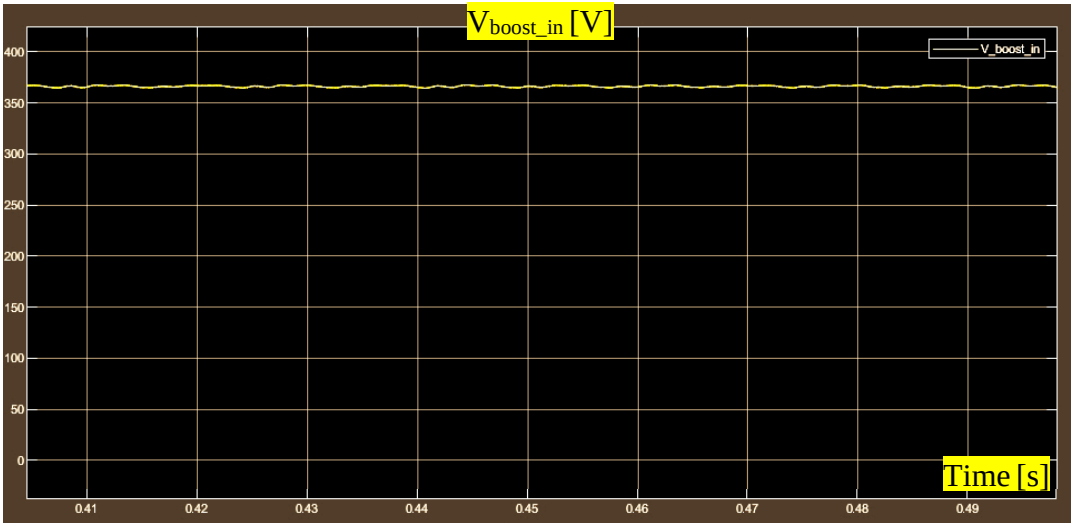

Figure 50: Boost converter's input voltage at 30 rpm

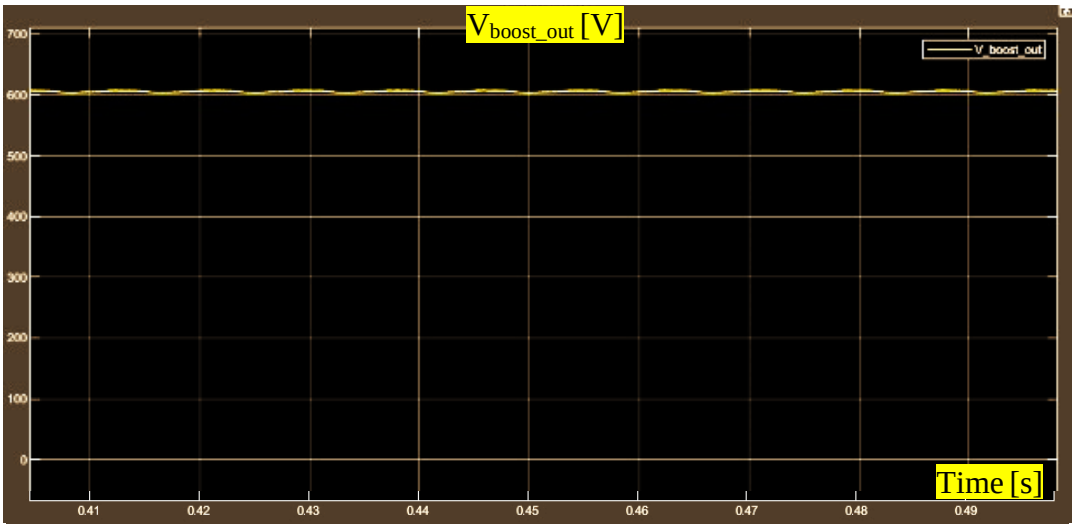

Figure 51: Boost converter's output voltage at 30 rpm

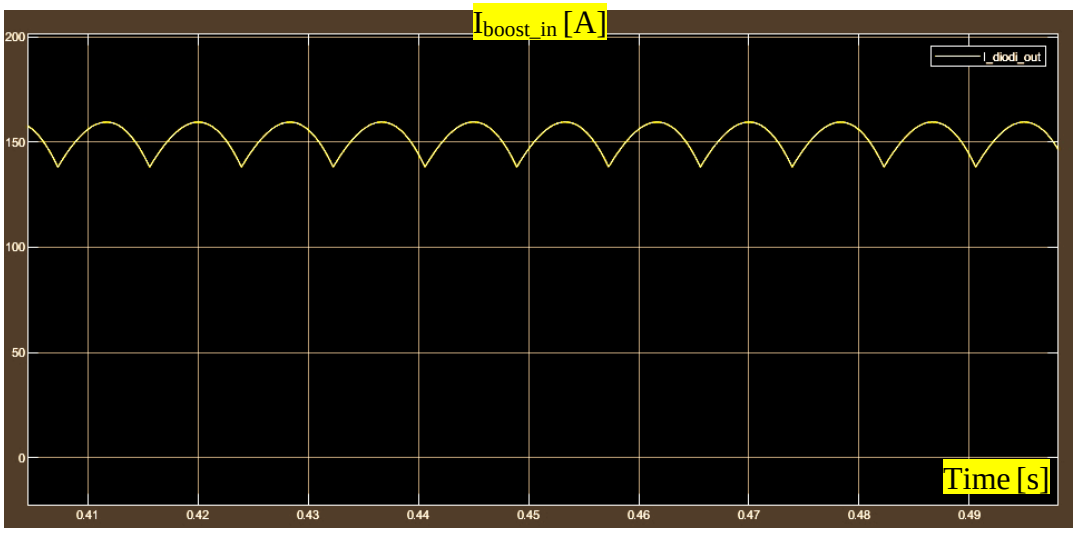

Figure 52: Boost converter's input current at 30 rpm

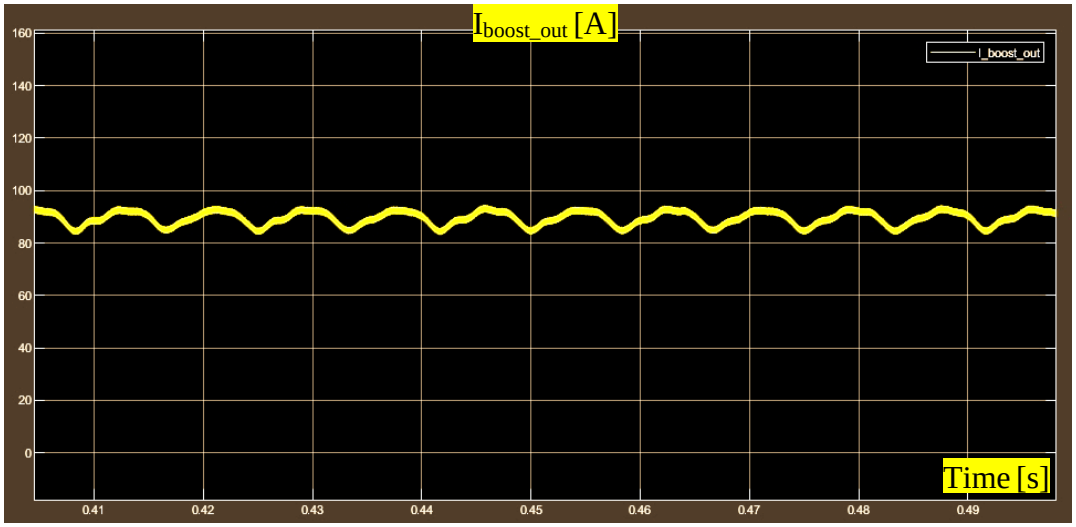

Figure 53: Boost converter's output current at 30 rpm

This study demonstrates the correct operation of the system with a boost converter featuring 4 diode bridges in parallel. The boost converter in this configuration requires a power switch (IGBT in this case) capable of withstanding a voltage greater than 600V and a current exceeding 300 A. The converter can be modified and adapted to higher IGBT switching frequencies beyond 10 kHz.

However, a challenge of this boost converter system is that it must operate with a maximum duty cycle of 80% to ensure an output voltage between 560 V and 600 V. Assuming a desired output voltage of 600 V, the minimum voltage at the boost converter input must not drop below 120 V, as indicated by the following equation.

$$\mathrm{V}_{in} = (1 - D) \ * \ \mathrm{V}_{out}$$

Equation 26

This implies that the minimum speed of the generator must be greater than 9 rpm. Unfortunately, this sets a speed limit that does not meet the project requirements, where the machine must operate down to 3 rpm.

Due to this limitation, further exploration of alternative power electronic systems for the generator control system is considered. The next section introduces the Buck-boost converter system, followed by a discussion of the dual inverter solution in the subsequent section.

In conclusion, the study delves into the intricate design and simulation of the diode bridges and boost converter system for controlling a screw turbine generator. The diode bridges serve the critical function of converting three-phase AC voltage from the generator into a pulsating DC voltage, setting the stage for subsequent power conversion.

The boost converter, a pivotal element in the system, undergoes meticulous modelling and simulation to ensure optimal performance across a range of generator speeds. The control system is designed to regulate the speed of the screw turbine, maintaining a desired head difference (ΔH) by adjusting the turbine speed. This, in turn, dictates the power generated, emphasizing the importance of an efficient and responsive control mechanism.

The complexity of the boost converter lies in its ability to absorb maximum power from the generator across varying speeds. Detailed calculations and considerations, as outlined in the Texas Instruments reference, facilitate the design of the boost converter components such as inductance and capacitance.

6.2 Diode Bridges and Buck-Boost Converter

As a second approach to generator control, the idea of utilizing four diode bridges, one for each machine circuit, has been conceived. However, in this case, the bridges are connected in series, allowing for a higher voltage output compared to the previous parallel configuration. Simulations conducted in Simulink reveal output voltages ranging from approximately 16 V at 3 rpm to around 2000 V at 30 rpm.

Since the generator needs to be connected to the grid through an inverter, a DC-DC converter must be added to ensure an input voltage to the inverter within the range of 560 V to 600 V for all generator speeds. Due to the elevated output voltage at high speeds, a voltage reduction system (Buck converter) is required, while at low speeds, a voltage-boosting system (Boost converter) is needed to meet the input voltage range of the inverter [23]. The schematic below illustrates this new control system.

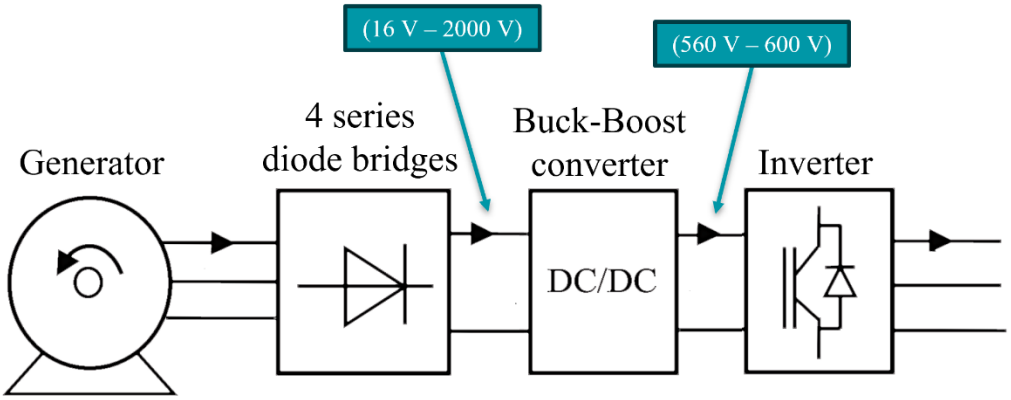

Figure 54: Generator control system with Buck-Boost converter.

Similar to the previous case, it is advisable to use the Buck-Boost converter with a maximum duty cycle of 80%. Therefore, based on the Buck-Boost equation below, it can be demonstrated that the minimum input voltage to the converter must exceed 150 V. Simulation results show this voltage at around 5 rpm generator speed, which is a lower speed compared to the previous boost converter scenario.

$$V_{in} = \left(\frac{1 - D}{D}\right) * V_{out}$$

Equation 27

The image below provides an example of a Buck-Boost converter, featuring a power switch (in this case, a Mosfet), an inductance, a diode, and a capacitor. With just

these four components, a system can be constructed to stabilize an output voltage in direct current, either lowering or raising the direct voltage at its input.

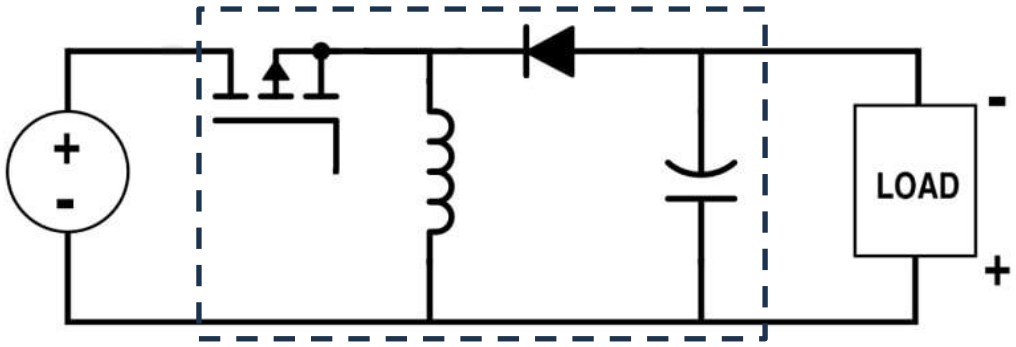

Figure 55: Buck-Boost converter diagram [24].

The challenge in employing the Buck-Boost converter lies in selecting the power switch. As evident from the previous figure, the switch is subjected to a much higher voltage than in the previous case, requiring assurance that the switch can withstand a voltage greater than its maximum input, which is 2000 V.

In conclusion, the exploration of a Buck-Boost converter as an alternative for controlling the generator presents a viable solution for managing the varying speeds of the machine. The series connection of four diode bridges allows for a broader range of output voltages, catering to the diverse speed requirements of the generator. The incorporation of a Buck-Boost converter facilitates the adjustment of voltage levels to meet the specifications of the grid-connected inverter.

Despite the advantages offered by the Buck-Boost converter, careful consideration must be given to the selection of the power switch. The increased voltage requirements impose challenges in ensuring that the switch can handle the elevated voltage levels, especially when compared to the earlier Boost converter configuration.

Through systematic simulations and analysis, the proposed Buck-Boost solution demonstrates its effectiveness in stabilizing the output voltage for various generator speeds. This alternative control strategy provides flexibility and adaptability, addressing the limitations encountered with the Boost converter at both high and low speeds. As the exploration of control strategies continues, further refinements and optimizations may be necessary. The Buck-Boost converter, with its ability to handle a broader range of input and output voltages, emerges as a promising candidate for efficiently regulating the generator's performance across different operating conditions.

6.3 Dual Inverters

In conclusion, the exploration of potential solutions for controlling the generator has led to the consideration of a more sophisticated and commercially viable approach. The third proposed solution involves the integration of a dual-inverter system, comprising one inverter on the machine side and another on the grid side. This system, while introducing complexity, offers several advantages, particularly in terms of precise power control and commercial availability. The machine-side inverter plays a pivotal role in this configuration, providing not only accurate control over the active power absorption but also managing the exchange of reactive power with the generator. Furthermore, it ensures a stable output voltage, effectively functioning as a Buck-Boost system. This inherent capability to modulate voltage levels facilitates the precise control of absorbed powers, contributing to the overall stability and efficiency of the system.

The bidirectional nature of the machine-side inverter is a noteworthy feature. It facilitates power exchange between the grid and the generator during startup, allowing for bidirectional power flow during energy production. The control system implemented in this inverter adds another layer of sophistication, enabling management of both active and reactive power generation. This capability holds the additional advantage of providing grid-phase modulation when required.

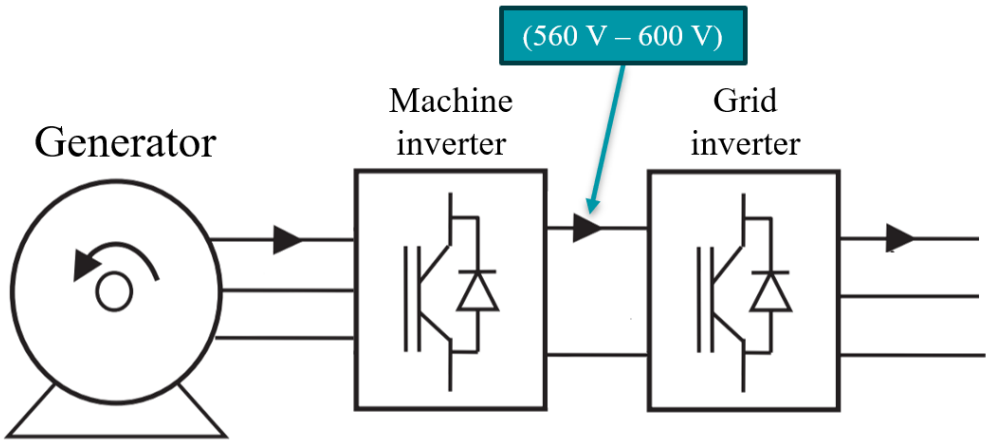

Figure 56: Generator control system with double inverters.

One significant benefit of this approach is the commercial availability of the inverters. Unlike custom solutions such as the Boost and Buck-Boost converters, the dual-inverter system consists of commercially certified products. These inverters are produced and supplied by reputable manufacturers in the power electronics industry, ensuring reliability and adherence to industry standards. However, it is essential to acknowledge that such commercial solutions come with a higher price tag compared to custom-built systems. The increased cost is a trade-off for the convenience and reliability offered by certified products. While the initial investment may be higher,

the advantages in terms of accessibility, reliability, and sophisticated control capabilities make this approach a compelling option for certain applications [25]. The next figure shows the complete diagram of a dual inverter system.

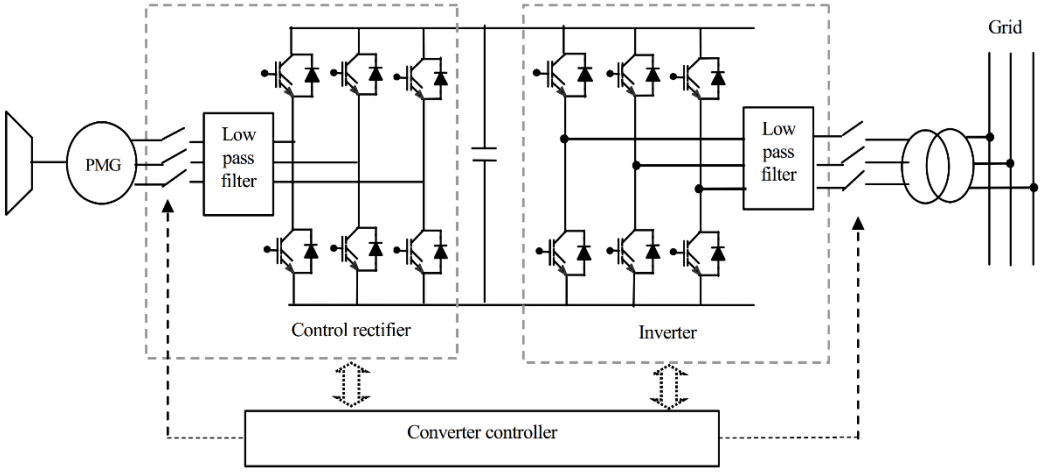

Figure 57: Dual inverter diagram [26].

In the upcoming chapter, a more in-depth exploration of the control aspects of this double-inverter system will be undertaken. This detailed analysis aims to elucidate the nuanced intricacies of managing power generation, reactive power exchange, and grid-phase modulation. By understanding and optimizing the control mechanisms, the system can be fine-tuned to achieve optimal performance, striking a balance between efficiency and cost-effectiveness.

6.4 Conclusion for the Control System

After presenting these three solutions to the company, the decision was made to proceed with the third option, the dual inverter system, primarily due to considerations of component availability. This choice underscores the importance of adopting solutions that are not only technically efficient but also practical and readily accessible in the market.

In the upcoming chapters, the focus will be on the third solution, with the goal of adapting the generator to ensure an optimized control system that seamlessly integrates with the dual inverter. This development and implementation phase will be crucial to fully leverage the advantages offered by the dual inverter, such as precise control of active and reactive powers, voltage output management, and operational flexibility during startup and power production. Specifically, the challenges and opportunities associated with implementing the dual inverter system

will be addressed in detail. This will include a thorough analysis of the control of this system, with particular attention to strategies for optimizing performance, maximizing efficiency, and ensuring operational stability in various operating scenarios.

While this approach may involve an initial learning curve due to the complexity of the solution, it promises to deliver a robust, reliable system that complies with industrial standards. The choice of a commercially available system represents a strategic long-term investment, considering ease of maintenance, spare parts availability, and the system's suitability for the company's needs.

In summary, the company made a decision based on thoughtful criteria, aiming for practicality and operational robustness offered by the third solution. The upcoming chapters will outline the path of implementation and refinement of the dual inverter system, contributing to the realization of an optimized and high-performing electrical generation plant.

7 Dual Inverter Control System

As mentioned in the previous chapter, the dual inverter solution offers several advantages, including precise control of machine torque, speed, and consequently, active power. Moreover, the dual inverter system provides the additional benefit of controlling the reactive power exchanged between the electric generator and the electrical grid, contributing to grid support and power factor correction. This latter advantage is far from trivial, as reactive power control enables the full utilization of the generator's power capacity.

As mentioned earlier, the complete system will feature four machine-side inverters, one for each three-phase circuit, with their outputs connected in parallel. Additionally, there will be a single grid-side inverter. This configuration has been carefully considered to ensure the generator's service continuity. Specifically, any fault occurring in one of the four machine circuits does not result in a complete shutdown of the machine. Instead, it may only exclude the affected circuit, providing uninterrupted operation of the overall system. The figure below illustrates the final system configuration.

This strategic arrangement enhances the reliability and fault tolerance of the generator system, addressing concerns related to potential circuit failures. The parallel connection of the machine-side inverters allows for a seamless transition between circuits, maintaining overall functionality even in the presence of localized faults.

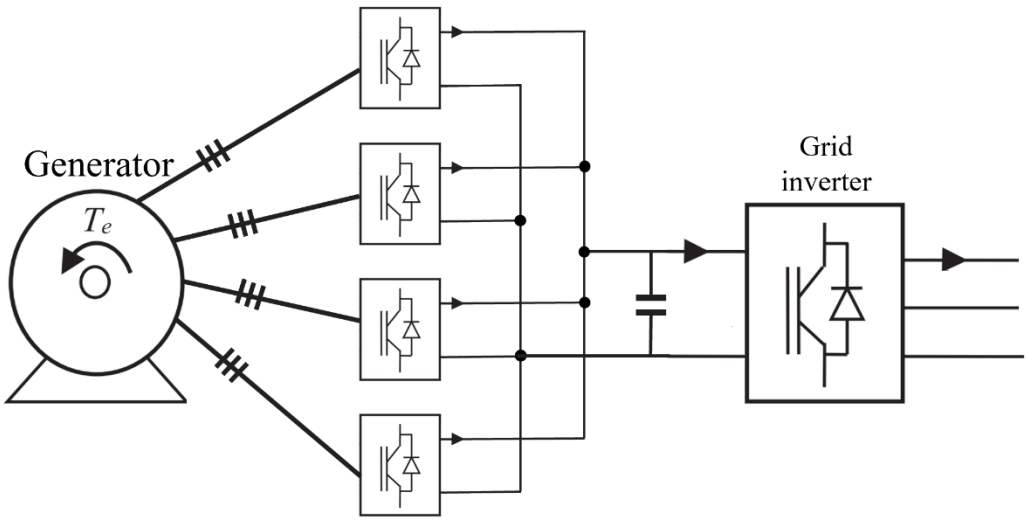

Figure 58: Extended dual inverter system.

In the previous chapter, we explored the system with the Boost converter, and simulations revealed the generation of reactive power due to the presence of diode bridges. This reactive power limited the generation of active power to be injected into the grid, primarily due to the generator's current limit constraints. However, with the dual inverter system, it becomes possible to optimize control to achieve zero reactive power generation, allowing the entire current to be utilized for generating active power. This advantage can be harnessed through the implementation of Field Oriented Control (FOC) techniques [27].

In this chapter, we will delve into the FOC technique in detail, understanding how it can be applied to maximize the potential of the electric generator. By adopting FOC, it becomes feasible to finely control the machine's magnetic field orientation and achieve optimal power generation, overcoming the limitations imposed by reactive power generation in traditional setups. This detailed exploration of FOC will encompass its principles, implementation strategies, and the impact it can have on the overall performance of the dual inverter system. Additionally, we will discuss how FOC contributes to achieving operational efficiency, minimizing losses, and ensuring a dynamic response to varying load conditions.

7.1 Field Oriented Control

Field Oriented Control (FOC), also known as Vector Control, stands as a groundbreaking variable-frequency drive (VFD) method designed to masterfully control three-phase electric motors and generators [28]. In this sophisticated approach, the stator currents of a three-phase AC electric motor are deconstructed into two orthogonal components, forming a vector. One component characterizes the motor's magnetic flux, while the other defines its torque. The control system orchestrates the calculation of corresponding current component references based on flux and torque references provided by the drive's speed control.

FOC leverages proportional-integral (PI) controllers to maintain measured current components at their designated reference values. The pulse-width modulation of the variable-frequency drive dictates transistor, MOSFET or IGBT switching according to the stator voltage references, outputting from the PI current controllers.

7.1.1 Applications and Evolution

FOC is used to control AC synchronous and induction motors and generators. It was originally developed for high-performance motor applications that are required to operate smoothly over the full speed range, generate full torque at zero speed, and have high dynamic performance including fast acceleration and deceleration. However, it is becoming increasingly attractive for lower performance applications as well due to FOC's motor size, cost and reduced power consumption reduction. It is expected that with increasing computational power of the microprocessors it will eventually almost universally replace single-variable scalar control (so-called V/f control).

In vector control, an AC induction or synchronous motor is controlled under all operating conditions like a separately excited DC motor. That is, the AC motor behaves like a DC motor in which the field flux linkage and armature flux linkage created by the respective field and armature (or torque component) currents are orthogonally controlled so that, when torque is changed, the field flux linkage is not affected, hence enabling dynamic torque response.

7.1.2 Coordinate Transformations

Vector control accordingly generates a three-phase PWM motor voltage output derived from a complex voltage vector to control a complex current vector derived from motor's three-phase stator current input through projections or rotations back and forth between the three-phase speed and time dependent system and these vectors' rotating reference-frame two-coordinate time invariant system.

Such complex stator current space vector can be defined in a (d,q) coordinate system with orthogonal components along d (direct) and q (quadrature) axes such that field flux linkage component of current is aligned along the d axis and torque component of current is aligned along the q axis. The motor's (d,q) coordinate system can be superimposed to the motor's instantaneous (a,b,c) three-phase sinusoidal system as shown in Figure 59. The symbol θ_{er} represents the angle between the (a,b,c) and (d,q) coordinate systems, and the ω_{er} represents the (d,q) reference system speed. Components of the (d,q) current vector allow for conventional control such as proportional and integral, or PI, control, as with a DC motor.

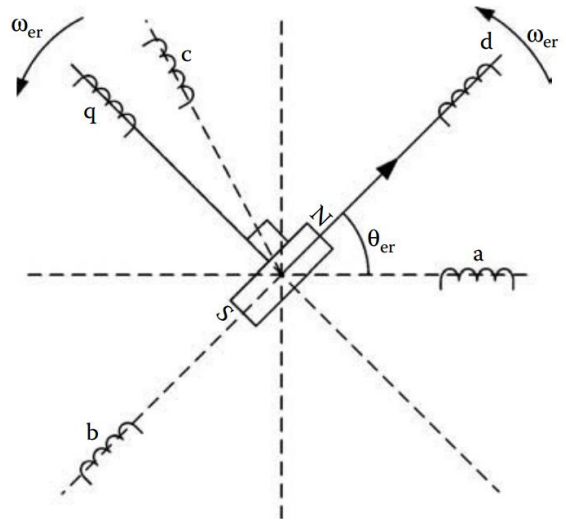

Figure 59: Coordinate transformation from (a,b,c) representation to (d,q) representation [29].

Projections associated with the (d,q) coordinate system typically involve:

1. Forward projection from instantaneous currents to (a,b,c) complex stator current space vector representation of the three-phase sinusoidal system.
2. Forward three-to-two phase, (a,b,c) to (α,β) projection using the Clarke transformation. Vector control implementations usually assume ungrounded motor with balanced three-phase currents such that only two motor current phases need to be sensed. Also, backward two-to-three phase, (α,β) to (a,b,c) projection uses space vector PWM modulator or inverse Clarke transformation and one of the other PWM modulators.
3. Forward and backward two-to-two phase, (α,β) to (d,q) and (d,q) to (α,β) projections using the Park and inverse Park transformations, respectively.

The idea of using the Park transform is to convert the system of three phase currents and voltages into a two-coordinate linear time-invariant (LTI) system. By making the system LTI is what enables the use of simple and easy to implement PI controllers, and also simplifies the control of flux and torque producing currents.

While (d,q) coordinate system rotation can arbitrarily be set to any speed, there are three preferred speeds or reference frames:

1. Stationary reference frame where (d,q) coordinate system does not rotate.
2. Synchronously rotating reference frame where (d,q) coordinate system rotates at synchronous speed.
3. Rotor reference frame where (d,q) coordinate system rotates at rotor speed.

Decoupled torque and field currents can thus be derived from raw stator current inputs for control algorithm development.

7.1.3 **Measurement and Transformation Process**

Whereas magnetic field and torque components in DC motors can be operated in a relatively simple way by separately controlling the respective field and armature currents, economical control of AC motors in variable speed application has required development of microprocessor-based controls with all AC drives now using powerful DSP (digital signal processing) technology.

The next figure explains the FOC method in a very detailed way. With the measurements of the 3 currents (i_a, i_b and i_c) and the rotor angle θ, it is possible to use the Clarke and Park transformations to transform the (a,b,c) projections to the (d,q) projections. The is_d and is_q can be compared with the referenced current values, which yields the current error, to control the electric machine torque and flux. The current controllers transform the current error to a (d,q) projections voltages. Finally, with the use of the inverse Park and Clarke transformations it is possible to control the electric machine voltage [30] [31].

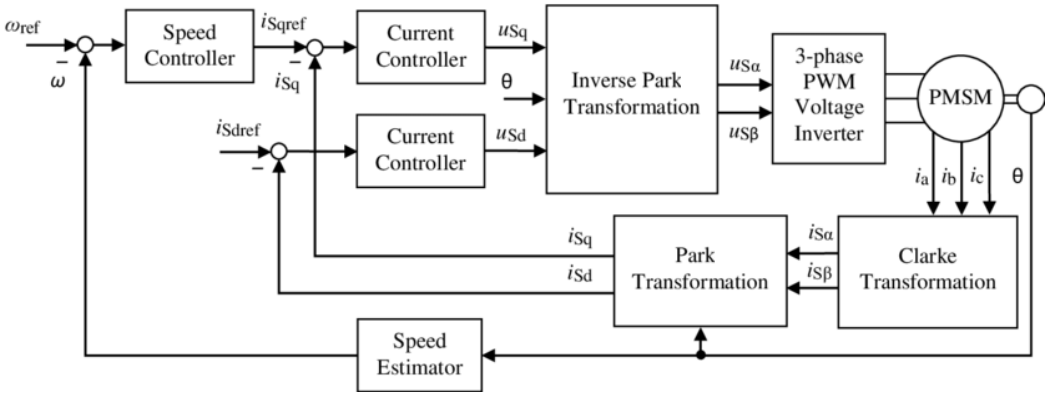

Figure 60: Field Oriented Control block diagram [32].

7.2 Generator design for Dual Inverter Control

As explained earlier, the dual inverter system offers numerous advantages over static DC-DC converters such as Boost and Buck-Boost. However, the generator designed so far has been tailored for Boost converter systems. Consequently, adaptation was necessary to integrate it with the new dual inverter system.

Commercial machine-side inverters typically require a rms line-to-line voltage below 600 V. This led to the redesign of the generator winding, adjusting the number of turns per coil (NSB) to achieve a nominal line-to-line voltage (at 30 rpm) of approximately 500V. This constraint resulted in an NSB of 18 turns per coil.

To further reduce the machine inductance values, the slot opening was maximized. This approach aimed to maximize the flux passing through the air gap. The figure below illustrates the magnetic flux distribution in the machine with surface magnets before the redesign (left) and after the redesign (right).

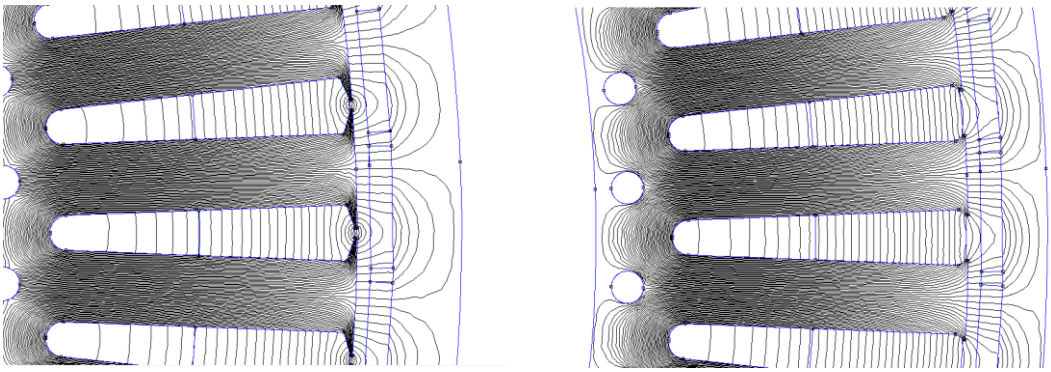

Figure 61: Shape of machine magnetic flux with magnets off before the redesign (left figure) and after the redesign (right figure).

This redesign not only ensures compatibility with the voltage requirements of commercial machine-side inverters but also optimizes the machine's magnetic characteristics for enhanced performance within the dual inverter system. The adjustments in winding configuration and slot geometry align the generator with the operational parameters of the dual inverter, paving the way for seamless integration and improved overall system efficiency.

The following sections will delve into the detailed engineering aspects of this generator redesign, exploring how these modifications impact on its electrical and magnetic characteristics. Additionally, the performance of the adapted generator within the dual inverter system will be assessed through simulations and analysis, providing valuable insights into its behavior under various operating conditions.

7.2.1 **Analytical Verification**

After redesigning the generator to meet the desired output voltage, two verifications were conducted to ensure the correctness of the coil turns calculation. The first verification follows the field-oriented control system, as explained in Ion Boldea's book "Electric Generators Handbook" [29]. Boldea employs direct axis (I_d) and quadrature axis (I_q) currents to determine the machine current (I_s) through the Equation 28:

$$I_s = \frac{\sqrt{{I_d}^2 + {I_q}^2}}{\sqrt{2}}$$

Equation 28

For the verifications, the generator is set to work at its maximum torque angle, with I_d set to zero and I_q set to the nominal current for each machine circuit, where:

$$I_q = -\sqrt{2} * \frac{I_n}{NCP}$$

Equation 29

as the machine operates as a generator. Certainly, in the previous equation, a negative value for I_q is chosen because the electric machine is being used as a generator rather than a motor.

The electrical angular frequency ω is calculated based on the generator's mechanical rotational speed Ωr in rpm and the pole pairs P, as follows:

$$\omega = 2\pi * P * \frac{\Omega r}{60}$$

Equation 30

The maximum no-load magnetic flux λ_{mag_max} is obtained from the FEMM simulation of the no-load magnetic flux. This flux enables the calculation of the generator's no-load voltage using Equation 31:

$$E_0 = \omega * \frac{\lambda_{mag\_max}}{\sqrt{2}}$$

Equation 31

Knowing the resistance R and the inductances L_d and L_q of each machine circuit, the direct axis voltage V_d and quadrature axis voltage V_q can be calculated, along with the rms output voltage V_{out}, as shown in the following equations:

$$V_d = R * I_d - \omega * L_q * I_q$$

Equation 32

$$V_q = R * I_q + \omega * (L_d * I_d + \lambda_{mag\_max})$$

Equation 33

$$V_{out} = \sqrt{3} * \frac{\sqrt{V_d^2 + V_q^2}}{\sqrt{2}}$$

Equation 34

Finally, the generated active power P_{out} of the generator at that speed can be calculated using Equation 35:

$$P_{out} = NCP * \frac{3}{2} * |(V_d * I_d + V_q * I_q)|$$

Equation 35

These calculations allow for the verification of the generated voltage and active power for various speeds, as detailed in the following table.

Ωr [rpm]	V_{out} [V]	P_{out} [kW]
3,3	46	4,86
8	125	35,34
15	246	80,76
25	420	145,628
30,3	513	180,012
33	560	197,528

Table 2: Output voltage and active power for various generator speeds by the analytical method.

In conclusion, the analytical verification process, based on the field-oriented control methodology outlined in Ion Boldea's "Electric Generators Handbook," has been instrumental in ensuring the correctness of the coil turns calculation for the redesigned generator. By imposing specific direct-axis (I_d) and quadrature-axis (I_q) currents at the maximum torque angle, the analytical approach facilitated the determination of the machine current (I_s). Subsequently, the analysis involved the calculation of the electrical frequency, obtaining the maximum flux linkage without

load, and determining the open-circuit voltage. Leveraging the known resistance and inductances of each machine circuit, the verification extended to deriving the direct and quadrature-axis voltages, ultimately leading to the calculation of the rms line-to-line output voltage (V_{out}) and the corresponding active power generated. This comprehensive analytical verification process provides confidence in the accuracy of the coil turns selection, affirming its suitability for the requirements of the redesigned generator under varying speeds.

7.2.2 FEMM Verification

The second verification involved Finite Element Method (FEMM) simulations, specifically focusing on torque ripple with nominal machine current while setting the torque angle to its maximum value, effectively aligning with the maximum torque angle. As mentioned earlier, configuring the system for the maximum torque angle is equivalent to setting the direct-axis current to zero.

Through the torque simulation results, the flux linkage with the loaded winding was determined as follows:

$$\lambda_{tot} = \frac{2}{3} * \left(\lambda_A e^{-0i} + \lambda_B e^{\frac{-2}{3}\pi i} + \lambda_C e^{\frac{-4}{3}\pi i} \right)$$

Equation 36

Once the flux linkage with the loaded winding at nominal load was computed, the voltage induced across the generator terminals was determined using Equation 37:

$$\mathrm{V}_{out} = \sqrt{3} \ * \ \frac{\omega \ * \ \lambda_{tot}}{\sqrt{2}}$$

Equation 37

Finally, knowing the nominal machine torque T_n, it was possible to calculate the active power generated by the machine:

$$\mathrm{P}_{out} = NCP \ * \left(\frac{T_n \ * \ \omega}{P \ * \ NCP} - \ 3 * R * {I_s}^2 \right)$$

Equation 38

And finally, the values of line-to-line voltage and active power for various speeds were determined through this second verification method. The table below presents results that closely align with those obtained through the previous analytical

approach. This consistency serves as evidence supporting the accuracy of the coil redesign performed during the generator winding reengineering phase.

Ωr [rpm]	V_{out} [V]	P_{out} [kW]
3,3	55	4,23
8	133	33,83
15	249	77,9
25	415	140,9
30,3	503	174,3
33	548	191,3

Table 3: Output voltage and active power for various generator speeds by the FEMM method.

In conclusion, the verification of the generator winding redesign involved two distinct methods: an analytical approach based on field-oriented control principles, as outlined in Ion Boldea's Electric Generators Handbook, and a simulation-based method using FEMM for ripple torque simulations. Both methods were employed to ensure the accuracy and reliability of the redesigned coil configuration.

The analytical approach, incorporating key parameters such as direct-axis current (I_d), quadrature-axis current (I_q), and mechanical speed (Ωr), provided a theoretical foundation for calculating line-to-line voltage and active power. The results obtained through this method were then cross-validated using FEMM simulations, specifically focusing on torque ripple under nominal machine current conditions.

The FEMM simulations confirmed the effectiveness of the redesigned coil configuration, as the results closely aligned with the analytical findings. This dual-method verification instils confidence in the accuracy of the generator winding redesign, ensuring that the generator will operate efficiently and reliably across a range of speeds. This meticulous verification process is crucial for the successful integration of the generator into the dual inverter system, guaranteeing optimal performance in real-world applications.

8 Generator Estimated Cost

One of the crucial steps in the industrialization of the studied generator is its cost analysis. In this chapter, a detailed cost estimation of the generator is undertaken, with the assistance of Dr. Matteo De Martin, an expert in electrical design for screw turbines. This cost estimate, conducted in April 2023, reflects the prices in the Italian market during this period. It is important to emphasize that this study played a pivotal role in determining the commercial viability of this generator compared to traditional solutions.

To streamline the cost estimation, it is divided into six main parts:

1. Cost of Stator and Rotor laminations:
   - This includes the expenses associated with the laminations for both the stator and rotor.

2. Cost of Copper for Stator Windings and Winding Production:
   - Encompasses the cost of copper needed for the stator windings and the overall winding production.

3. Cost of Magnets and Magnet Gluing:
   - Covers the expenses related to acquiring magnets and the cost associated with their gluing process.

4. Cost of Stator Internal Casing and Integration with Laminations:
   - Includes the costs involved in manufacturing the internal casing of the stator and integrating it with the stator laminations.

5. Cost of Cooling System Implementation:
   - Encompasses the expenses associated with the implementation of the cooling system.

6. Cost of Insulating Material and Generator Cables:
   - Involves the cost of acquiring insulating materials and the necessary cables for the generator.

By considering these six elements, it will be possible to estimate the overall cost of the generator, excluding the expenses related to the mechanical coupling between the generator and the screw turbine.

8.1 Cost of Stator and Rotor Laminations

As seen in previous chapters, the studied generator is an outer rotor generator primarily composed of permanent magnets, a rotor yoke, stator windings, and the internal stator. The figure below simplifies the representation of the main components of the studied generator.

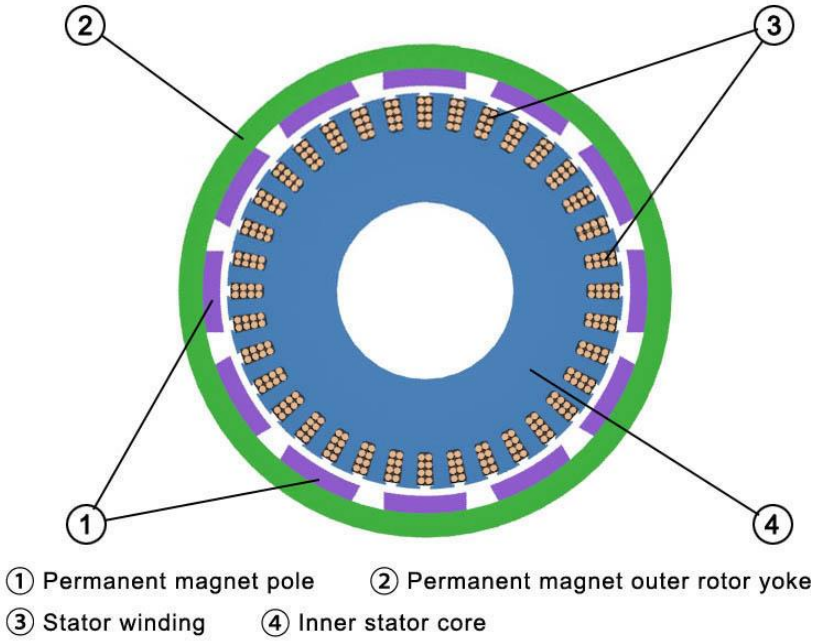

Figure 62:Outer rotor SPM machine [6].

From this illustration, it is evident that the main materials for constructing a generator include magnets, copper for windings, and iron for both the rotor and stator.

In theory, the stator must be laminated to reduce iron losses, while the rotor can be made of solid iron. In our case, for simplicity, it is assumed that both the stator and rotor are constructed from laminated iron, specifically using M800-100A iron. Here, M800 signifies that this material dissipates 8 W per kilogram when used at 1.5 tesla, and 100A indicates that the thickness of this iron lamina is equivalent to 1 mm.

From the FEMM model of the generator, it was possible to determine the overall area of both the stator and rotor. Additionally, knowing the machine's length enabled the calculation of the number of laminations to order. In this case, Engineer De Martin estimated an order of 930 laminations. The cost of a processed and cut lamination is approximately €8.38. This results in a total cost of laminations of about €7793.4.

8.2 Cost of Copper and Winding Production

The second part of the cost of the generator goes to the stator winding. This winding is made of copper wires wound around the stator teeth. The figure below shows how the winding is mounted around the stator teeth to build the inner part of the generator.

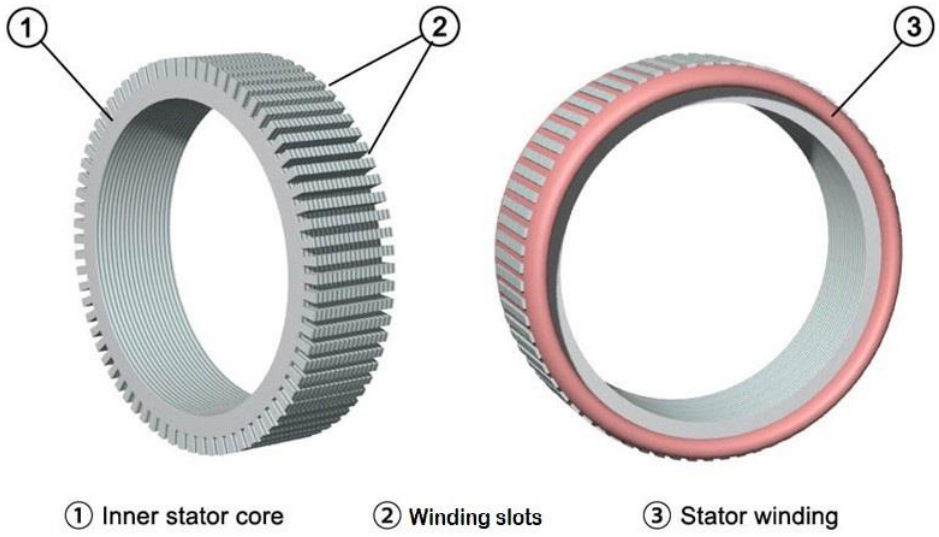

Figure 63: Outer rotor SPM machine stator winding [6].

To estimate the cost of the generator's copper winding, it is necessary to know the characteristics of the winding very well. In particular, it is necessary to know the length of the winding for each phase and the section of the winding. These characteristics were presented in previous chapters in order to calculate the phase resistance.

Therefore, knowing the length and section of the winding for each phase, and also knowing that the machine is made up of 3 phases per circuit, for a total of 4 circuits in parallel. This information allows us to easily calculate the volume of copper to be used for the winding. Knowing the specific weight of copper, it was possible to find the total weight of copper required for the machine equal to 520.65 kg. The price of copper on the market at that time was 10.2 €/kg, so the total cost of the copper is €5311.

Knowing the price of copper is not enough for the realization of the winding, this simply because the copper must be wound and inserted into the slots of the stator by a manual operation performed by experienced operators. The hourly rate of these operators is around 35 €/hour, and for this winding it is estimated at around 250 hours of work. This leads to a total of €8750.

After completion of the winding, the stator must go through a process of impregnation, drying and curing to ensure a certain robustness and insulation of the winding. This operation has an average cost of around €1500.

Therefore, by adding up all the costs shown for the winding so far, it will be possible to estimate a total of €15561 to be able to manufacture the winding of the generator.

8.3 Cost of Magnets and Magnet Gluing

A considerable amount of a permanent magnet generator cost is due to the magnets themselves. The construction process of permanent magnets is a complex and expensive process, and it has a significant impact on the final cost of the magnets.

In the case of the generator studied, it was decided to use NdFeB magnets. This type of magnet was chosen for its high-performance characteristics. In particular, this type of magnet presents:

- High magnetic force:
  - NdFeB magnets have a very high magnetic force, making them the most powerful permanent magnets currently available.

- High magnetic energy:
  - They have a high energy product, which is a measure of the amount of magnetic energy stored in a magnet. This feature contributes to their power and makes NdFeB magnets suitable for a wide range of applications.

- Wide range of operating temperatures:
  - They can operate effectively in a wide range of temperatures, although temperature can affect their magnetic performance.

- Resistance to corrosion:
  - NdFeB magnets are susceptible to corrosion, especially in humid environments. However, they can be treated with coatings or made with more resistant alloys to reduce this risk.

- High coercivity levels:
  - They have a very high magnetic coercivity, which is the ability of a magnet to resist demagnetization. This feature makes them stable and

suitable for applications where it is necessary to maintain a constant magnetic force over time.

- Light weight and compactness:
  - Compared to other types of magnets, NdFeB magnets are lightweight and can be made in very compact dimensions, while providing significant magnetic forces.

These types of magnets are tailored for electric machine manufacturers. Therefore, as it has been seen previously, the magnets chosen for the generator must be 42.2 mm wide and 8 mm high. These magnets are placed in series along the generator, along the whole generator's 710 mm length.

For transportation and assembly reasons, as well as to reduce eddy current losses, it is recommended to build the magnets with a maximum length of around 35 mm. Therefore, in order to have an integer number, it was decided to choose 35.5 mm long magnet segments. This means that each pole should have 20 magnets. Knowing that the generator is 80 poles, it was possible to calculate a total of 1600 magnets sized 42.2 × 35.5 × 8 mm. This type of magnet is sold at a piece price with a cost of around 9 €/piece. Therefore, the total cost of the magnets is €14,400.

Once the magnets are bought, they must be glued to the rotor, so a part of the cost of the generator derives from the price of the glue to be used for the magnets. In this case, a glue cost of around €600 is estimated.

Once the magnets and glue are found, it will be enough to assign the work to an experienced operator for gluing the magnets to the rotor. For this generator, it is estimated that about 133.3 hours of work are required for the gluing of all the magnets. As it has been seen, an hour of work of an experienced operator costs around €35, leading to a total cost of €4,667.

Finally, it is possible to sum up all these figures together to find a final cost of the magnets and their gluing of around €19,667.

In conclusion it is possible to see that the cost of the magnets is a major component in the overall cost of a permanent magnet generator. By choosing the right type of magnet and using efficient gluing methods, it is possible to minimize the cost of the magnets and keep the overall cost of the generator down.

8.4 Cost of Stator Internal Casing and Integration with Laminations

The internal fixing part of the stator is one of the most important parts of an external rotor generator. This part provides the mechanical support for the stator and ensures a smooth rotation of the rotor.

As the generator rotates, a mechanical torque is generated between the stator and the rotor. If the stator is not securely fixed in place, it can damage the entire machine. Therefore, it is important to carefully design the internal fixing part of the stator and its connection to the stator laminations.

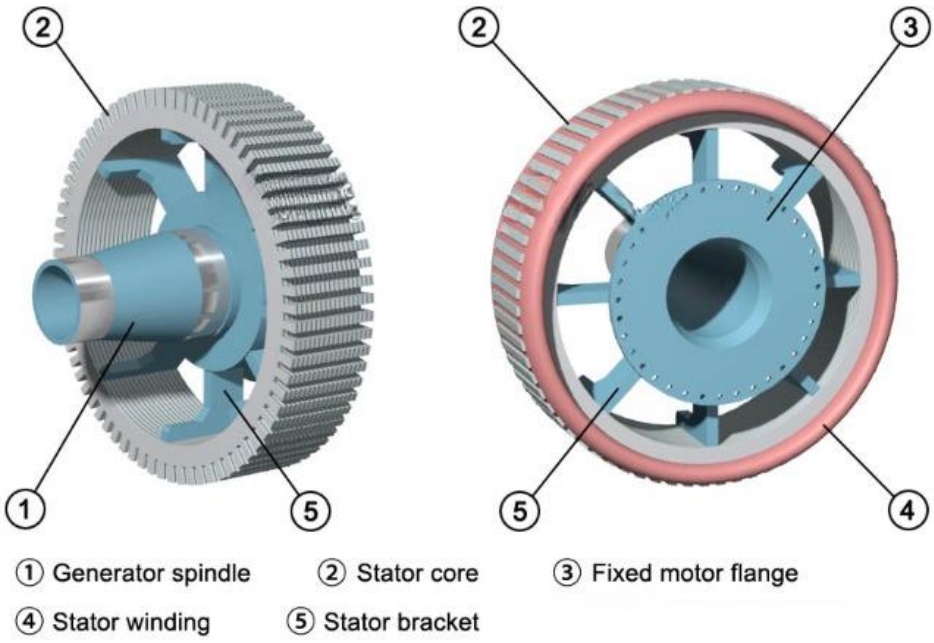

Figure 64: Outer rotor SPM machine internal fixing [6].

In the case of the generator studied, the internal fixing part consists of the following components:

- Generator spindle: This part houses the bearings that support the rotor.
- Stator core: This part provides the structural support for the stator laminations.
- Stator bracket: This part secures the stator laminations to the generator spindle.
- Fixed motor flange: This part guarantees the stator to be mechanically fixed.

Once the rotor and stator are complete, they can be assembled to form the generator. This process involves the following steps:

1. Mounting the rotor on the shaft: The rotor is mounted on the shaft using bearings. The bearings provide support for the rotor and allow it to rotate smoothly.
2. Inserting the stator into the housing: The stator is inserted into the housing, which provides a mechanical support for the stator.
3. Connecting the stator winding to the external circuit: The stator winding is connected to the external circuit using terminal cables. This allows the electrical power generated by the generator to be delivered to the load.

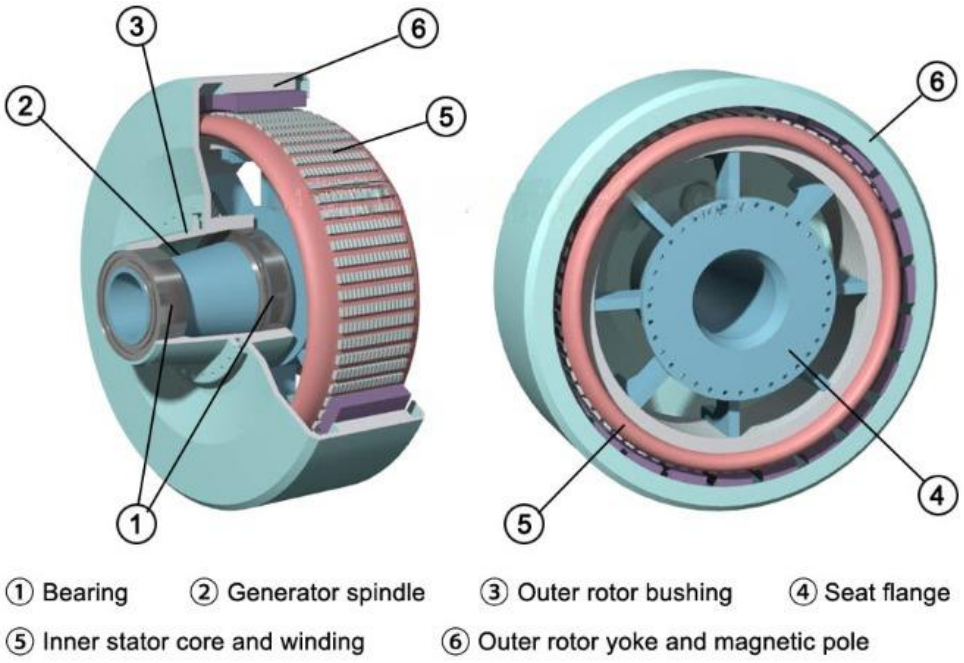

Figure 65: Outer rotor SPM machine assembling [6].

This figure shows a complete drawing of an external rotor SPM generator, where the generator has the following components:

- Rotor: The rotor consists of a stack of permanent magnets. The magnets are arranged in a circular pattern to create a rotating magnetic field.
- Stator: The stator consists of a stack of laminated steel sheets. The sheets are wound with copper wire to create the stator winding.
- Bearing housing: The bearing housing houses the bearings that support the rotor.
- Generator flange: This part provides the structural support for the stator.
- Terminals: The terminals connect the stator winding to the external circuit.

The assembly of an external rotor SPM generator is a relatively straightforward process. By following the steps outlined above, it is possible to assemble a reliable and efficient generator.

The cost of constructing the internal fixing part of the stator, the integration with laminations and the generator assembling process is estimated to be around €17,411. This estimate is based on the feedback from qualified mechanical designers with extensive experience in the field of turbines.

8.5 Cost of Cooling System Implementation

All electric machines, including external rotor SPM generators, are inefficient to some degree, meaning that they convert a portion of the mechanical energy they receive into heat. This heat must be dissipated effectively to maintain the generator's temperature within safe margins and prevent overheating.

In the case of the external rotor SPM generator studied, a simple open-loop cooling system is employed. Water is drawn from a nearby river and circulated through a network of copper tubes embedded within the generator's stator structure. As the water passes through the tubes, it absorbs the heat generated by the generator's operation. The heated water is then discharged back into the river, where it can discharge its heat to the environment.

Therefore, the cooling circuit has a single inlet for the cooling liquid and a single outlet. The figure below shows a portion of the cooling circuit from one side of the generator.

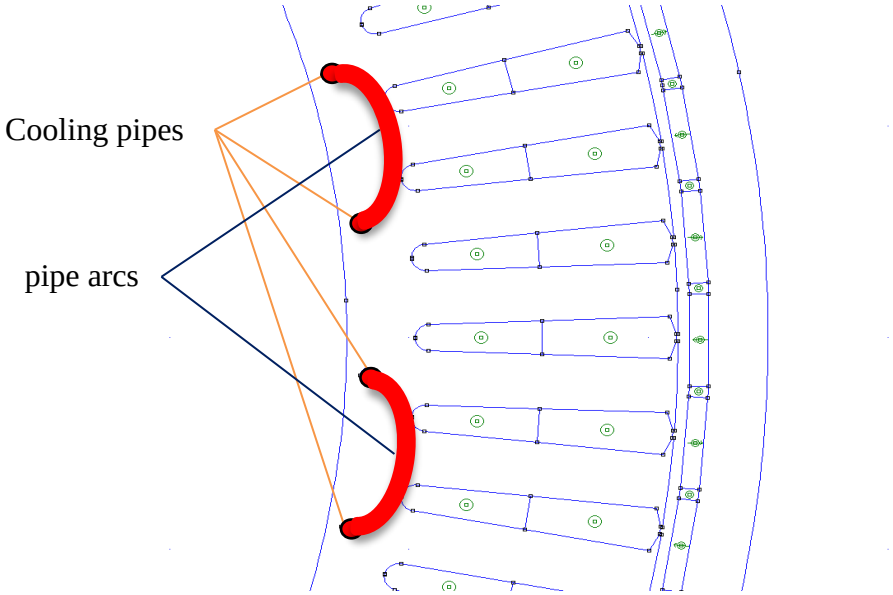

Figure 66: Cross section of the synchronous generator with the cooling system.

The tubes used for this circuit are 12 mm diameter copper tubes, with an estimated total length of approximately 65 m. Based on current market prices, a cost of €800 has been estimated for the copper tubes.

These copper tubes must be manually inserted into the generator by specialized operators and pressurized to ensure hydraulic tightness. For this type of work, 80 hours of work have been planned with an estimated cost of €35/hour, leading to a total labour cost of €2800.

The total cost of the cooling system, excluding the pump and water filters, is estimated to be around €3600. The pump is responsible for circulating the water through the tubes, while the water filters remove impurities and contaminants from the water to prevent clogging and maintain the system's temperature and efficiency.

Finally, it is important to remember that the cooling system plays a crucial role in maintaining the efficiency and lifespan of an external rotor SPM generator. By carefully designing and implementing a suitable cooling system, the generator can operate effectively and reliably for extended periods (decades).

8.6 Cost of Insulating Material and Generator Cables

The final cost of this generator stems from the generator's insulating materials, which serve to ensure a certain electrical safety, such as:

- **Impregnated paper**: This is the most commonly used insulating material in low-voltage generators. It is an economical and easy-to-work material, and has good electrical and mechanical insulation properties. Impregnated paper is used to insulate electrical conductors from each other and from the metal components of the generator.
- **Epoxy resin**: This is a synthetic material that is used to coat electrical conductors and metal components of the generator. Epoxy resin has good electrical and mechanical insulation properties, and is resistant to high temperatures.
- **Silicone**: This is a synthetic material that is used to insulate electrical conductors and metal components of the generator in humid or corrosive environments. Silicone has good electrical and mechanical insulation properties, and is resistant to water and chemicals.

These insulating materials are used in an electric generator at the following points:

- **Between electrical conductors**, to prevent them from touching each other and causing a short circuit.
- **Between electrical conductors and metal components of the generator**, to prevent them from touching each other and causing a short circuit or an electrical discharge.
- **To coat metal components of the generator**, to protect them from corrosion and wear.

The choice of insulating materials to use in a low-voltage electric generator depends on a number of factors, including the operating voltage of the generator, the environmental conditions in which the generator must operate, and the cost of the materials.

In addition to the insulating materials, there is a small amount of costs pertaining to the generator's cables. The total cost of the insulating materials and machine cables is estimated to be around €797.

In conclusion, it is important to note that the insulating materials used in an electric generator are essential for ensuring its safe operation. By choosing the right materials and applying them correctly, manufacturers can help to protect users from electrical hazards.

8.7 Total Generator Estimated Cost

After this long cost analysis, it is possible to predict a total cost of the generator of around €65,000. This price does not include the mechanical coupling system between the generator and the turbine.

In traditional systems, with induction machine, in addition to the cost of the generator, the cost of the gearbox is also added, but in our case the gearbox does not exist because the generator has a rotational speed equal to that of the screw.

Even if the traditional screw turbine, generator and gearbox system is simplified with the new design of the integrated generator with external rotor, the total price of the entire system is still greatly increased compared to the traditional system. This is basically due to the high price of permanent magnets. The traditional system uses an induction generator which has very low costs compared to a synchronous permanent magnet generator.

After an in-depth economic analysis conducted jointly with the company, it was noted that the new generator together with its mechanical coupling system with the screw turbine has a price about twice that of the traditional generator with its gearbox. For this reason, the company has decided not to prototype this innovative solution and perhaps leave it for future developments to be carried out with financial support from research grants.

In conclusion of this analysis, it is clear that the new generator design is not currently economically viable. The high cost of permanent magnets is a major factor accounting for this, as it more than doubles the cost of the generator compared to the traditional system. The company has therefore decided to focus on other developments for the time being. However, the new generator design has the potential to be a significant improvement over traditional system. It is more efficient, has a longer lifespan, and is less likely to require maintenance thanks to its bearing-less direct-coupling layout. If the cost of permanent magnets could be reduced, the new design would become a viable and attractive option for a range of applications.

9 Eddy Current Losses in SPM Machines

Eddy currents are circular electric currents that are induced in conductors by a changing magnetic field. They are named after the French physicist Léon Foucault, who discovered them in 1855.

To understand how eddy currents work, let us consider a conductor placed in a changing magnetic field. As the magnetic field changes, it induces an EMF (electromotive force) in the conductor. This EMF causes electrons in the conductor to flow, creating an electric current. The current flows in closed loops, perpendicular to the magnetic field. This phenomena can be illustrated in the figure below.

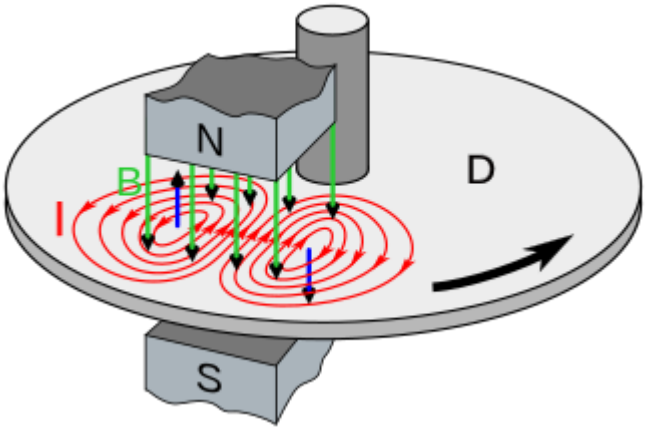

Figure 67: Eddy currents (I) induced in a conductive metal plate (D) as it moves to the right under a magnet (N-S) [33].

When eddy currents flow through a conductor, they generate heat. This is because the electrons in the conductor collide with the atoms of the conductor, and this collision releases energy in the form of heat.

The magnitude of the eddy current is determined by several factors:

- **The strength of the magnetic field**: The stronger the magnetic field, the stronger the eddy current.
- **The area of the conductor**: The larger the area of the conductor, the stronger the eddy current.
- **The rate of change of the magnetic field**: The faster the magnetic field changes, the stronger the eddy current.

- **The resistivity of the conductor**: The higher the resistivity of the conductor, the weaker the eddy current.

Eddy currents can be used for a variety of purposes, including:

- **Induction heating**: Eddy currents are used to heat objects in induction heating furnaces and equipment. This is done by placing the object in a coil of wire that is connected to an AC source. The changing magnetic field induces eddy currents in the object, which generate heat.
- **Electromagnetic braking**: Eddy currents are used to create a drag force on a moving object. This is done by placing the object in a magnetic field and then moving it through the field. The eddy currents that are induced in the object create a drag force that opposes its motion. This effect is used in eddy current brakes, which are used to stop rotating power tools quickly when they are turned off.
- **Non-destructive testing**: Eddy currents can be used to detect cracks and flaws in metal parts. This is done by passing an alternating current through the part and then measuring the induced eddy currents. The presence of a crack or flaw will distort the eddy currents, and this distortion can be used to detect the flaw.

Eddy currents can also be a source of energy loss in AC machine. This is because the eddy currents generate heat, which reduces the efficiency of the machine and cause a temperature rise. To reduce eddy current losses, AC machines is often constructed with laminated magnetic cores. Laminated magnetic cores are made up of thin sheets of metal that are separated by insulating material. This prevents the eddy currents from flowing freely through the core, and this reduces the amount of heat that is generated.

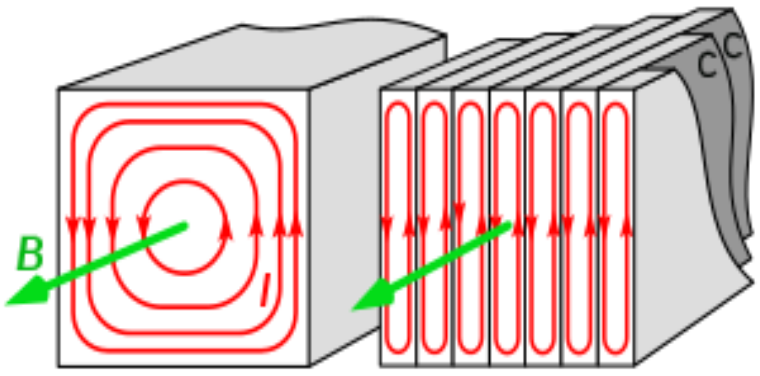

Figure 68: Eddy currents (I) within a solid iron core (left side) and parallel laminations with insulation (C) (right side) generated from the field (B) [33].

The use of surface permanent magnet (SPM) synchronous machines is becoming more popular [4] thanks to their compactness, high torque density and increased flux weakening performance . On the other side, eddy currents can be also induced inside the magnets for a SPM motor or generator. This is because magnets are conductors, and they must be placed in a changing magnetic field. When this happens, an EMF (electromotive force) is induced inside the magnets, and this EMF causes electrons in the magnets to flow, creating a current. The current flows in closed loops and generates heat inside the magnets. The figure in blow shows the current density inside the magnets of a SPM machine.

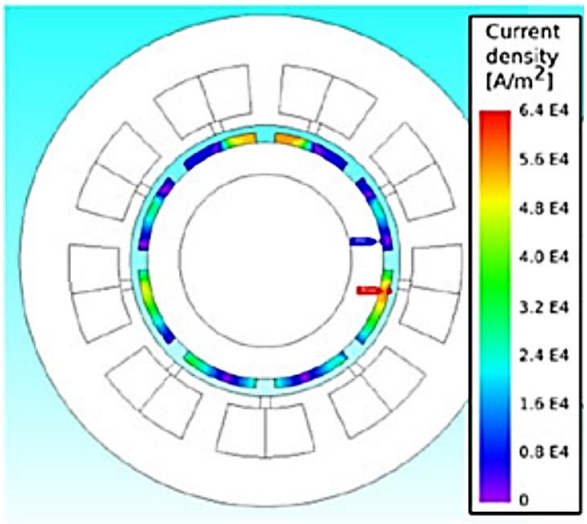

Figure 69: Current density inside the magnets of a SPM machine [34].

The magnitude of the eddy current is determined by several factors, including:

- **The amplitude of the non-synchronous harmonics content of the magnetic field**: The non-synchronous harmonics of the magnetic field are generated because of the non-sinusoidal distribution of the conductors along the stator periphery, which is especially true for concentrated winding designs.
- **The area of the magnet**: The larger the area of the magnet, the higher the eddy current.
- **The rate of change of the magnetic field**: The faster the magnetic field changes, the stronger the eddy current.

The air-gap field harmonic content causes eddy current losses in the permanent magnets placed on the surface of the rotor. For this reason, these magnets can be demagnetized due to overheating [7] [35]. Furthermore, spatial harmonics can decrease the performances of the electrical machines in terms of torque ripple and unbalanced magnetic pull.

To reduce eddy current losses in SPM motors and generators there are several techniques:

- **Increasing the magnets resistivity**: The magnets are often made of a material with a high resistivity. This makes it more difficult for eddy currents to flow, and this reduces the amount of heat that is generated.
- **Magnet segmentation:** By dividing a magnet pole into several magnet segments insulated between each other, the volume of the magnet can be reduced and subsequently increases its resistivity.
- **Optimizing the winding:** By optimizing the electric winding for the electric generator it could be possible to reduce the eddy current losses inside the SPM machine's magnets.

By reducing eddy current losses, SPM motors and generators can be more efficient and reliable.

This chapter will explore innovative strategies for optimizing the SPM machine winding configuration to effectively minimize eddy current losses within the SPM machine magnets without significantly compromising the generator's generated voltage.

9.1 Fractional-Slot Concentrated Windings

Significant advantages can be gained by equipping SPM machines with concentrated winding in the stator. In fact, using concentrated winding can be beneficial regarding easy manufacturing and consequently lower production costs, modularity [36] and fault tolerance. More particularly, short end-windings are a strong benefit in terms of copper saving and less joule losses.

A weakness of concentrated winding is a feasibility rule that imposes a constraint on the design of the machine. As it can be found in the literature [37], some numbers of slots and numbers of poles combinations are not feasible for the winding to be symmetrical. This limits the degree of freedom of the designer's choices. Furthermore, regardless of the feasibility, the slot-pole combinations are proven to have direct effect on machines performance in various aspects such as winding factor [38] [39], radial forces and vibration behavior [40] [41], cogging torque [42] [43], and leakage inductances [44].

The figure below shows an SPM machine with a traditional concentrated winding, where each tooth has a phase wound around it [45].

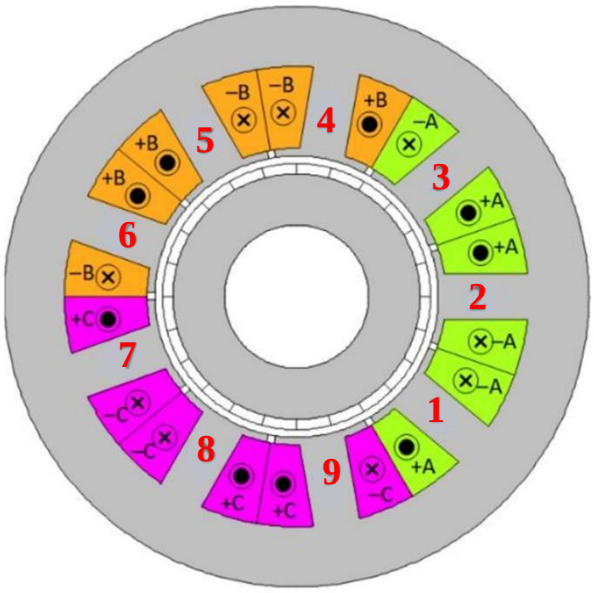

Figure 70: Cross section for a SPM machine with concentrated winding.

The three colours used indicate the three phases of the machine separately, in particular the green colour indicates the first phase (phase A), the orange colour indicates the second phase (phase B) and the purple colour indicates the third phase (phase C). In this particular machine, there are 8 poles with 9 teeth on the stator, therefore 3 teeth per phase.

Another way to present the winding of an electric machine is in linear mode, as shown in the figure below, where the stator is presented as if it were linear (unrolled along a line) and the colours of the phases are assigned around its teeth. The figure below shows the same winding configuration for the same machine but with the stator drawn in a linear way.

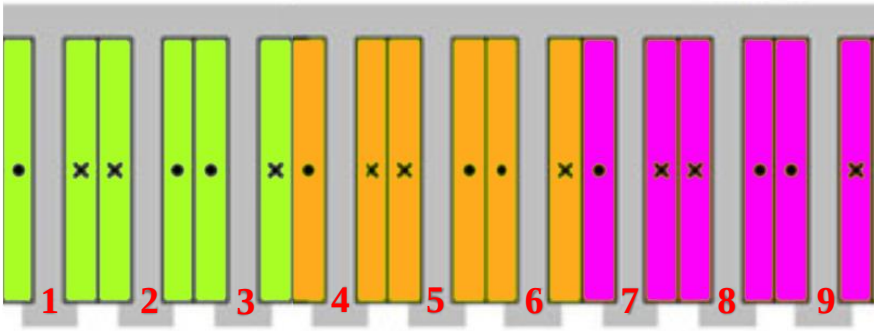

Figure 71: Linear presentation for a SPM machine with concentrated winding.

The traditional winding configuration for SPM machines with concentrated coils is simple to manufacture and provides good performance. However, it has the disadvantage of producing high eddy currents in the magnets.

Various provisions have been proposed in the literature to reduce the magnetic field harmonics content, consequently the eddy current losses, by modifying the machine winding. We can mention combined star-delta connections among the coils of a phase and use of multi-phase configurations [46], or the adoption of multi-layer arrangements in which more coils, belonging to different phases, are wound around the same tooth [47] [48] [49].

In [34], an analytical method is outlined to optimize Fractional-Slot Concentrated Windings (FSCW) for Surface Permanent Magnet (SPM) machines. This method leverages Quadratic Programming to minimize eddy current losses while also seeking to maximize the amplitude of the first harmonic of the magneto-motive force (MMF) responsible for the SPM machine output voltage and power.

When applying this optimization method to the previously introduced SPM machine model, a Pareto front was obtained. In this graph, the x-axis represents the reduction of the fundamental of the magneto-motive force (MMF), and the y-axis represents the reduction of the eddy current losses. Each point on the Pareto front corresponds to a different configuration of the three-phase winding for the machine. The figure below illustrates this concept.

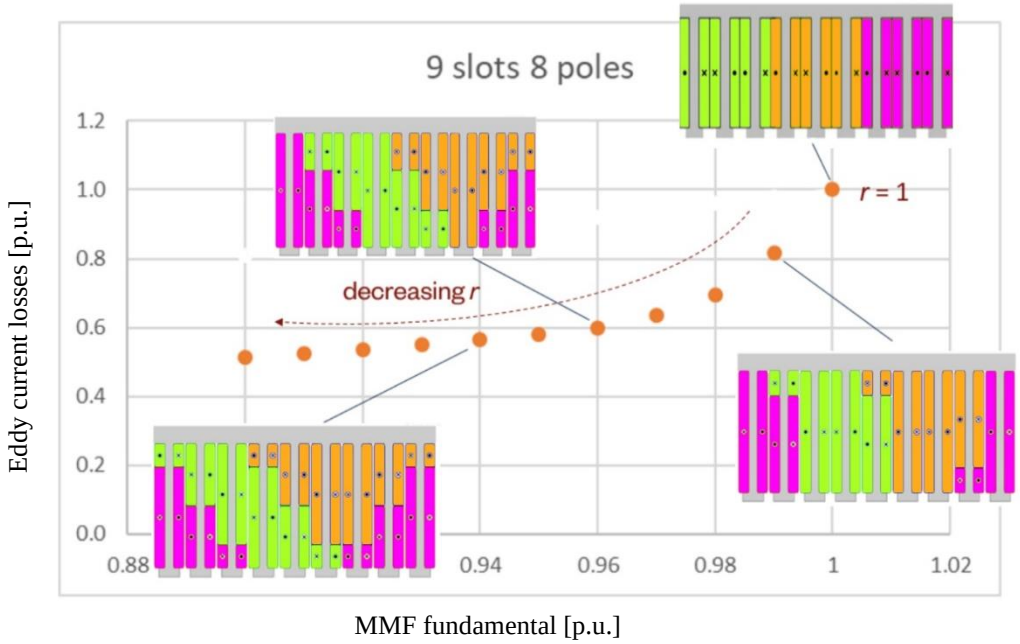

Figure 72: Pareto front for the eddy current losses vs. the MMF fundamental.

As shown, there is a trade-off between minimizing losses and maximizing the amplitude of the first harmonic of the MMF. As the losses decrease, the amplitude

of the first harmonic also diminishes, leading to a corresponding reduction in output voltage.

9.1.1 Application of the Fractional Slot Concentrated Windings Method on the SPM Machine Designed in this Thesis

To minimize the eddy current losses in the Surface Permanent Magnet (SPM) machine designed for this thesis, the method discussed earlier was applied. Specifically, this approach was implemented on a three-phase SPM generator with 84 stator teeth and 80 poles. The study used an analytical approach for calculations, and finite element simulations (via Flux software from Altair) were employed to validate the results.

In the reference article [34], the rotor magnets are modelled simplistically as a magnetic ring, where eddy currents are generated, leading to losses as a result of the magnetic field harmonics produced by the stator windings. While this analytical method is straightforward to apply, it involves simplifications in the geometry of the magnets, which can result in less accurate predictions. The article also describes how the stator winding is modified by employing multiple coils from different phases around the same tooth ("multi-layer" configuration) to reduce magnet losses. However, this modification slightly reduces the generator's output voltage.

To apply this method, an on-purpose algorithm was developed using MATLAB for analytical computation. The algorithm takes several electrical and mechanical parameters as inputs, including:

Electrical Parameters:

- Machine current
- Number of phases
- Machine electrical frequency

Mechanical Parameters:

- Stator inner radius
- Rotor radius
- Air gap
- Magnet height
- Machine length
- Number of slots
- Number of poles

- Maximum number of turns per stator tooth

The algorithm also uses several standard constants for its calculations, such as:

- Magnet conductivity
- Air permeability

This approach allowed for a detailed analysis of the generator's performance considering the trade-offs between reducing eddy current losses and maintaining sufficient output voltage. Through the combination of analytical methods and finite element analysis, this study provides a more comprehensive view of the machine's behavior, balancing efficiency and performance in a practical design.

9.1.2 Star of Slots Method for Traditional Winding Calculation

The MATLAB algorithm utilizes the provided input parameters to calculate the traditional winding configuration using the star of slots method. This method produces a table where the rows represent the machine teeth, the columns represent the phase phasors, and the number in each cell indicates the number of turns around that specific tooth. Since the machine under study is three-phase, six phasors can be identified, as shown in the figure below. These phasors represent the three phases and their corresponding negative counterparts.

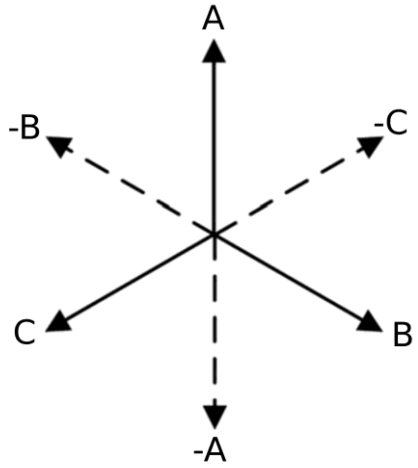

Figure 73: Three phases system space vectors.

The table below shows the winding configuration for the first 21 teeth of the machine, calculated using the star of slots method.

		Phasor					
		A	**-C**	**B**	**-A**	**C**	**-B**
Tooth	**1**	18	0	0	0	0	0
	2	0	0	0	18	0	0
	3	18	0	0	0	0	0
	4	0	0	0	18	0	0
	5	0	0	0	0	0	18
	6	0	0	18	0	0	0
	7	0	0	0	0	0	18
	8	0	0	18	0	0	0
	9	0	0	0	0	0	18
	10	0	0	18	0	0	0
	11	0	0	0	0	0	18
	12	0	18	0	0	0	0
	13	0	0	0	0	18	0
	14	0	18	0	0	0	0
	15	0	0	0	0	18	0
	16	0	18	0	0	0	0
	17	0	0	0	0	18	0
	18	0	18	0	0	0	0
	19	0	0	0	18	0	0
	20	18	0	0	0	0	0
	21	0	0	0	18	0	0

Table 4: SPM machine winding for the first 21 slots obtained with star of slots algorithm.

This table can be further simplified into one that contains only three columns, corresponding to the three phases. In this simplified table, each phase has a positive number, representing one direction of winding, and a negative number, representing the opposite winding direction. The simplified table is shown below.

		Phase		
		A	**B**	**C**
Tooth	**1**	18	0	0
	2	-18	0	0
	3	18	0	0
	4	-18	0	0
	5	0	-18	0
	6	0	18	0
	7	0	-18	0
	8	0	18	0
	9	0	-18	0
	10	0	18	0
	11	0	-18	0
	12	0	0	18
	13	0	0	-18
	14	0	0	18
	15	0	0	-18
	16	0	0	18
	17	0	0	-18
	18	0	0	-18

	19	-18	0	0
	20	18	0	0
	21	-18	0	0

Table 5: SPM machine winding for the first 21 slots transformed in 3 phases.

The Fractional-Slot Concentrated Windings (FSCW) algorithm uses the table generated by the star of slots method, with the six phasors, to create a winding vector x, of length 2m×Z, where m is the number of phases and Z is the number of teeth. Thus, the vector x is structured as shown in the figure below. This is the vector that is optimized using quadratic programming to minimize losses and maximize the output voltage of the machine.

Figure 74: The x vector used for the winding optimization with the Fractional-slot concentrated algorithm.

9.1.3 Harmonic Content Calculation and Quadratic Programming Optimization for Winding Design

Before optimizing the winding vector, it is essential to calculate the harmonics $m_n^{\pm}$ of the magnetic field generated by the winding. This harmonic content includes the fundamental harmonic with an order n corresponding to the number of pole pairs, responsible for generating output voltage of the machine. Additionally, it includes other harmonics that induce eddy currents in the magnets, causing losses. This harmonic content is determined by applying the following four equations, where Z represents the number of teeth and I_0 represents the machine current.

$$a_n = \frac{2}{n*\pi}(-1)^n * \sin(\frac{n*\pi*(Z-1)}{Z})$$

Equation 39

$$[v_n^{\pm}]_h = \frac{1}{2} a_n I_0 e^{i\left[-\frac{\pi}{3} mod(h,6) \mp n\frac{2\pi}{Z} floor(h,6)\right]} \quad \forall h = 0..6Z-1$$

Equation 40

$$Q_n^{\pm} = Re\{v_n^{\pm}\} + Re\left\{v_n^{\pm T}\right\} + Im\{v_n^{\pm}\} + Im\left\{v_n^{\pm T}\right\}$$

Equation 41

$$m_n{}^{\pm} = \sqrt{x^T \, Q_n{}^{\pm} \, x}$$

Equation 42

These equations, present in [34], were applied to calculate harmonic content for up to 100 harmonics. The graph below shows the fundamental harmonic at $n = 40$, as this machine has 40 pole pairs, making this harmonic the one responsible for generating the machine's output voltage. The remaining harmonics contribute to losses in the machine.

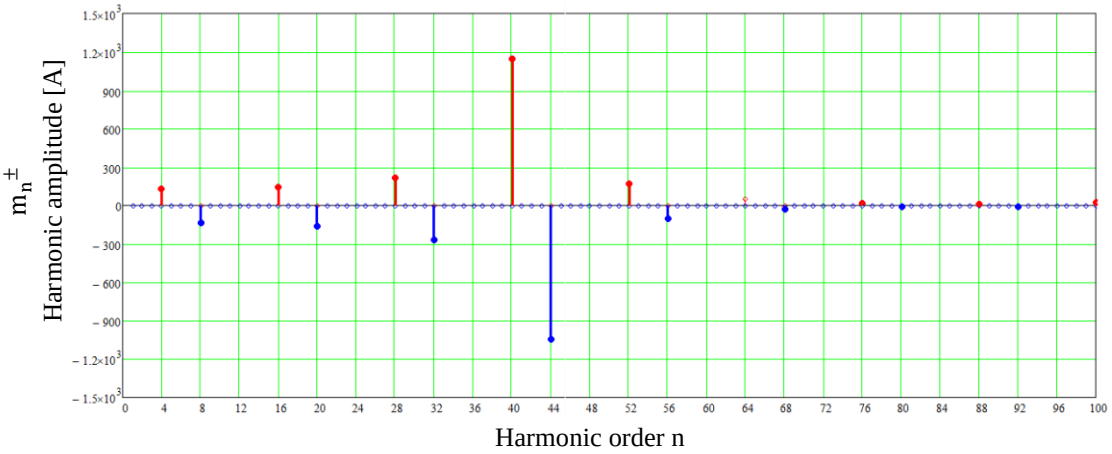

Figure 75: SPM machine MMF spectrum for the traditional star slot winding.

In the article [34], quadratic programming is introduced as a method for optimizing the winding design. To utilize this optimization method, two objective functions were defined: $f_{fund}(x)$ and $f_{loss}(x)$. The function $f_{fund}(x)$ is a quadratic function representing the fundamental harmonic amplitude of the magnetic field, which should be kept as high as possible. This harmonic corresponds to $n = p$, where p is the number of pole pairs. On the other hand, $f_{loss}(x)$ is a quadratic function that represents the losses caused in the magnet by the remaining harmonic content, which needs to be minimized. The following two equations [34] show how these functions are modeled.

$$f_{fund}(x) = \; -x^T \, Q_p \, x$$

Equation 43

$$f_{loss}(x) = \; x^T \left[\sum_{n=1..\infty} \left(p_n{}^{+} * Q_n{}^{+} + \; p_n{}^{-} * Q_n{}^{-} \right) \right] x$$

Equation 44

Here, $p_n^{\pm}$ represents the per-unit losses in the magnet caused by the *n-th* harmonic of the MMF.

Quadratic programming aims to minimize or maximize a function subject to certain constraints. The objective function to be optimized should take the form [34]:

$$\frac{1}{2}\, x^T\, H\, x + \, f^T\, x$$

Where H is a symmetric matrix and $f^T\, x$ represents the linear part of the function. In this case, the term $f^T\, x$ is discarded, and H is structured as follows [34]:

$$H = (1 - \omega)\, f_{fund}(x) + \omega\, f_{loss}(x)$$

where ω is a weight coefficient ∈ [0,1].

The second important part of the quadratic programming is the constrains to be satisfied. The quadratic programming constrains can be represented in the following form [34]:

$$A\, x \leq b$$

$$A_{eq}\, x = \, b_{eq}$$

$$l_b \, \leq x \, \leq \, u_b$$

In this case the constraints to be satisfied are the following three:

1. The number of turns per tooth must not exceed the maximum number N_0.
2. All elements of the vector x must be non-negative.
3. The winding symmetry must be respected to produce a consistent fundamental MMF at all times.

Before running the optimization algorithm, a minimum threshold for the fundamental MMF is chosen, below which the optimization cannot proceed. This means the algorithm will optimize the winding to minimize losses while ensuring the fundamental MMF remains above a certain value, thereby striking a balance between minimizing losses and maintaining sufficient output voltage.

Applying this algorithm to the machine with 84 slots and 80 poles studied in this thesis resulted in the Pareto front shown below.

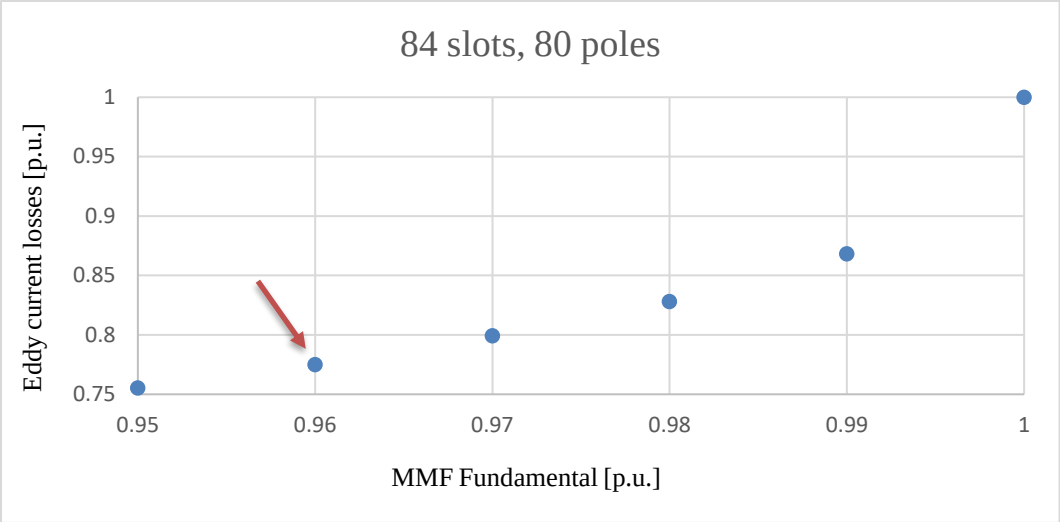

Figure 76: Pareto front for the eddy current losses reduction with the MMF fundamental reduction by using the fractional slot concentrated winding method.

From the points on the Pareto front, the decision was made to use the point that reduces losses to 77% while maintaining the fundamental MMF at 96%. The table below shows the winding configuration obtained from this point on the Pareto front.

		Phase		
		A	**B**	**C**
Tooth	**1**	18.0	0.0	0.0
	2	-15.8	2.2	0.0
	3	13.3	-4.7	0.0
	4	-10.4	7.6	0.0
	5	7.6	-10.4	0.0
	6	-4.7	13.3	0.0
	7	2.2	-15.8	0.0
	8	0.0	18.0	0.0
	9	0.0	-15.8	2.2
	10	0.0	13.3	-4.7
	11	0.0	-10.4	7.6
	12	0.0	7.6	-10.4
	13	0.0	-4.7	13.3
	14	0.0	2.2	-15.8
	15	0.0	0.0	18.0
	16	2.2	0.0	-15.8
	17	-4.7	0.0	13.3
	18	7.6	0.0	-10.4
	19	-10.4	0.0	7.6
	20	13.3	0.0	-4.7
	21	-15.8	0.0	2.2

Table 6: SPM machine new winding for the first 21 slots by using the fractional slot concentrated winding method to reduce losses to 77% and MMF fundamental to 96%.

In a real machine, the number of turns in a winding cannot be fractional; it must be an integer. As a result, the number of turns in this configuration was rounded to the nearest whole number.

9.1.4 Verification of the Efficiency of the Fractional-Slot Concentrated Windings Method

To verify the efficiency of the Fractional-Slot Concentrated Windings (FSCW) method, the machine was modeled using finite element modeling (FEM) in the Altair Flux software. The simulation compared the performance of the original winding configuration with the new multi-layer winding designed to reduce losses. This comparison aimed to assess the effectiveness of the optimization algorithm in minimizing eddy current losses and maintaining machine performance.

The figure below illustrates the difference between the original winding (on the left) and the new multi-layer winding (on the right), using the geometric model of the machine employed for the FEM. Specifically, the red color represents phase A, green represents phase B, and yellow represents phase C. The multi-layer configuration uses multiple coils of different phases wound around the same stator teeth, which was expected to reduce losses while maintaining similar output performance.

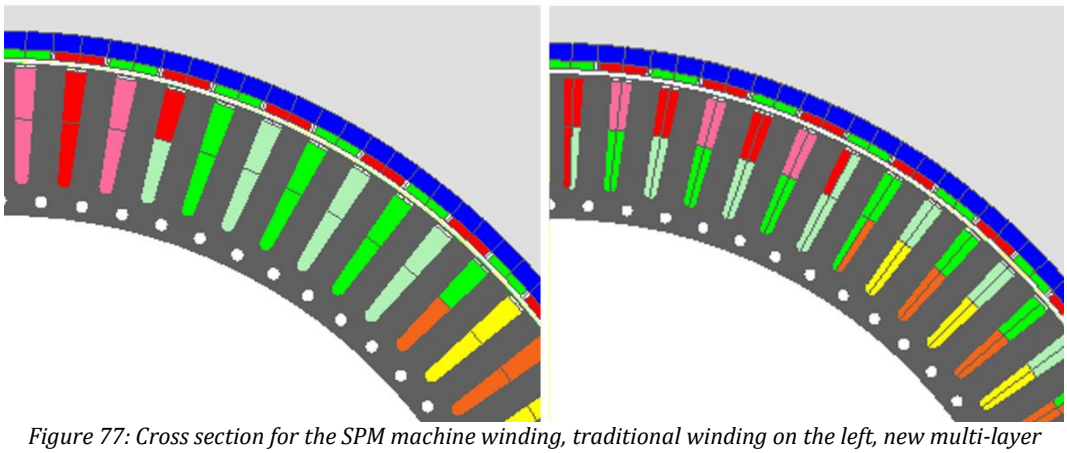

Figure 77: Cross section for the SPM machine winding, traditional winding on the left, new multi-layer winding on the right.

When applying this new winding structure to the Flux finite element model of the electric machine, the simulation yielded results that differed from the expected values based on the simplified model. The table below shows that the simulation reported higher voltage and losses than anticipated.

	Traditional winding	Analytical calculation	Flux simulation
Output voltage E_0	272 V	261.12 V (96%)	264.9 V (97.4%)
Eddy current losses	207.72 W	159.94 W (77%)	182.84 W (88%)

Table 7: Difference between the analytical calculation and fem simulation for the output voltage and eddy current losses by using the fractional-slot concentrated winding.

These discrepancies highlight the limitations of the simplified analytical models and the need for more precise simulations to capture the machine's complex electromagnetic interactions. The results indicate that while the optimized winding configuration does lead to improved performance compared to the traditional winding, the extent of improvement in terms of reduced losses and output voltage requires further refinement to align with theoretical expectations.

9.2 Magnet Circumferential Segmentation

As an alternative to the initial simplified analytical model, a more accurate approach was considered, where the permanent magnets are not treated as a single magnetic ring but are instead modelled as individual magnet segments. This enhanced analytical model, presented in the article [50], offers a more precise representation of the magnetic field behavior and eddy current losses.

In this model, the Laplace and Poisson equations are solved analytically to determine the magnetic field in the air gap and within the permanent magnets. The model also accounts for the current density field inside the magnets, which is crucial for accurately predicting the eddy current distribution and corresponding losses.

This advanced model allows for a more detailed analysis of the magnetic field interactions, particularly in machines with segmented magnets, which is a common design feature in high-performance Surface Permanent Magnet (SPM) machines. By providing a more accurate representation of the field distribution in both the air gap and the magnet segments, this method improves the prediction of losses compared to the simplified model, which assumed a continuous magnetic ring.

The results from this model can better inform the design choices for minimizing eddy current losses while maintaining efficient operation in SPM machines, especially when compared to the multi-layer winding configurations explored earlier. Moreover, this more accurate analytical approach helps bridge the gap between simplified theoretical predictions and the more complex real-world behavior observed in finite element simulations.

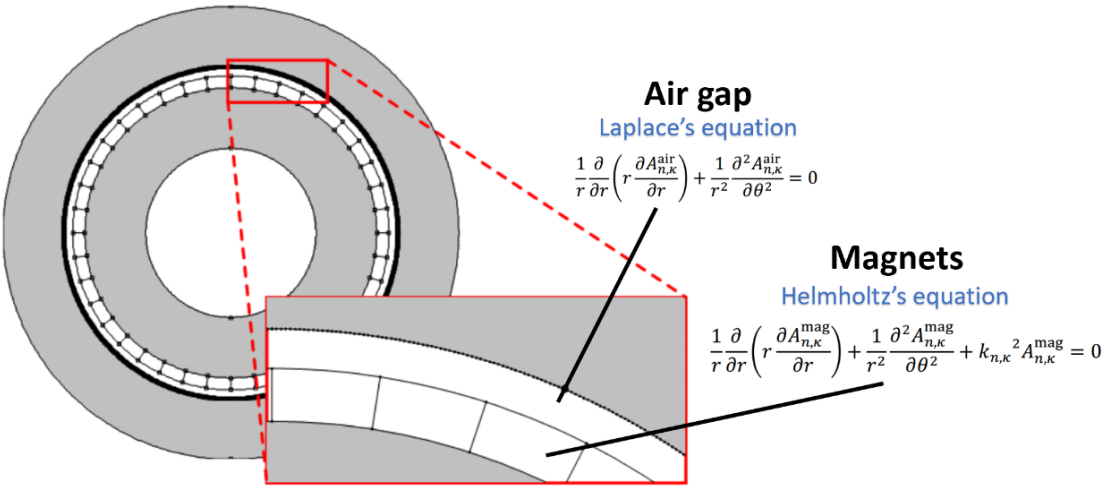

Figure 78: Representation of the air gap and segmented magnets used in [50].

9.2.1 Application of the Magnet Circumferential Segmentation Winding Method on the SPM Machine Designed in this Thesis

The second analytical model presented in [50] significantly differs from the first model, particularly in the calculation of eddy current losses constants, denoted as ${p_n}^{\pm}$. Unlike the earlier approach, where the magnets were treated as a single continuous ring, this model considers each magnet as a separate segment, allowing for a more precise representation of the magnetic behavior.

In Figure 79 of the referenced article, a flow chart is provided that outlines the steps required to calculate the eddy current losses. The inputs for this flow chart include:

- The electrical and mechanical parameters of the machine.
- The stator angular frequency.
- The space harmonic parameters of the magnetic motive force (MMF) to be considered.

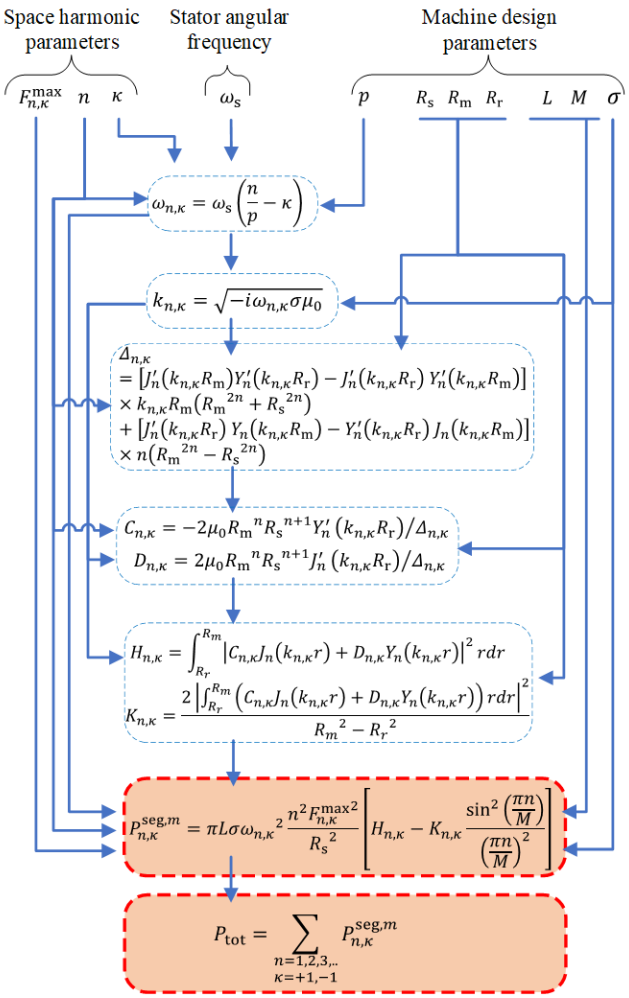

Figure 79: Flow chart summarizing the procedure for permanent magnet loss computation, from the input data to the final formula [51].

By implementing this analytical model in MATLAB, a new Pareto front was obtained, showing the trade-off between the reduction in eddy current losses and the reduction in the fundamental MMF. Figure 80 demonstrates that the loss reduction is slightly greater than in the previous case. For instance, it shows a reduction of 88% in eddy current losses at a 97.4% reduction in the fundamental MMF. This result aligns closely with the findings of the Flux simulation applied to the earlier model, using the Fractional-Slot Concentrated Windings (FSCW) algorithm.

As shown, the second model produces more accurate results due to a critical difference in how the eddy current flows are treated. In this model, the currents are in fact required to close within each individual magnet segment, ensuring that the total current in each segment remains zero. This is a crucial improvement over the previous method, which oversimplified the magnetic behavior by treating the rotor as a continuous magnetic ring.

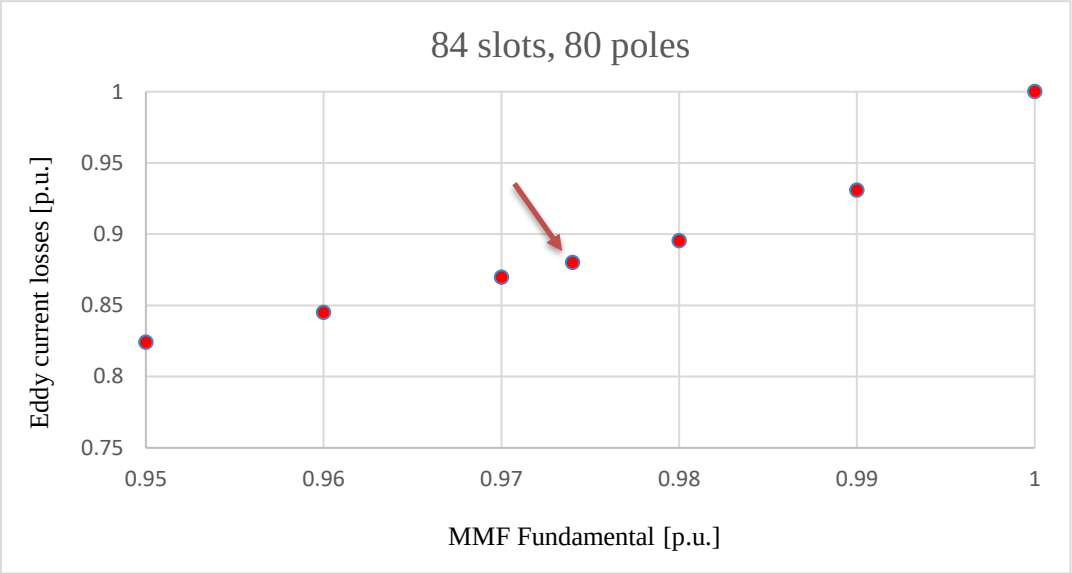

Figure 80: Pareto front for the eddy current losses reduction with the MMF fundamental reduction by using the magnet circumferential segmentation method.

To allow for a real comparison between the two methods, an optimized winding design was chosen, which reduced the fundamental MMF (and consequently the machine's output voltage) to 97.4% while achieving an 88% reduction in eddy current losses. This point on the Pareto front resulted in a winding configuration that is similar, but not identical, to the one obtained using the previous method. This optimized winding configuration is detailed in Table 8.

		Phase		
		A	**B**	**C**
Tooth	**1**	18.0	0.0	0.0
	2	-15.8	2.2	0.0
	3	13.3	-4.7	0.0
	4	-10.4	7.6	0.0
	5	7.6	-10.4	0.0
	6	-4.7	13.3	0.0
	7	2.2	-15.8	0.0
	8	0.0	18.0	0.0
	9	0.0	-15.8	2.2
	10	0.0	13.3	-4.7
	11	0.0	-10.4	7.6
	12	0.0	7.6	-10.4
	13	0.0	-4.7	13.3
	14	0.0	2.2	-15.8
	15	0.0	0.0	18.0
	16	2.2	0.0	-15.8
	17	-4.7	0.0	13.3
	18	7.6	0.0	-10.4
	19	-10.4	0.0	7.6
	20	13.3	0.0	-4.7
	21	-15.8	0.0	2.2

Table 8: SPM machine winding for the first 21 slots by using the magnet circumferential segmentation method to reduce losses to 88% and MMF fundamental to 97.4%.

As mentioned above, the number of turns in the winding must be an integer in a real machine, so the fractional values obtained in the analysis were approximated to the nearest whole numbers.

9.2.2 Verification of the Efficiency of the Magnet Circumferential Segmentation Method

As shown in the table below, the results obtained with the new analytical model demonstrate significantly higher precision, aligning very closely with the independent numerical simulations conducted using finite element analysis (FEM) in the Flux software.

	Traditional winding	Analytical calculation	Flux simulation
Output voltage E_0	272 V	264.9 (97.4%)	264.6 V (98.4%)
Eddy current losses	207.72 W	182.84 (88%)	185.49 W (89.3%)

Table 9: Difference between the analytical calculation and fem simulation for the MMF and eddy current losses by using the magnet circumferential segmentation method.

By comparing the results obtained through both methods, it is possible to observe how the Pareto front changes between the two approaches. The Magnet Circumferential Segmentation method yields more accurate results, as evidenced by the detailed comparison in the figure below.

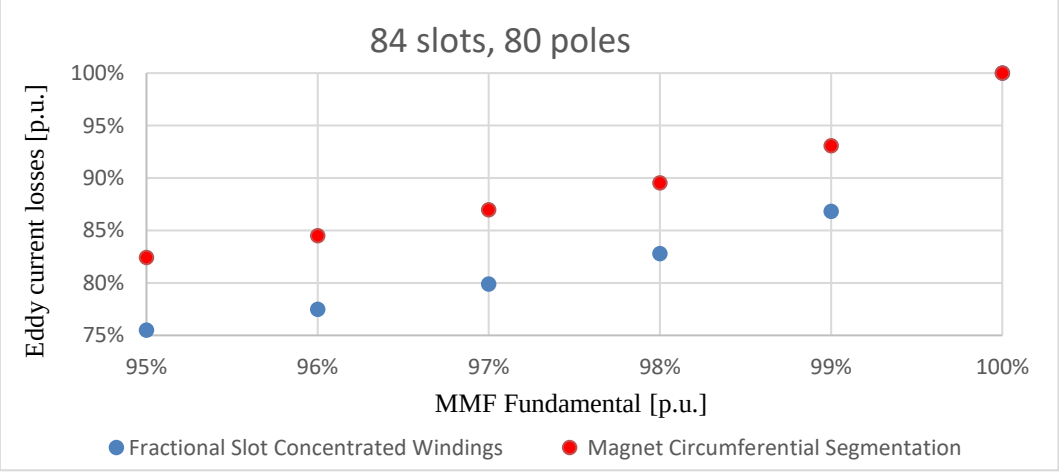

Figure 81: Pareto front for the eddy current losses reduction with the MMF fundamental reduction by using both the fractional slot concentrated windings and the magnet circumferential segmentation methods.

This figure illustrates the improved precision of the new model over the previous one, particularly in predicting the trade-off between eddy current losses and the fundamental MMF. In both cases, the goal is to reduce losses while maintaining a high fundamental MMF. However, the new method clearly outperforms the earlier one, producing a more optimal winding configuration that minimizes losses while ensuring effective machine performance.

The Magnet Circumferential Segmentation method's ability to model each magnet individually leads to a more accurate representation of eddy current paths and better results in optimizing the winding arrangement. This is a crucial step forward in the design of high-efficiency SPM machines.

9.2.3 Advanced Magnet Segmentation Techniques for SPM Machines

The Fractional-Slot Concentrated Windings method simplifies the modelling of the SPM machine by representing it with a single magnet in the form of a circular ring. In contrast, the Magnet Circumferential Segmentation method adopts a more granular approach by modelling the SPM machine with M segments of magnets, where in this case M=80.

This Magnet Circumferential Segmentation method can be further extended to accommodate different magnet segmentations. For instance, each magnet can be divided into two parts, resulting in M=160, or into three parts, leading to M=240. The Figure 82 illustrates various segmentation configurations explored throughout this thesis.

In this particular analysis, the optimal reduction of eddy current losses is achieved with a segmentation of M=80, indicating the use of a single magnet per pole. This approach not only enhances the accuracy of the magnetic field representation but also contributes to improved overall efficiency in the machine's performance.

The ability to adjust the segmentation of the magnets opens up new avenues for optimizing SPM machines, allowing for tailored solutions based on specific operational requirements and performance objectives. This flexibility is crucial for advancing the design of high-efficiency electric machines in the quest for sustainable energy solutions.

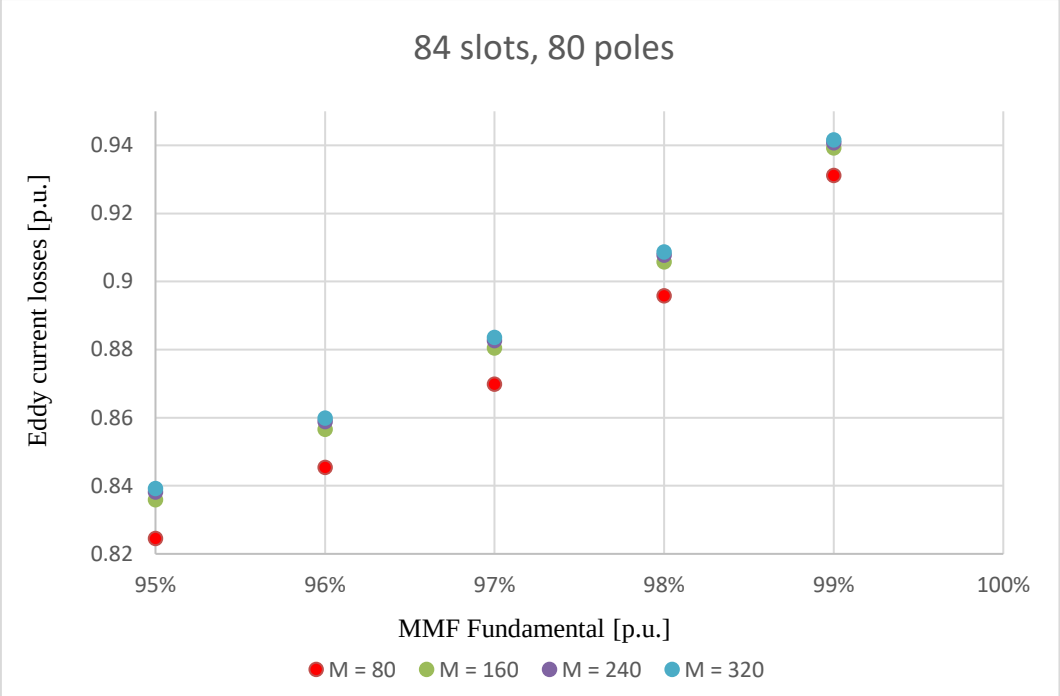

Figure 82: Pareto front for the eddy current losses reduction with the MMF fundamental reduction by using the magnet circumferential segmentation methods with different magnet segmentations.

9.3 Optimization for The Magnet Circumferential Segmentation Algorithm

This study has demonstrated that the efficiency of surface permanent magnet synchronous generators can be optimized by refining the winding design without altering the geometry of the generator, thereby enhancing the overall performance of the system. The general methodology for generating an optimized multi-phase winding aimed at reducing losses in permanent magnets is outlined in the following article [51].

As observed, the Magnet Circumferential Segmentation method yields significantly more accurate results compared to the Fractional-Slot Concentrated Windings approach. However, a small discrepancy still exists between the results obtained through the Magnet Circumferential Segmentation analytical method and those derived from finite element simulations. This difference may stem from various factors, including:

1. **Slot Openings:** The simplification of slot openings in the machine's design may not be adequately accounted for in the analytical model.

2. **Air Gap between magnets Considerations:** The magnetic air gap between the magnets is another critical factor that could influence the results and may not have been fully integrated into the analytical approach.

3. **Winding Approximations:** Approximating the winding to an integer number of turns per tooth could introduce additional variances, affecting the fidelity of the model.

Future studies can focus on incorporating these elements into the analytical model to achieve results that are more accurate and closely aligned with finite element simulations. By refining the analytical framework to include these considerations, the potential for improved predictive accuracy in the performance of surface permanent magnet synchronous generators can be realized, paving the way for further advancements in generator design and optimization.

Conclusion

This thesis has provided an in-depth analysis of the integration of screw turbines with Surface Permanent Magnet (SPM) synchronous machines in small hydropower plants, underscoring the importance of these systems in advancing renewable energy technologies. As the global community grapples with the pressing challenges of climate change and the urgent need to reduce greenhouse gas emissions, small hydropower plants emerge as a promising solution, blending environmental sustainability with efficient energy generation.

The initial chapters of this work have contextualized the significance of small hydropower systems within the broader renewable energy landscape. By emphasizing the advantages of small-scale installations such as lower environmental impacts, reduced capital investment, and suitability for distributed generation this thesis advocates for the increased adoption of small hydropower projects. This perspective is especially pertinent in regions with abundant water resources, where small hydropower can complement other renewable sources and contribute to a diversified energy portfolio.

Central to this research has been the innovative design of screw turbines, which have shown exceptional adaptability to various hydrological conditions. The exploration of new technological solutions and design principles has illustrated how screw turbines can enhance operational efficiency while minimizing maintenance needs. By integrating these turbines with SPM synchronous machines, we have demonstrated a synergistic approach that optimizes energy conversion processes, leading to improved overall system performance.

The extensive examination of SPM generators has revealed their potential to revolutionize small hydropower applications. Our analysis has delved into the intricate engineering principles governing the design and operation of these machines. We have highlighted strategies to enhance efficiency and reliability. The detailed investigations into the various design parameters, including pole and slot configurations, winding arrangements, and thermal management systems, contribute to a deeper understanding of the technical challenges and opportunities in SPM generator development.

In addition to the technical aspects, this research has placed significant emphasis on the control systems that govern the operation of SPM generators. The field-oriented control (FOC) method has been scrutinized for its precision and effectiveness in managing the torque and speed of electric machines. The thorough analysis of its implementation, along with the exploration of diode bridges, boost converters, and

dual inverter systems, has demonstrated the critical role of power electronics in optimizing the performance of small hydropower systems. These control strategies not only enhance system reliability but also ensure responsiveness to varying load conditions, thus maximizing energy output.

Moreover, the economic assessment of SPM generator deployment within the Italian market context has provided invaluable insights into the financial viability of small hydropower projects. By detailing the breakdown of costs associated with materials, manufacturing, and integration, this thesis presents a comprehensive overview of the economic landscape for small hydropower systems. The findings suggest that, with careful consideration of design and operational parameters, these projects can achieve favorable return on investment, making them attractive options for both private investors and public utilities.

A significant contribution of this research is the innovative approach to reducing eddy current losses in SPM machines, which can adversely affect efficiency and operational longevity. By proposing alterations to winding configurations without modifying machine geometry, we have introduced a novel solution that promises to enhance performance and safe operation in terms of permanent magnet possible overheating. This finding is particularly relevant as the industry continues to seek methods to improve the sustainability and competitiveness of hydropower systems.

In conclusion, this thesis not only advances the understanding of SPM generators in small hydropower applications but also introduces practical solutions to enhance their performance and economic feasibility. By bridging the gap between traditional hydropower techniques and modern engineering innovations, this research paves the way for more efficient, reliable, and eco-friendly energy generation systems. The insights gleaned from this study serve as a foundation for future research endeavours aimed at optimizing small hydropower technology, ultimately contributing to the global transition towards a more sustainable energy future.

As we look to the future, it is essential that researchers, engineers, and policymakers continue to collaborate to overcome the challenges faced by small hydropower systems. By fostering innovation and investment in this field, we can unlock the full potential of small hydropower plants, ensuring they play a vital role in the quest for a cleaner, more sustainable world.

Bibliography

[1] O. Saad and C. Abdeljebbar, "Historical Literature Review of Optimal Placement of Electrical Devices in Power Systems: Critical Analysis of Renewable Distributed Generation Efforts," *IEEE Systems Journal,* vol. 15, pp. 3820-3831, 2021.

[2] G. Behal and K. Laing, "Global Hydropower: Current Developments and Future Innovations," *IEEE Power and Energy Magazine,* vol. 18, no. 5, pp. 16-17, 2020.

[3] "Gilbert Gilkes & Gordon," [Online]. Available: https://www.gilkes.com/small-hydropower-solutions/gilkes-turbines/pelton-turbines. [Accessed 14 August 2023].

[4] A. M. El-Refaie, "Fractional-Slot Concentrated-Windings Synchronous Permanent Magnet Machines: Opportunities and Challenges," *IEEE Transactions on Industrial Electronics,* vol. 57, no. 1, pp. 107-121, 2010.

[5] T. Wegiel and D. Borkowski, "Variable Speed Small Hydropower Plant," in *3rd IEEE International Symposium on Power Electronics for Distributed Generation Systems (PEDG)*, Aalborg, Denmark, 2012.

[6] "Pengky," [Online]. Available: https://www.pengky.cn/zz-direct-drive-turbine/external-rotor-generator/external-rotor-generator.html. [Accessed 3 January 2024].

[7] N. Bianchi and E. Fornasiero, "Impact of MMF space harmonic on rotor losses in fractional-slot Permanent-Magnet machines," *IEEE Transactions on Energy Conversion,* vol. 24, no. 2, pp. 323-328, June 2009.

[8] "Energy Education," [Online]. Available: https://energyeducation.ca/encyclopedia/Pelton_turbine. [Accessed 14 August 2023].

[9] "Energy Education," [Online]. Available: https://energyeducation.ca/encyclopedia/Francis_turbine. [Accessed 14 August 2023].

[10] "Savree," [Online]. Available: https://savree.com/en/encyclopedia/francis-turbine-cross-section. [Accessed 14 August 2023].

[11] "Energy Education," [Online]. Available: https://energyeducation.ca/encyclopedia/Kaplan_turbine. [Accessed 14 August 2023].

[12] "Eco Evolution," [Online]. Available: http://ecoevolution.ie/blog/the-benefits-of-an-archimedean-screw-hydropower-turbine. [Accessed 8 August 2023].

[13] K. Mansour, M. Mezzarobba, M. De Martin and A. Tessarolo, "A New Turbine-Generator Integrated Concept Design for Screw-Turbine-Based Small Hydropower Plants," in *ICCEP 2023*, Terrasini, Italy, 2023.

[14] C. S. Bruk, "Tata Steel Europe," [Online]. Available: https://www.tatasteeluk.com/sites/default/files/m800-100a.pdf. [Accessed 5 December 2023].

[15] D. Meeker, "Finite Element Method Magnetics," [Online]. Available: https://www.femm.info/wiki/HomePage. [Accessed 5 December 2023].

[16] D. Borkowski, "Analytical Model of Small Hydropower Plant Working at Variable Speed," *IEEE Transactions on Energy Conversion*, vol. 33, no. 4, pp. 1886-1894, December 2018.

[17] D. Borkowski, "Maximum Efficiency Point Tracking (MEPT) for Variable Speed Small Hydropower Plant With Neural Network Based Estimation of Turbine Discharge," *IEEE Transactions on Energy Conversion*, vol. 32, no. 3, pp. 1090-1098, September 2017.

[18] D. Borkowski, "Average-value model of energy conversion system consisting of PMSG, diode bridge rectifier and DPC-SVM controlled inverter," in *International Symposium on Electrical Machines (SME)*, Naleczow, Poland, 2017.

[19] Y. Jiang, Meng Fan Rong and L. Y. Hua, "Variable Speed Constant Frequency Tidal Current Energy Generation and Control Strategy for Maximum Power Point Tracking and Grid Connection," *International Conference on Sustainable Power Generation and Supply*, April 2009.

[20] "All about circuits," [Online]. Available: https://www.allaboutcircuits.com/technical-articles/understanding-the-operation-of-a-boost-converter/. [Accessed 11 November 2023].

[21] Basic Calculation of a Boost Converter's Power Stage, Texas Instruments Incorporated, 2022.

[22] D. Borkowski and T. We, "Small Hydropower Plant With Integrated Turbine-Generators Working at Variable Speed," *IEEE Transactions on Energy Conversion*, vol. 28, no. 2, pp. 452-459, June 2013.

[23] C. B. Albuquerque and F. A. Moreno Vásquez, "Modeling and Control of Isolated Modular Hydrokinetic Energy Systems," in *Workshop on Communication Networks and Power Systems (WCNPS)*, Brasilia, Brazil, 2021.

[24] "All about circuits," [Online]. Available: https://www.allaboutcircuits.com/technical-articles/all-about-the-inverting-buck-boost-converter. [Accessed 30 November 2023].

[25] L. Belhadji, S. Bacha and D. Roye, "Modeling and Control of Variable-speed Micro-Hydropower Plant Based on Axial-flow turbine and Permanent Magnet Synchronous Generator (MHPP-PMSG)," in *IECON 2011 - 37th Annual Conference of the IEEE Industrial Electronics Society*, Melbourne, VIC, Australia, 2011.

[26] Z. Zhou, W. Knapp, J. MacEnri, H. C. Sorensen, E. F. Madsen, I. Masters and P. Igic, "Permanent Magnet Generator Control and Electrical System Configuration for Wave Dragon MW Wave Energy Take-off System," in *IEEE International Symposium on Industrial Electronics*, Cambridge, UK, 2008.

[27] U. Nasir, Z. Iqbal, M. Rasheed and H. Minxiao, "Active and Reactive Power Control of a Variable Speed Pumped Storage System," *IEEE 15th International Conference on Environment and Electrical Engineering (EEEIC)*, June 2015.

[28] "Wikipedia," [Online]. Available: https://en.wikipedia.org/wiki/Vector_control_(motor). [Accessed 6 December 2023].

[29] I. Boldea and S. Nasar, The Electric Generators Handbook - Variable Speed Generators, Productivity Press.

[30] L. Belhadji, S. Bacha, I. Munteanu, A. Rumeau and D. Roye, "Adaptive MPPT Applied to Variable-Speed Microhydropower Plant," *IEEE Transactions on Energy Conversion*, vol. 28, no. 1, pp. 34-43, March 2013.

[31] Y. Pannatier, B. Kawkabani, C. Nicolet, J.-J. Simond, A. Schwery and P. Allenbach, "Investigation of Control Strategies for Variable-Speed Pump-Turbine Units by Using a Simplified Model of the Converters," *IEEE Transactions on Industrial Electronics*, vol. 57, no. 9, pp. 3039-3049, September 2010.

[32] V. M. Bida, D. V. Samokhvalov and F. S. Al-Mahturi, "PMSM Vector Control techniques - A Survey," in *IEEE Conference of Russian Young Researchers in Electrical and Electronic Engineering (EIConRus)*, Moscow and St. Petersburg, Russia, 2018.

[33] "Wikipedia," [Online]. Available: https://en.wikipedia.org/wiki/Eddy_current. [Accessed 29 January 2024].

[34] A. Tessarolo, "A Quadratic-Programming Approach to the Design Optimization of Fractional-Slot Concentrated Windings for Surface Permanent-Magnet Machines," *IEEE Transactions on Energy Conversion*, vol. 33, no. 1, pp. 442-452, March 2018.

[35] A. Tessarolo, "A survey of state-of-the-art methods to compute rotor eddycurrent losses in synchronous permanent magnet machines," in *IEEE Workshop on Electrical Machines Design, Control and Diagnosis (WEMDCD)*, Nottingham, UK, 2017.

[36] A. Tessarolo, F. Luise, S. Fieri, A. Benedetti, M. Bortolozzi and M. De Martin, "Design for Manufacturability of an Off-Shore Direct Drive Wind Generator: An Insight Into Additional Loss Prediction and Mitigation," *IEEE Transactions on Industry Applications*, vol. 53, no. 5, pp. 4831-4842, 2017.

[37] J. Gieras, Electrical Machines: Fundamentals of Electromechanical Energy Conversion, CRC Press, 2016.

[38] Y. Yokoi, T. Higuehi and Y. Miyamoto, "General formulation of winding factor for fractional-slot concentrated winding design," *IET Electric Power Applications*, vol. 10, no. 4, pp. 231-239, April 2016.

[39] S. Skaar, O. Krovel and R. Nilssen, "Distribution, coil-span and winding factors for PM machines with concentrated windings," *17th International Conference on Electric Machines, ICEM 2006, Cliania, Crete Island, Greece,* September 2006.

[40] F. Lin, S. Zuo and X. Wu, "Electromagnetic vibration and noise analysis of permanent magnet synchronous motor with different slot-pole combinations," *IET Electric Power Applications,* vol. 10, no. 9, pp. 900-908, November 2016.

[41] S. G. Min and B. Sarlioglu, "Investigation of electromagnetic noise on pole and slot number combinations with possible fractional slot concentrated windings," *IEEE Transportation Electrification Conference and Expo (ITEC), Chicago,* 2017.

[42] Z. Zhu and D. Howe, "Influence of design parameters on cogging torque in permanent magnet machines," *IEEE Transactions on Energy Conversion,* vol. 15, no. 4, pp. 407-412, December 2000.

[43] L. Zhu, S. Z. Jiang, Z. Q. Zhu and C. C. Chan, "Analytical Methods for Minimizing Cogging Torque in Permanent-Magnet Machines," *IEEE Transactions on Magnetics,* vol. 45, no. 4, pp. 2023-2031, April 2009.

[44] P. Ponomarev, P. Lindh and J. Pyrhdnen, "Effect of Slot-and-Pole Combination on the Leakage Inductance and the Performance of Tooth-Coil Permanent-Magnet Synchronous Machines," *IEEE Transactions on Industrial Electronics,* vol. 60, no. 10, pp. 4310-4317, 2013.

[45] C. Ciriani, "UniTs," [Online]. Available: https://arts.units.it/handle/11368/3030489. [Accessed 31 January 2024].

[46] A. S. Abdel-Khalik, S. Ahmed and A. M. Massoud, "Low space harmonics cancelation in Double-Layer fractional slot winding using dual multiphase winding," *IEEE Transactions on Magnetics,* vol. 51, no. 5, May 2015.

[47] L. Alberti and N. Bianchi, "Theory and Design of Fractional-Slot Multilayer Windings," *IEEE Transactions on Industry Applications,* vol. 49, no. 2, pp. 841-849, April 2013.

[48] Y. Wang, R. Qu and J. Li, "Multilayer windings effect on interior PMmachines for EV applications," in *International Conference on Electrical Machines (ICEM),* Berlin, Germany, 2014.

[49] A. Tessarolo, M. Mezzarobba and N. Barbini, "Improved four-layer winding design for a 12-slot 10-pole permanent magnet machine using unequal tooth coils," in *IECON 2016 - 42nd Annual Conference of the IEEE Industrial Electronics Society*, Florence, Italy, 2016.

[50] C. Ciriani, H. A. Khan, K. Mansour, M. Olivo and A. Tessarolo, "Simple and Accurate Computation of Rotor Eddy-Current Losses in Surface-Mounted Permanent Magnet Machines Accounting for Magnet Circumferential Segmentation," *IEEE Access*, vol. 12, pp. 36810-36824, 2024.

[51] C. Ciriani, H. A. Khan, K. Mansour, M. Olivo and A. Tessarolo, "A General Approach to the Design of Multi-Layer Fractional-Slot Concentrated Windings With Arbitrary Number of Slots, Poles, and Phases," *IEEE Access*, vol. 12, pp. 89248-89261, 2024.

[52] A. M. El-Refaie and T. M. Jahns, "Scalability of surface PM Machines with concentrated windings designed to achieve wide speed ranges of constant-power operation," *IEEE Trans. Energy Convers.*, vol. 21, no. 2, pp. 362-369, June 2006.

[53] "GrabCAD," [Online]. Available: https://grabcad.com/library/archimedes-screw-turbine-1. [Accessed 14 August 2024].